

NORTHWESTERN UNIVERSITY

**A Search for Dark Matter Produced in Association with $t\bar{t}$ at $\sqrt{s} = 13$ TeV in the
Dilepton Final State with the CMS Experiment**

A DISSERTATION

**SUBMITTED TO THE GRADUATE SCHOOL
IN PARTIAL FULFILLMENT OF THE REQUIREMENTS**

for the degree

DOCTOR OF PHILOSOPHY

Field of Physics and Astronomy

By

Stanislava Lubomirova Sevova

EVANSTON, ILLINOIS

June 2018

Abstract

4.5 years of POOP!

Declaration

I haz dun most of dis werk.

Stanislava Sevova

Acknowledgements

H8rz gonna h8.

Preface

This thesis describes my research on various aspects of the CMS particle physics program, centred around the CMS detector and LHC accelerator at CERN in Geneva.

For this example, I'll just mention Chapter ?? and Chapter ??.

Contents

1. Dark matter: Beyond the Standard Model	1
1.1. Introduction to dark matter	2
1.2. The Standard Model	8
1.2.1. Dark matter candidates	8
1.3. Dark matter detection	8
1.3.1. Direct detection	8
1.3.2. Indirect detection	8
1.3.3. Collider searches	8
1.4. Simplified models of DM: beyond the Standard Model	8
2. The CMS experiment	9
2.1. The LHC	9
2.2. The CMS experiment	13
2.2.1. The magnet	15
2.2.2. The inner tracker	18
2.2.3. The calorimeters	22
2.2.4. The muon detectors	27
2.2.5. The readout system	30
2.2.6. Computing and Data Storage	37

3. Object and event reconstruction	39
3.1. Leptons	39
3.1.1. Muons	40
3.1.2. Electrons	43
3.2. Jets	47
3.2.1. b jet tagging	49
3.3. Missing transverse energy	51
4. Signal simulation and event selection	55
4.1. $t\bar{t} + \chi\bar{\chi}$ simplified models	55
4.2. Signal region event selection	58
4.2.1. The $M_{T2}^{\ell\ell}$ variable	59
5. Background processes	63
5.1. $t\bar{t}(2\ell)$	65
5.2. $t\bar{t} + V$, diboson, and single top processes	66
5.3. Drell-Yan	68
5.3.1. The $R_{in/out}$ method	69
5.4. Fake lepton background	77
5.4.1. Fake rate measurement	78
5.4.2. Fake rate application	79
5.4.3. Fake rate closure test	81
6. Analysis	83
6.1. Search strategy	83
6.2. Data to simulation corrections	84
6.2.1. Trigger efficiency	84
6.2.2. PU reweighting	84
6.2.3. Top p_T re-weighting	86

6.2.4. b-tagging efficiency	87
6.3. Discriminating observables	89
6.4. Systematic uncertainties	90
6.4.1. Sources of systematic uncertainty	91
6.5. Statistical analysis	95
6.5.1. Maximum likelihood	95
6.5.2. Hypothesis testing	96
6.5.3. Signal extraction	99
6.5.4. Post-fit diagnostics	101
7. Results	113
7.1. Simplified model interpretation	113
7.2. Upper limits on $t\bar{t} + \chi\bar{\chi}$ production in the dilepton channel	116
7.3. Comparison with direct detection	120
7.3.1. Spin-indepedent comparison	120
A. Pointless extras	123
A.1. Like, duh	123
A.2. $y = \alpha x^2$	124
Bibliography	127
List of figures	133
List of tables	135

Chapter 1.

Dark matter: Beyond the Standard Model

The Standard Model (SM) of particle physics, albeit a successful theory encoding the properties of elementary particles and their interactions, nonetheless has some shortcomings. For one, cosmological and astrophysical observations supply compelling evidence [1–3] for the existence of dark matter (DM), a piece of the astro-particle physics puzzle that does not fit together with the SM. In Sec. 1.1, evidence of the existence of DM and motivations for its search are briefly detailed, while in Sec. 1.3 the three main modes of DM detection are outlined, with a particular emphasis on particle colliders. An outline of the SM is presented in Sec. 1.2 and its connection with DM is described in Sec. 1.4, with a focus on beyond the Standard Model (BSM) simplified models of DM currently being probed at general-purpose detectors at the Large Hadron Collider (LHC) in Geneva, Switzerland.

1.1. Introduction to dark matter

Observations at all scales, from smaller dwarf galaxies to large cosmological scales point to the existence of more matter than can be reconciled with the amount of visible matter in our universe. The existence of additional non-luminous matter and its dominance in amount compared to luminous matter, was first postulated by Swiss physicist Fritz Zwicky in 1933 during his studies of the Coma cluster. Zwicky's observations pointed to the necessity for approximately 400 times [4] the mass density as observed from the luminous matter from the cluster to ensure the gravitational bounding of nebulae within Coma. It is worth noting that Zwicky's calculations made extensive use of Hubble's constant at the time, $H_0 = 558 \text{ km/s/Mpc}$, and if rescaled by the modern value of $H_0 = 67.27 \pm 0.66 \text{ km/s/Mpc}$ [5] Zwicky's results point to approximately a mass density 10 times larger than observed [6]. The period around the 1950's and 1960's marks a time when various astronomical explanations for the missing mass in galaxy clusters began to be ruled out, such as the hypothesis that dark matter consists of hot intracluster gas. Ref. [7] presents evidence that the amount of gas required for gravitational binding is 98% larger than that observed from X-ray emission spectra. During the 1970's the first explicit statements began to emerge regarding the need of the missing mass to be concentrated in the outer parts of galaxies based on spectroscopic and radio astronomy observations of the galactic rotation velocity curves. Namely, Kent Ford and Vera Rubin published results from observations of the Andromeda galaxy which extended the observational reach out to 110 minutes of arc away from the center of M31, revealing a flat dependence of v , the galactic rotation velocity, as a function of the radius r beyond the visible galactic disk as shown in Figure 1.1. By the onset of the 1980's the majority of the astrophysical community was convinced that a substantial amount of DM exists in the universe

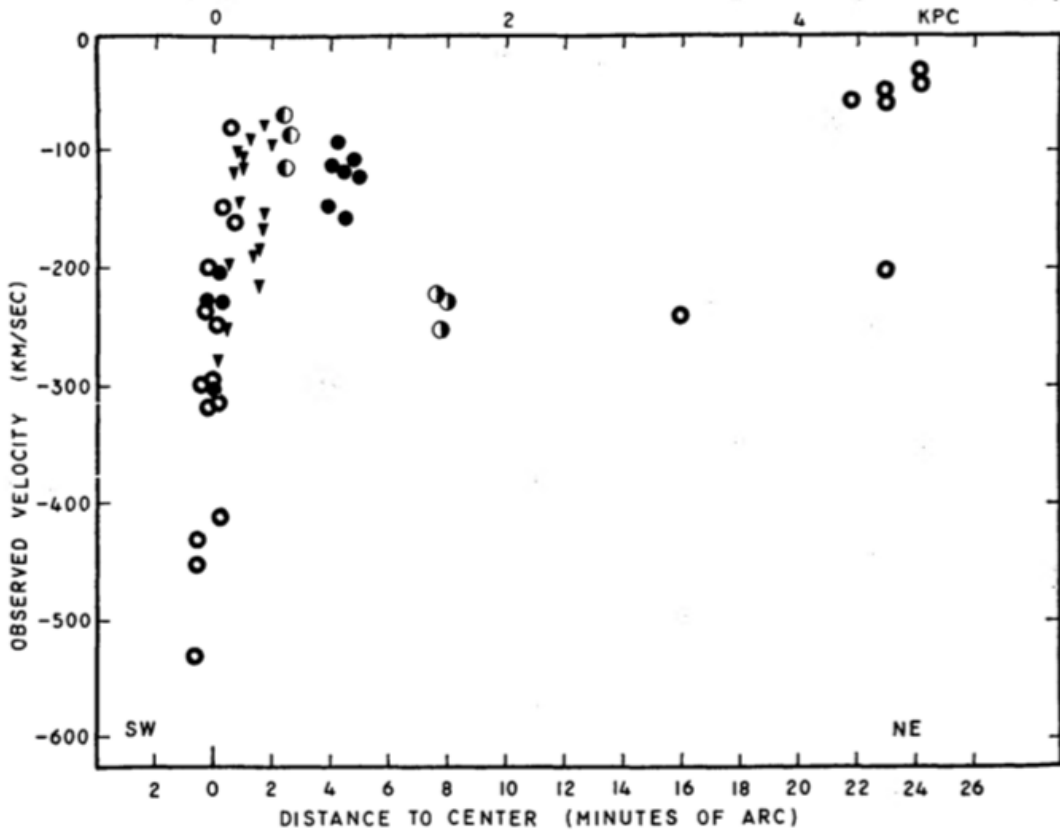


Figure 1.1.: The velocities of emission regions from M31 as a function of distance to the center of the galaxy measured in minutes of arc along the NE major axis as reported by Rubin and Ford in Ref. [8].

based on the observational evidence of mass-to-light ratios of galaxies and galactic rotation curves.

Studies of the large scale structure of the universe have provided clues as to the nature of dark matter. Just as on the small scale, ordinary visible matter consists of protons, electrons, neutrons, or groups of atoms held together by the electromagnetic force, analogously groups of matter peaks containing stars were bound together by the gravitational force provided sufficiently massive in order to form stellar clusters. These groups were in turn merged with gas and the postulated DM to form galaxies and the galaxies were bound together to form clusters, and superclusters. This standard theory of cosmic structure formation is often referred to as the “bottom-up” approach,



Figure 1.2.: A composite image from the Hubble, Chandra, and Magellan telescopes of the 1E 0657-558 cluster of galaxies (Bullet cluster) depicting the X-rays emitted by the baryonic matter as a diffuse red gas, while the approximate location of the DM surrounding the visible matter is represented in a blue hue.

and essentially posits that the current structure of the Universe is a result of the gravitational amplification of tiny matter fluctuations that were generated during the very early epochs of the Universe [9]. The evidence from the 20th century for the existence of non-luminous matter has been further supplemented with data from weak [10] and strong [11] gravitational lensing by large scale structures. The distortion of the appearances of distant objects or the duplication of the apparent image is caused by the bending of the light these objects emit by the gravitational force of the large scale structures in between the observer and the object. The data from a survey of the Bullet cluster as observed by the Chandra [12] experiment best illustrates how the distribution of the hot gas and stars originating from the collision of two galaxies and comprising the baryonic matter are bound together by a much greater contribution of non-luminous matter as seen in Figure 1.2. The calculation of the approximate contribution of visible matter was performed using data from gravitational lensing.

The aforementioned experiments and measurements buttress the necessity for the existence of DM, however the first attempts to precisely quantify the amount of DM in the Universe began with discovery and subsequent analyses of the cosmic microwave background (CMB) by Peebles, Wilkinson, Dicke, and Roll [13]. In brief, the CMB is the relic radiation energy content from beyond our galaxy, emitted shortly before the period of recombination [14] which occurred approximately 380 000 years after the Big Bang. At this stage, photons began to decouple from the baryonic matter and over time have been redshifted to the microwave frequency range as a result of the expansion of the Universe over the past 13.81 billion years. Although the dominant contributions of the CMB are homogeneous and isotropic wherein the CMB temperature is almost uniformly $T \simeq 2.72$ K, slight temperature fluctuations of $\mathcal{O}(10^{-5})$ have been observed which are indicative of the state of the early Universe and the relative abundance of visible and dark matter during this period. As gravity acted on the photon-baryon plasma, the fluid pressure increased giving way to its expansion. This cycle was repeated once the pressure decreased as a result of the expansion, and gravity once more won over causing a fluid compression, hence the photons emitted during compression stages were of varying energies. More specifically, the period of photon decoupling leading to these relic temperature variations, known as the CMB anisotropy, can be interpreted as a power spectrum in terms of multipole orders, ℓ . The effects produced by the acoustic oscillations of the photon-baryon plasma just prior to the emission of the CMB are captured in this spectrum. Since both types of matter contribute to the temperature oscillations via gravitational effects, the power spectrum shown in Figure 1.3 contains information about the relative content of both visible and dark matter. The parametrization of the temperature anisotropies is in terms of spherical harmonics contained in the two-dimensional function, $T(\theta, \phi)$ projected over the entire visible sky defined as,

$$T(\theta, \phi) = \sum_{\ell=0}^{\infty} \sum_{m=-\ell}^{\ell} a_{\ell m} Y_{\ell m}(\theta, \phi), \quad (1.1)$$

where θ and ϕ are angular coordinates, ℓ is the multipole order, and $a_{\ell m}$ are the multipole moments. Following the theory of temperature fluctuations, the distributions of the coefficients $a_{\ell m}$ are approximately Gaussian centered about zero with a variance defined as $C_{\ell} \equiv <|a_{\ell m}|^2>$, where there are only $2\ell + 1$ values of m for each ℓ , hence

$$C_{\ell} \equiv <|a_{\ell m}|^2> \equiv \frac{1}{2\ell + 1} \sum_{m=-\ell}^{+\ell} |a_{\ell m}|^2. \quad (1.2)$$

The power spectrum, C_{ℓ} is expressed as $\ell(\ell + 1)C_{\ell}/2\pi$ in Figure 1.3, and fit to the Planck data provides the abundances of baryonic and dark matter. The location of the first peak is related to the flat geometry of the Universe and requires that the total energy-matter density ratio, $\Omega_{\text{total}} = 1$. The resolution of this peak is connected to the expansion of the Universe which is driven by the repulsive force of dark energy [15]. The angular resolution of the second peak, at $\ell_2 \simeq 500$, provides the amount of ordinary matter that exists in the Universe, and correspondingly, the difference between the third peak, at $\ell_3 \simeq 700$, and the second peak provides the density of the dark matter in the early Universe. The extracted total densities of baryonic and dark matter are respectively,

$$\Omega_b h^2 = 0.02222 \pm 0.00023, \quad \Omega_{\text{DM}} h^2 = 0.1186 \pm 0.0020, \quad (1.3)$$

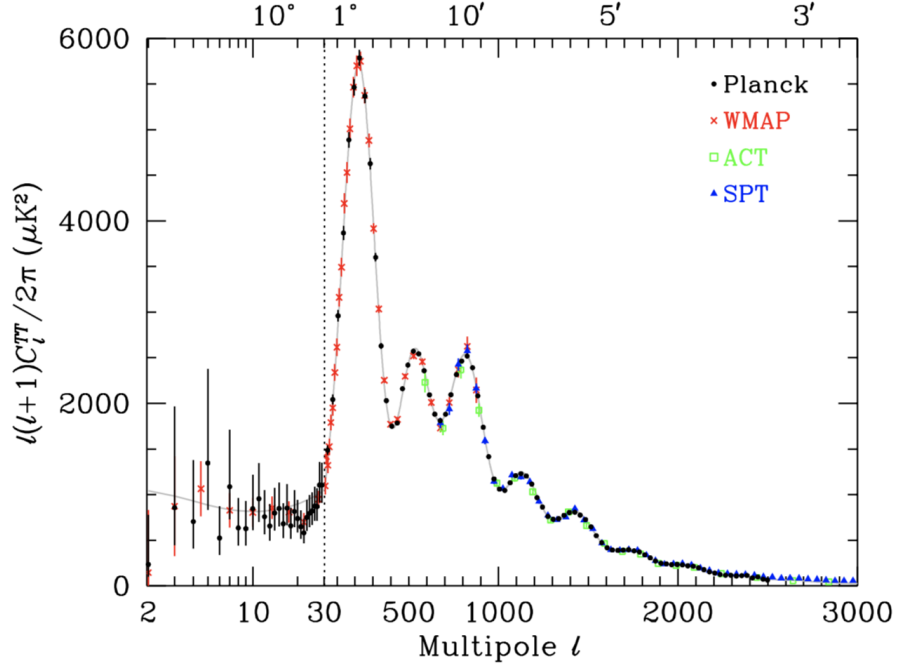


Figure 1.3.: The CMB radiation temperature anisotropy power spectrum as a function of the multipole order, ℓ , as measured by various experiments [16]. The angular scales that correspond to the multipole orders are listed across the top of the graph. The data points correspond to the experimental measurements and the error bars account for measurement uncertainties. The black curve represents the best global fit of the standard model of cosmology to the Planck data.

where $h = H_0/100$, translating to 24% and 4.8% of the total matter in the Universe as being dark and baryonic, respectively, while the rest consists of dark energy [16].

1.2. The Standard Model

1.2.1. Dark matter candidates

1.3. Dark matter detection

1.3.1. Direct detection

1.3.2. Indirect detection

1.3.3. Collider searches

1.4. Simplified models of DM: beyond the Standard Model

Chapter 2.

The CMS experiment

2.1. The LHC

The Large Hadron Collider (LHC) [17] at CERN is the most powerful particle accelerator in the world, located in the same tunnel as the Large Electron-Positron collider (LEP) [18]. At 27 km in circumference, the LHC is a two-ring, superconducting accelerator and proton-proton (or proton-ion or ion-ion) collider with a two-fold experimental mandate: to probe the electroweak symmetry breaking mechanism via which particles in the Standard Model (SM) attain mass, and to extend the exploration of the energy frontier in search for new physics beyond the SM (BSM). Pictured in Figure 2.1 is the approximate LHC ring size superimposed on top of a map of the Swiss-French border near Geneva, Switzerland. The LHC is comprised of octancts, and the locations at which beam collisions occur are the interaction points (IP). The general purpose high luminosity (L) experiments on the LHC ring are the CMS (Compact Muon Solenoid) [19] and ATLAS (A Toroidal LHC ApparatuS) [20] detectors located at IP5 and IP1, respectively. The low luminosity experiment dedicated to B-physics,

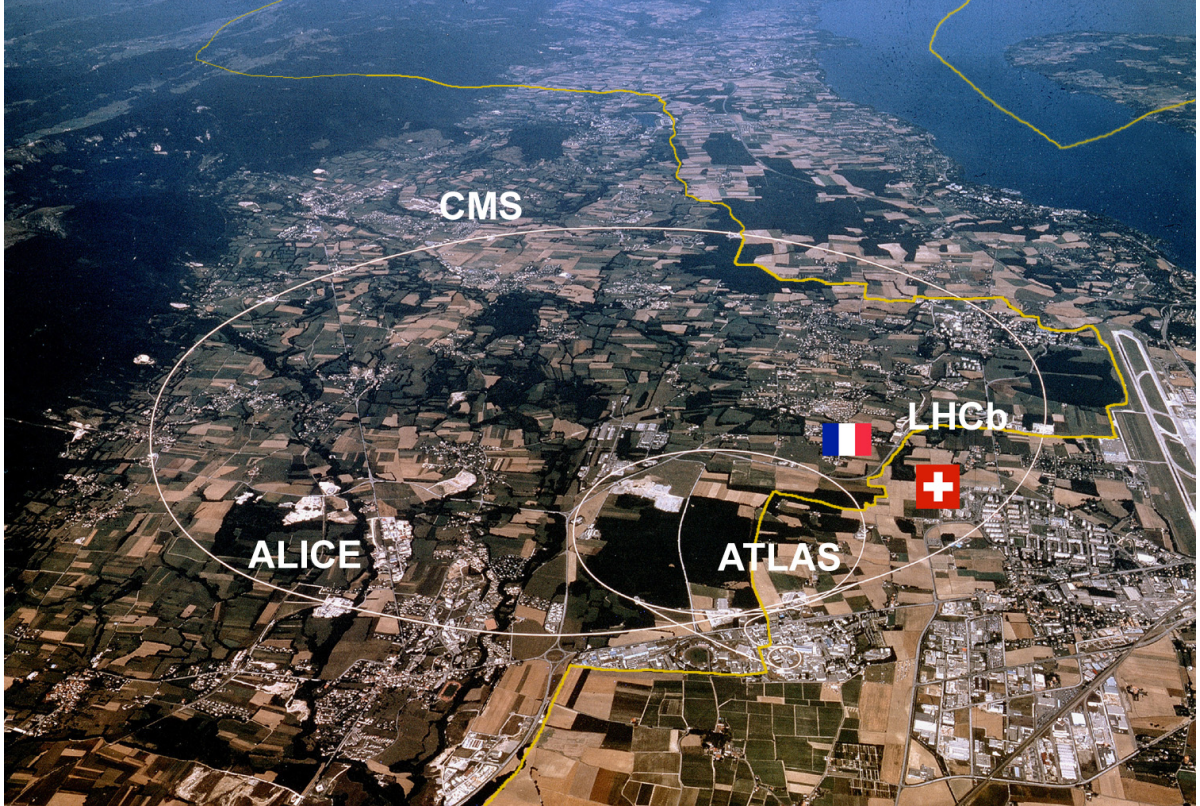


Figure 2.1.: The approximate location of the LHC ring traced over the Swiss-French border near Geneva, Switzerland. Also indicated are the relative locations of the two high luminosity experiments (CMS and ATLAS), the low luminosity B-physics dedicated experiment (LHCb), and the dedicated ion experiment (ALICE).

LHCb [21] is located at IP8, and the dedicated ion collision detector ALICE (A Large Ion Collider Experiment) [22] is located at IP2, as depicted in Figure 2.1.

The total center-of-mass energy of a beam collision is twice the energy of the incoming beam [23], and the LHC is designed to reach a center-of-mass collision energy of up to $\sqrt{s} = 14 \text{ TeV}$, with each beam able to reach energies of 7 TeV . The total number of events that are generated in an LHC collision are given by $N_{\text{event}} = L\sigma_{\text{event}}$, with σ_{event} being the cross section for the relevant measured event and L being the machine luminosity. L depends only on the beam parameters and goes as,

$$L = \frac{N_b^2 n_b f_{\text{rev}} \gamma_r}{4\pi \epsilon_n \beta^*} F, \quad (2.1)$$

where N_b is the number of particles per bunch, n_b is the number of bunches per beam, f_{rev} is the revolution frequency, γ_r is the relativistic gamma factor, ϵ_n is the normalized transverse beam emittance, β^* is the beta function at the interaction point (IP), and F is the geometric luminosity reduction factor due to the crossing angle at the IP. The peak LHC design luminosity $L = 10^{34} \text{ cm}^{-2} \text{ s}^{-1}$ dictates the necessity of high beam intensities, thus proton rather than anti-proton beams are used. The two beams of equally charged particles are circulated in opposite directions within separate beam pipes, and accelerated using separate and opposite magnet dipole fields and vacuum chambers in the main arcs.

The point of commencement for the protons circulated in the main LHC ring is a bottle of hydrogen gas at one end of the Linear accelerator 2 (Linac 2). Passing through an electric field that strips the hydrogen of its electrons, the remaining protons enter the Linac 2 and pass through alternating positive and negative cylindrical conductors charged by radiofrequency cavities, which push and pull the protons causing them to accelerate to approximately 50 MeV. The protons then enter the Proton Synchrotron (PS) Booster, which accelerate the beams to 1.4 GeV by means of four superimposed synchrotron rings. The protons then enter the PS, which is 628 m in circumference and accelerates the beams to 25 GeV through the use of conventional (i.e. not superconducting) magnets, of which 100 are dipoles that bend the beams around the ring. At this stage, a package of roughly one hundred billion protons, known as a “bunch”, is separated from another bunch by a spacing of 25 ns, meaning that a proton bunch now rotates at 40 MHz. The following stage is the Super Proton Synchrotron (SPS), which has the same function as the PS, however with a circumference of nearly 7 km

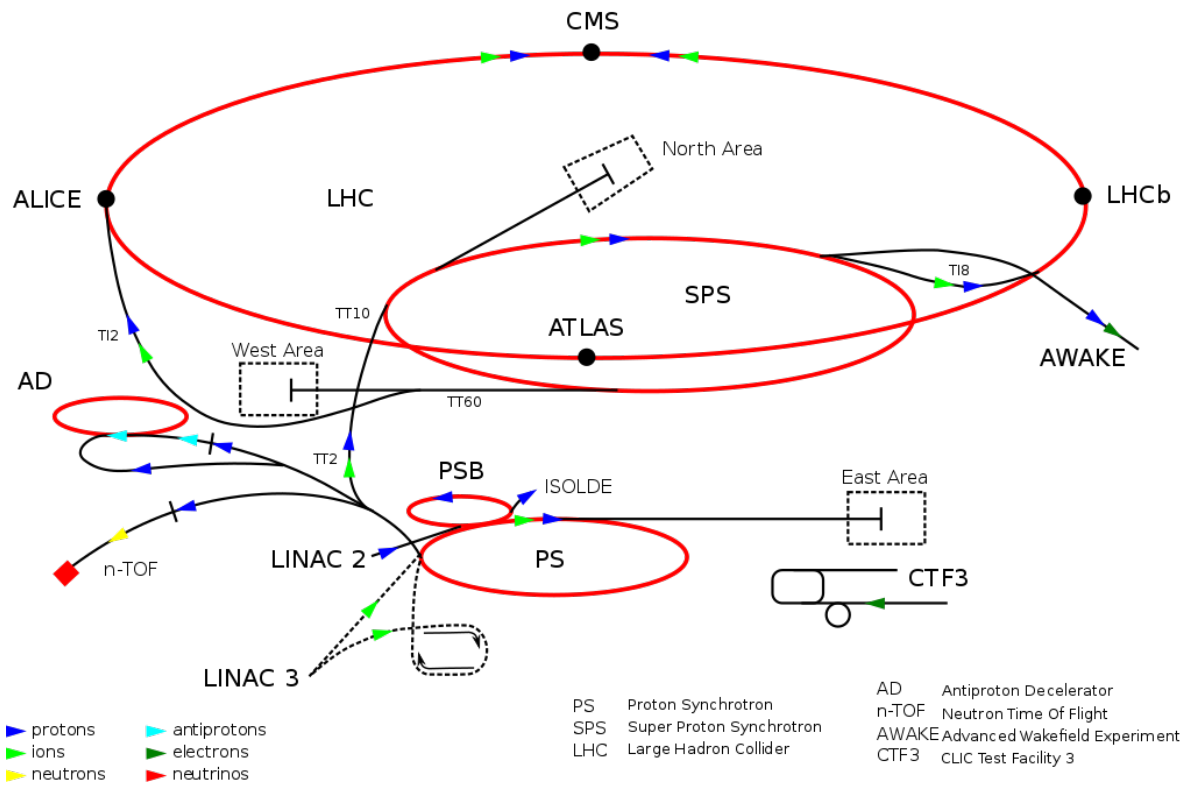


Figure 2.2.: A schematic of the CERN accelerator complex, where protons (blue arrows) and ions (lime green arrows) begin their journey to the main LHC ring at the Linac 2 and Linac 3, respectively.

and 744 dipole magnets, the SPS is able to accelerate the proton beams up to an energy of 450 GeV. At this stage the proton beam undergoes a bifurcation into bunch trains with two beams which enter the LHC moving in opposite directions. The chain is illustrated in Figure 2.2 showing an overview of the CERN accelerator complex and the aforementioned experiment IPs.

Once injected into the LHC, the proton beams undergo a ramp up in energy in order to reach the maximum design energy of 7 TeV per beam, typically making 10^5 traversals of the ring. In order to achieve these energies, the beam traverses a number of radiofrequency cavities, which are cooled with liquid helium to an operating temperature of 4.5 K. In addition, 1232 superconducting dipole magnets measuring 15 m in length are used to constrain the beam in a near circular path with a generated magnetic field of approximately 8.33 T, whilst 392 quadrupole magnets supercooled

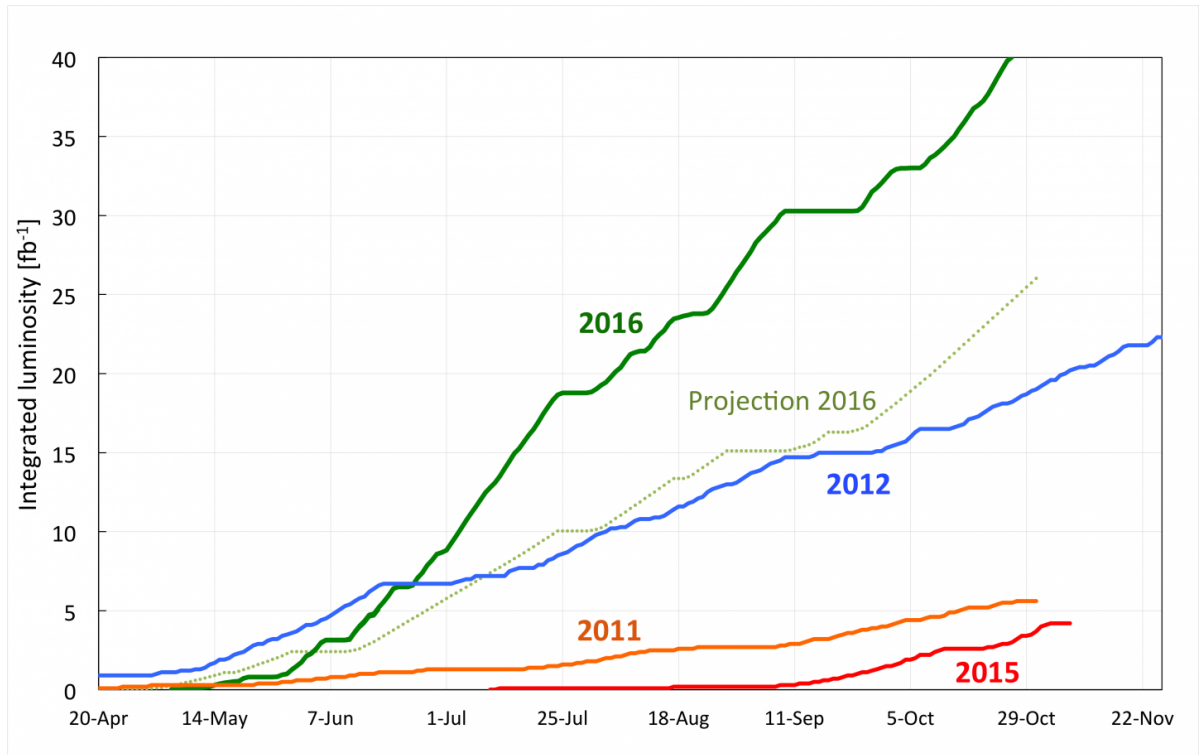


Figure 2.3.: The integrated luminosity as a function of time that the LHC delivered at $\sqrt{s} = 7\text{ TeV}$ and $\sqrt{s} = 8\text{ TeV}$ during 2011 and 2012, and at $\sqrt{s} = 13\text{ TeV}$ during 2015 and 2016.

to 1.9 K and measuring 5-7 m, focus the beams and facilitate the collisions at the designated IPs. During 2011 and 2012, the LHC collided proton beams at $\sqrt{s} = 7\text{ TeV}$ and $\sqrt{s} = 8\text{ TeV}$ respectively, while the energy increased to $\sqrt{s} = 13\text{ TeV}$ in 2015 and 2016. The total integrated luminosity delivered by the machine as a function of time can be seen in Figure 2.3, where the performance of the LHC was better than projected for 2016.

2.2. The CMS experiment

Quantities described in this and following sections and chapters will rely heavily on the cylindrical coordinate system defined by the detector structure. The z -axis is defined to be parallel to the beam pipe pointing in the direction towards the Jura

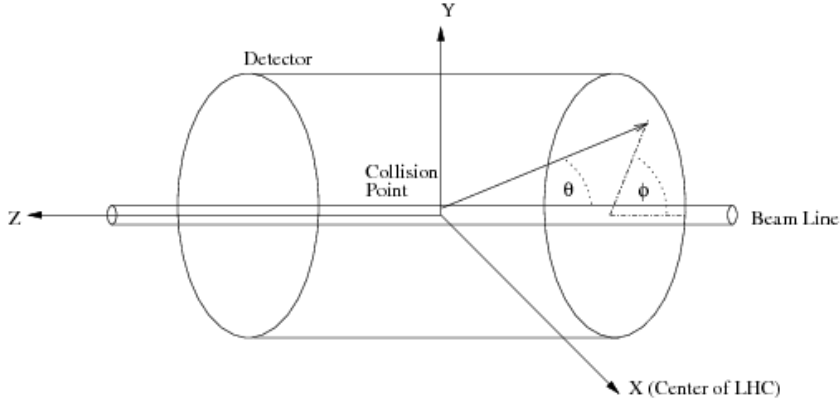


Figure 2.4.: A diagram of the cylindrical coordinate system for the CMS detector.

mountains from IP5, the azimuthal angle ϕ is defined in the transverse x - y plane perpendicular to the beam line, and θ is the polar angle measured from the z -axis, as shown in Figure 2.4. Consequently, quantities such as p_T , the transverse momentum, and E_T , the transverse energy are defined in terms of the respective momentum and energy in the x - y plane. Rather than using θ to describe the direction of a particle trajectory within the detector, it is common practice in the case of highly relativistic particles to use *pseudorapidity* defined as,

$$\eta = -\ln \left[\tan \left(\frac{\theta}{2} \right) \right] = \frac{1}{2} \ln \left(\frac{|\mathbf{p}| + p_z}{|\mathbf{p}| - p_z} \right) \quad (2.2)$$

in terms of both the polar angle, and \mathbf{p} , the three momentum and p_z , the momentum along the z -axis. $\eta = 0$ for $\theta = 90^\circ$ and approaches infinity as the polar angle goes to 0. Throughout this chapter and the following, detector regions will be referred to as “barrel” if $|\eta| < 1.4$, “endcap” if $1.4 < |\eta| < 3.0$, and “forward” if $|\eta| > 3.0$.

The CMS detector, described in detail in Ref. [?], is a multi-purpose apparatus designed to study high- p_T physics processes in proton-proton and heavy-ion collisions. In 2016, CMS collected nearly 38 fb^{-1} of integrated luminosity as seen in Figure 2.5,

of which 35.9 fb^{-1} were certified as usable for physics analysis. The CMS detector relies on a superconducting solenoid magnet located in its central region to provide a magnetic field of 3.8 T parallel to the beam direction. Charged particle trajectories are measured by silicon pixel and strip trackers, which cover a pseudorapidity region of $|\eta| < 2.5$. Surrounding the tracker volume are a lead-tungstate crystal electromagnetic calorimeter (ECAL) and a brass-and-scintillator hadron calorimeter (HCAL) surround the tracking volume, covering the region of $|\eta| < 3$. A steel and quartz-fiber Cherenkov forward hadron calorimeter extends the coverage to $|\eta| < 5$. The muon system consists of gas-ionization detectors embedded in the steel flux return yoke outside the solenoid, and covers the region with $|\eta| < 2.4$. The detector is designed to cover a 4π solid angle as illustrated in Figure 2.6, demonstrating the overall scale of the experiment and the surrounding cavern structure.

2.2.1. The magnet

The benefit of the strong magnetic field provided by the superconducting solenoid is the improvement in the momentum resolution for muons, and the increase efficiency of the inner tracking [24]. The main components comprising the magnet are the superconducting solenoid coil, the 1.5 m thick saturated iron yoke in the barrel and endcap regions which return a 2 T magnetic flux, vacuum chambers, and the cryogenic system. Stabilised, reinforced NbTi conductor is used for the 4-layer winding of the coil cold mass, which measures 12.5 m in length. Since the CMS magnet can achieve a stored energy and an energy-to-mass (E/M) ratio significantly larger than any other previous detector magnet technologies, the shear stress level inside the coil winding is non-negligible, thus an innovative self-supporting aluminum conductor is included in the magnet structural material to mitigate these effects.

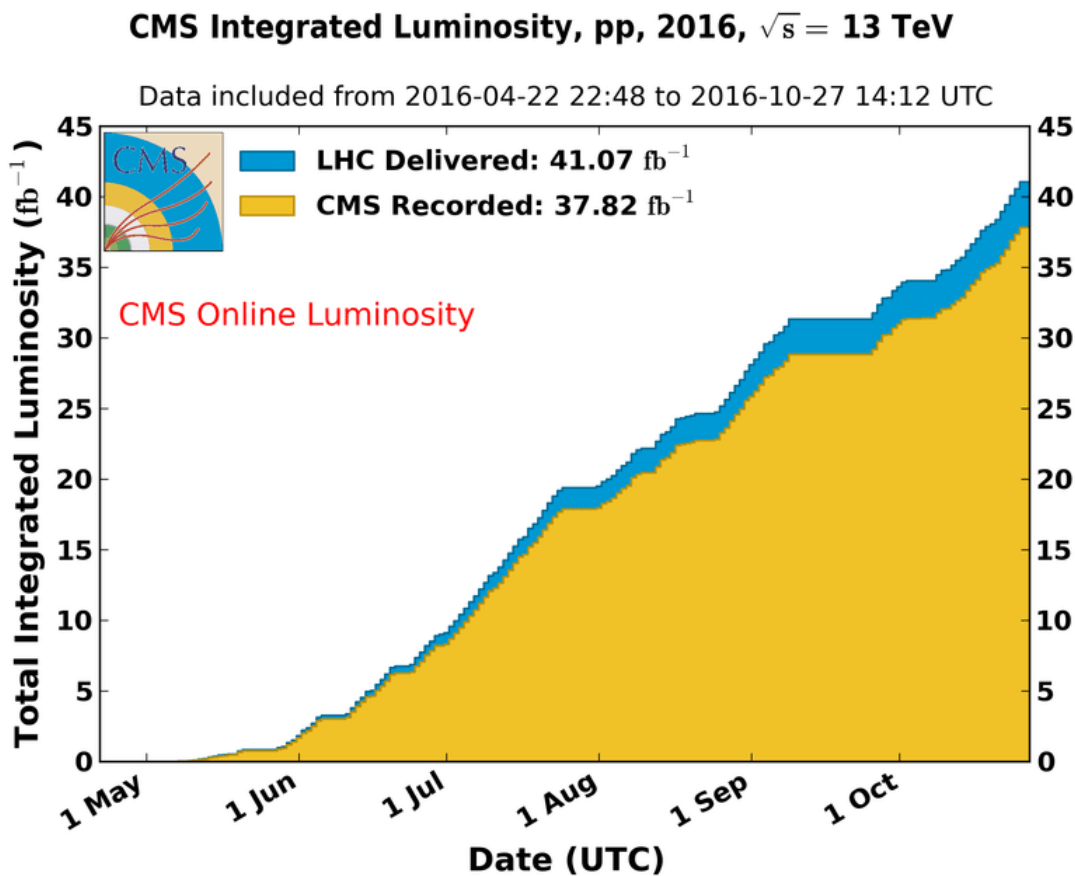


Figure 2.5.: The total integrated luminosity that the LHC machine delivered to CMS, and the total integrated luminosity that the detector collected during the 2016 data-taking period.

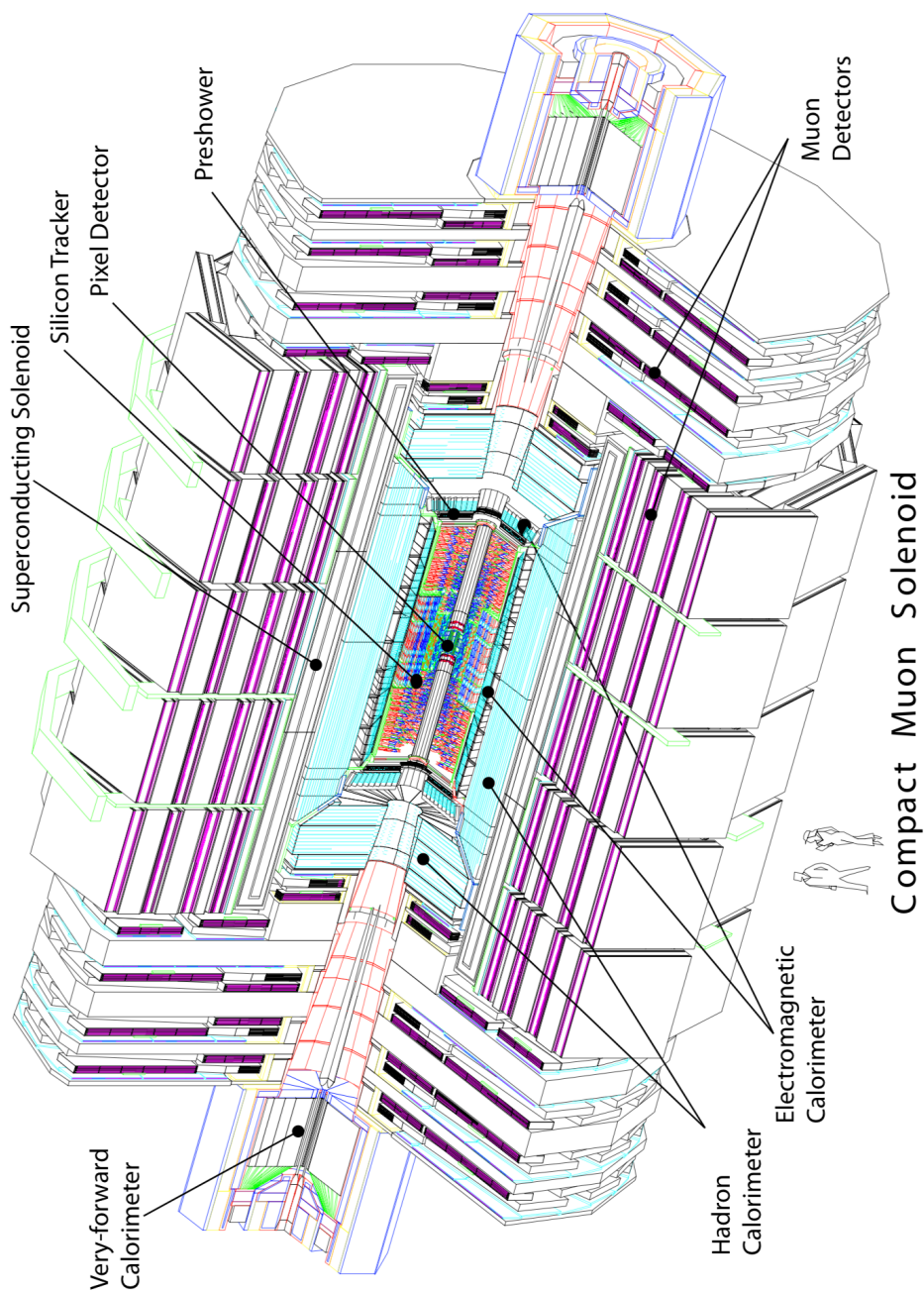


Figure 2.6.: Cross-section view of CMS.

The 3.8 T field that is generated inside the solenoid bends charged particle trajectories in the enclosed silicon tracking detector, enabling the measurement of the p_T of a particle track via the azimuthal angle ϕ , which is related to the bending radius ρ and the magnet length L by $\phi = L/\rho$. ρ can be obtained via,

$$\rho = \frac{p_T}{0.3zB} , \quad (2.3)$$

where B is the magnetic field in the z direction, parallel to the beam axis, and a particle charge of ze is assumed. The muon system stations, described in greater detail in Sec. 2.2.4 interleaved in the iron yoke are also subjected to a 2 T return flux, causing charged particles to bend in the opposite direction from their trajectory within the inner tracker volume. Multiple measurements N made along the trajectory of a uniform medium provide the curvature ($k = 1/\rho$) error δk_{res} due to finite measurement resolution which goes as,

$$\delta k_{\text{res}} = \frac{\epsilon}{L'} \sqrt{\frac{720}{N+4}} \quad (2.4)$$

2.2.2. The inner tracker

One of the main mandates of the CMS detector is to provide good resolution and reconstruction efficiency for charged particles emitted from LHC collisions in the inner tracker, of which a cross-sectional view is shown in Figure 2.7. Furthermore, the precise reconstruction of secondary vertices is imperative for the efficient identification of b-jets; b-jets being the only flavor jets expected in the dilepton channel $t\bar{t} + \chi\bar{\chi}$ signal

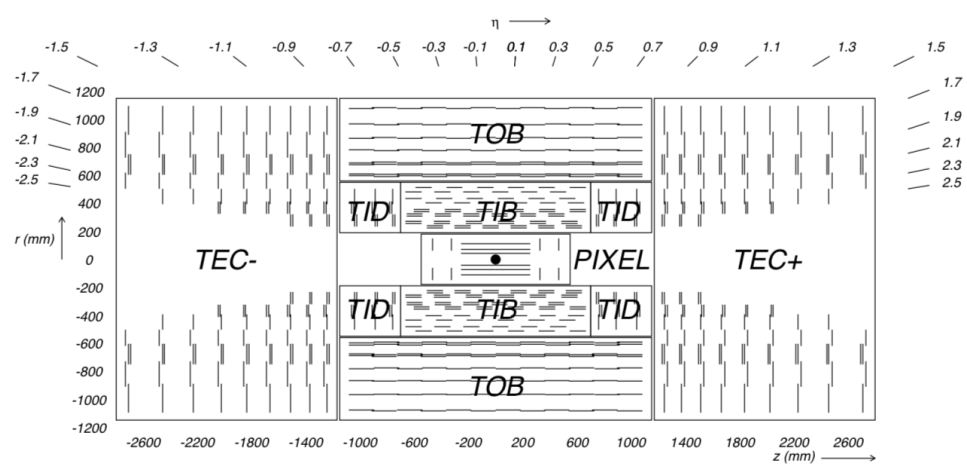


Figure 2.7.: Schematic cross-section through the CMS tracker, where a single detector modules is represented by a line, and double lines signify back-to-back modules.

final state topology. To achieve this, it is imperative for the positioning of tracker layers to be close to the interaction point of a collision, hence the first through third of three pixel barrel (BPix) layers are stationed at radii 4.4 cm, 7.3 cm, and 10.4 cm from the interaction point. Designed to keep the occupancy of these inner layers below 1%, the silicon pixel cells measure $100 \times 150 \mu\text{m}^2$ in $r - \phi$ and z respectively, of which 52×80 cells populate one read-out chip (ROC) and 16 ROCs comprise one BPix module sensor. In order to cover out to $|\eta| < 2.5$, the pixel detector also has two endcap disks (FPix) stationed on either side of the BPix at $z = \pm 34.5$ and $z = \pm 46.5$ cm and extending from 6 to 15 cm in r . The FPix consists of varying trapezoidal (pie-shaped) panels which contain different numbers of *plaquettes* consisting of single pixel sensors bump-bonded to a varying number of ROCs. The sensors are offset on the panels so as to ensure there are no cracks in the endcap η coverage. The BPix and FPix deliver up to three high precision spatial point positions (hits) for which the resolution in $r - \phi$ is up to $10 \mu\text{m}$ and that in z is up to $20 \mu\text{m}$. The operating temperature of the pixel detector during 2016 was -10°C .

Surrounding the pixel layers are the four and six silicon strip layers comprising the Tracker Inner Barrel (TIB) and Tracker Outer Barrel (TOB), respectively. The TIB extends radially from 20 to 55 cm, with a relative occupancy of 2 – 3% per strip module in this intermediate region. The distance between the p+ type strip implants in the n type SiO_2 bulk of the strip sensors is called the pitch [25] and is approximately $80 \mu\text{m}$ for the first two layers and $120 \mu\text{m}$ for the third and fourth TIB layers, providing a hit resolution of $23 \mu\text{m}$ and $35 \mu\text{m}$ respectively. The TOB covers a region out to $|z| < 118$ cm along the beampipe and makes use of thicker ($500 \mu\text{m}$) strip sensors as compared to those used for the TID ($320 \mu\text{m}$) in order to maintain a signal-to-noise ratio greater than 10. The first four layers of the TOB make use of strips with a pitch of $183 \mu\text{m}$, while the strip pitch in layers 5 and 6 is $122 \mu\text{m}$, providing hit resolutions ranging from $53 \mu\text{m}$ to $35 \mu\text{m}$. The strip hit resolutions in the TIB and TOB for 2016

are summarized in Figure 2.8. The last TOB layer reaches an outward radius of 110 cm from the beampipe. The TIB and TOB are complimented by disk layers on both $\pm z$ sides, with the Tracker Inner Disks (TID) consisting of three small disks flanking the TIB and the Tracker EndCaps (TEC) consisting nine larger disks flanking the TOB. The pitch for the 320 μm thick micro-strip detectors employed in the TID varies from 100 μm to 141 μm . The TEC has a positive (TEC+) and negative (TEC-) z side, where the nine disks on either side extend from $124 < |z| < 282$ cm and radially from $22.5 < |r| < 113.5$ cm. The disks can have up to 7 rings, of which the four innermost are comprised of 320 μm thick micro strip sensors while the fifth through seventh are 500 μm in thickness. A maximum of 9 ϕ hit measurements can be obtain from each TEC disk. In addition, the innermost two layers and disks and of the TIB, TOB and TID, and the first, second and fifth wheel of the TEC+/- disks are comprised of double-sided strip modules where the second module is mounted back-to-back at a stereo angle of 100 mrad in order to make it possible to compute a two-dimensional position measurement by also providing the z coordinate in the barrel and r coordinate on the disks, along with the ϕ .

The layout of the inner tracker guarantees approximately 9 hit measurements up to $|\eta| < 2.4$, at least 4 of which are 2D measurements. The performance of the tracker is gauged by the resolutions for the p_T , the transverse impact parameter (d_0), and the longitudinal impact parameter (z_0) expected for single muons of varying p_T . In the case of single muons with a p_T of 10 and 100 GeV, (i.e. the range considered in the following search), the p_T resolution is 0.65% and 1.5% respectively at $\eta = 0$, and reaches 1 – 2% for $|\eta| = 1.6$.

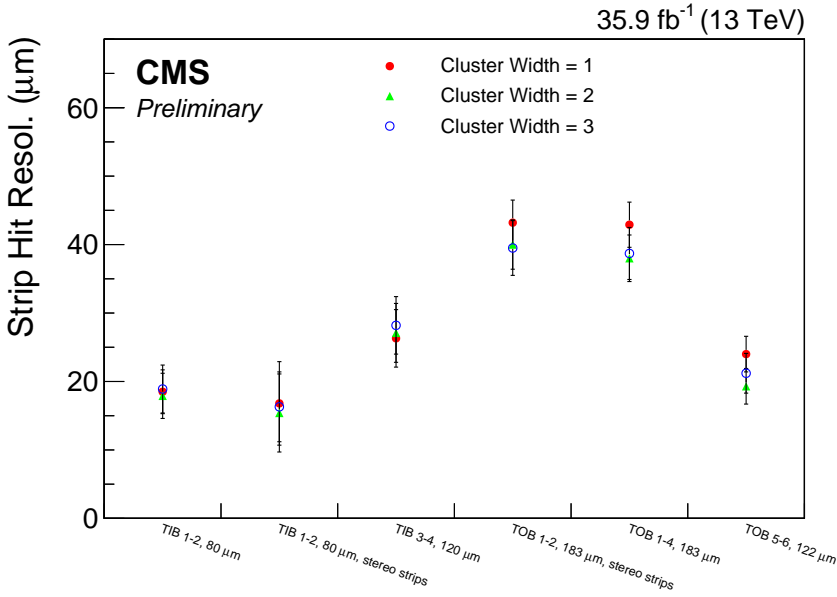


Figure 2.8.: The strip hit resolution for the TIB and TOB layers which are comprised of Si sensors with varying strip pitch. The tracks selected have $p_T > 3 \text{ GeV}$, at least 6 hits in the inner tracker, and χ^2 probability greater than 9.

2.2.3. The calorimeters

Along with tracking information, in order to measure hadronic jets or to infer the presence of neutral particles within the detector volume such as π^0 's or photons (γ), a calorimeter system is of utmost importance. The CMS calorimeter system is comprised of an electromagnetic calorimeter and a brass and scintillating hadronic calorimeter.

The ECAL

The ECAL is a hermetic and homogeneous calorimeter which consists of a barrel (EB) region, from $0 < |\eta| < 1.48$, and two endcap regions (EE), from $1.48 < |\eta| < 3.0$. Chosen for its short radiation length (X_0) and correspondingly small Molière radius (R_M), the ECAL is comprised entirely of lead tungstate crystals (PbWO_4). The two quantities are related by,

$$R_M = 0.0265X_0(Z + 1.2), \quad (2.5)$$

where Z is the atomic number. With the ability to emit 80% of the scintillating light within 25 ns, the crystals are fast light emitters with an emission peak located at 425 nm allowing for a suitable combination with photo-detectors [26]. With $X_0 = 0.89$ cm and $R_M = 2.2$ cm, a better electromagentic (EM) shower position and shower separation is achievable because of the compact nature and fine granularity of the detector. The EB crystals are approximately $25.8X_0$ (23 cm) in length and cover an area of $2.6 \times 2.6 \text{ cm}^2$ at the rear, while the EE crystals are $24.7X_0$ (22 cm) in length and cover an area of $3 \times 3 \text{ cm}^2$ at the rear. In dimensions of $\Delta\eta \times \Delta\phi$, the area that is subtended by a crystal in the EB is 0.0175×0.0175 , while the area varies from 0.0175×0.0175 to 0.05×0.05 for the EE crystals. The scintillation light is detected by the use of avalanche photodiodes (APDs) in the EB, with a total of two APDs glued to each crystal. Both the APDs, which operate at a gain of 50, and the crystal scintillation have a temperature dependence of approximately $-2.4\%/\text{ }^\circ\text{C}$, which dictates the operation of the ECAL to within $\pm 0.05\text{ }^\circ\text{C}$. Vacuum photo-triodes (VPTs) are employed in the EE as a cause of their increased radiation resistance compared to the silicon diodes.

In front of each EE, flanking the inner tracker TEC+/- disks sits a preshower detector covering $1.65 < |\eta| < 2.6$ which consists of $2X_0$ and $1X_0$ depth of lead absorber strips, behind which are two orthogonal planes of silicon strip detector. The preshower aids in the discrimination between $\pi^0 \rightarrow \gamma\gamma$ process and Higgs decays of $h \rightarrow \gamma\gamma$.

The ECAL detector is read out from groupings of 5x5 crystals, where the APDs or VPTs are connected to multi gain pre-amplifiers and these gain ranges are fed

to an analog-to-digital converter (ADC) which digitizes the signal at 40 MHz. The transverse energy sum is performed upon the reception of a level one (L1) trigger accept from CMS and subsequently the data stored in a pipeline by the frontend readout card which has been received from the ADCs, is used in the summing. The sum is the so-called ECAL trigger primitive and is sent to the Trigger Concentrator Card (TCC), where ECAL trigger tower energy sums are performed and fed to the Regional Calorimeter Trigger (RCT).

The energy resolution of the ECAL contains three contributions: a stochastic term, a noise term, and a constant term listed in order in the following [27],

$$\frac{\sigma_E}{E} = \frac{2.8\%}{\sqrt{E}} \oplus \frac{12\%}{E} \oplus 0.3\%, \quad (2.6)$$

where the EB energy resolution is obtained using electrons incident on 5x5 arrays of crystals, and the EM showers are reconstructed in a 3x3 matrix of crystals inside the array around the electron impact point.

The HCAL

The hadron calorimeter (HCAL), of which a quarter-view is shown in Figure 2.9, is essential to the measurement of the energy and direction of particle jets which determine quark, gluon, and neutrino energies and directions. In conjunction with the ECAL and the muon system, the HCAL also aids in the identification of electrons, photons and muons. Hadronic calorimetry is in general considered to be more challenging than the EM calorimetry discussed in the above section, in part due to the much larger depth of detector material required to contain a hadronic cascade in comparison to the EM fraction emitted in the ECAL. Furthermore, the energy resolution of the HCAL is

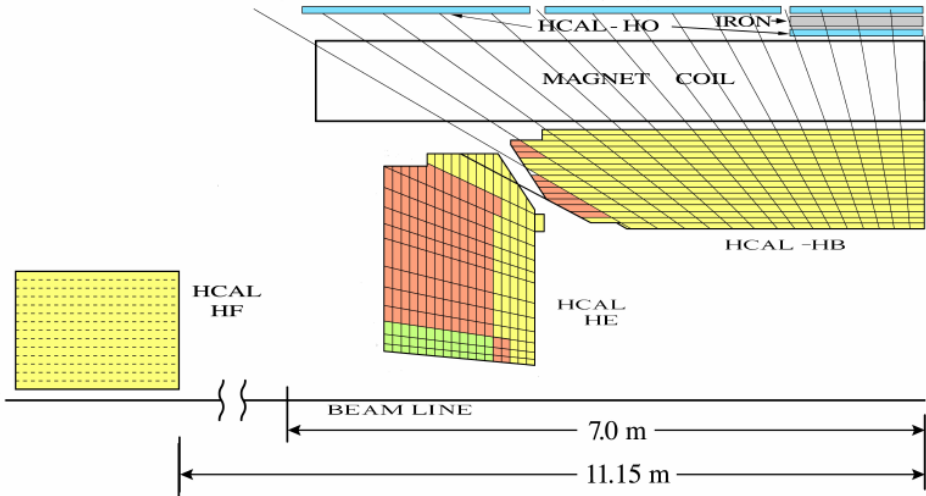


Figure 2.9.: A quarter-view of the CMS hadron calorimeter. The shading indicates the grouping of scintillating layers optically added together to form trigger tower signal readouts. [28]

worsened compared to that of the ECAL by so-called intrinsic fluctuations, which are a result of the significant incoming energy fraction being invisible, since it is employed in processes like nuclear break-up [29].

Located inside the solenoid magnet cryostat, the CMS HCAL consists of four distinctive regions, where the barrel (HB) covers the $|\eta|$ range from 0 to 1.4, while the endcap (HE) covers the $|\eta|$ range from 1.3 to 3.0, thus the HB and HE share the $|\eta|$ range from 1.3 to 1.4. The calorimeter is based on sampling detector technology, and both the HB and HE consist of brass (copper) absorber plates interleaved with plastic scintillator where the sampling fraction is approximately 7%. The HB consists of 18 wedges, where each covers 20° in ϕ and this area is further divided into 5° sectors. The composition and segmentation of the HE is similar, and extends from $388 \text{ cm} < |z| < 5.68 \text{ cm}$ on either $\pm z$ side. The space constraint from the magnet cryostat at $\eta = 0$ requires the HB thickness be limited to approximately 5.8 nuclear interaction lengths (λ_I) and increases to $10\lambda_I$ at $|\eta| = 1.2$. The nuclear interaction length is the mean free path that an incident hadron can travel in a medium before the nuclear interaction

resulting in the absorption of the hadron occurs, and is a material constant that goes as,

$$\frac{1}{\lambda_I} = \sigma_{\text{inel}} \cdot \frac{N_A \cdot \rho}{A} \quad (2.7)$$

where σ_{inel} is the inelastic cross-section, ρ is the density, and A is the atomic mass of the absorber. At $10\lambda_I$, more than 99% of the hadronic cascade is contained within the detector material. In the HB and HE, the scintillation light that is captured is then wavelength shifted, and guided to hybrid photodiodes (HPDs).

In addition to the HB and HE, the main objectives of the forward part of the HCAL (HF) involve the improved measurement of the missing transverse energy and to ensure the identification and reconstruction of very forward jets. The HF covers the $|\eta|$ region from 3.0 to 5.0, and the front face is located at $|z|=11.1$ m from the IP. Due to the high operational luminosity of the LHC and subsequently high average particle multiplicity at the IP per bunch crossing, the inner part of the HF ($4.5 < |\eta| < 5$) is subjected to the largest particle flux, which when absorbed by the detector can reach radiation doses close to 100 Mrad/year. As a result, the HF is constructed with the capability to survive in a high radiation field, hence the absorber is iron and embedded with dual-length quartz fibres parallel to the beam pipe. The HF is segmented into 20° wedges in ϕ where each wedge contains two 10° ϕ sectors. The particles that enter the absorber subsequently produce a shower of particles and those traversing the quartz fibres produce Cherenkov light in the fibres which is guided to the photomultipliers (PMTs). In order to distinguish between showers emitted from e/γ and hadrons, short and long fibres of approximately 165 cm and 22 cm, respectively, are used where

the typical electromagnetic shower is known to be shorter and more collimated than charged hadron showering.

The final part of the HCAL, located outside the solenoid cryostat, is the outer HCAL (HO) which consists of layers of scintillators and serves to catch any energy leakage from the HB. Approximately 5% of particles with $p_T > 100 \text{ GeV}$ deposit some energy fraction in the HO, since complete containment of the hadronic shower in the $3.0 < |\eta| < 5.0$ is not feasible.

2.2.4. The muon detectors

The CMS muon system is used as an exceptionally powerful tool for recognizing interesting physics processes over high background rates, and has a three-fold objective: triggering, identification, and precise momentum measurement. In particular, the latter objective is achieved as a result of the high spatial resolution of the detector and the high magnetic field of the solenoid coil and the flux-return yoke. The CMS muon spectrometer is designed to measure the momentum and charge of muons over a large kinematic range, and operate in high flux regions with non-uniform magnetic field strengths.

Comprised of both a barrel and endcaps, the muon system is situated outside of the magnet solenoid and is interleaved with layers of the steel flux-return yoke. The technologies used in both the barrel and endcaps are three types of gas ionization particle detectors and in all cases throughout the following section, the physical modules are referred to as “chambers”. Since the magnetic field is diminished to approximately 2 T outside of the solenoid magnet and subsequently reverses the muon trajectory, recording several muon track measurements along the trajectory is necessary for the momentum calculation. For this reason, the drift tube (DTs) chambers

used in the barrel are positioned along several values of r in the radial direction and the cathode strip chambers (CSCs) used in the endcaps are positioned along several values of z parallel to the beampipe, as shown in Figure 2.10. There are four stations in the barrel labeled MB1-MB4, and four stations in each of the endcaps labeled ME1-ME4, where a station is an assembly of chambers.

Owing to the low muon rate, along with low neutron background rate expected in the barrel region, and the relatively uniform and weak magnetic field inside the chambers (0.4 T), DTs are employed in this region. Each DT chamber consists of many drift cells, each filled with 85%/15% Ar/CO₂ and having two cathode strips on either side, and electrodes on the top and bottom walls of the cell. A singular 50 μm gold-plated anode wire operating at +3.6 kV is centrally located within the cell volume. Meanwhile the cathodes are operated at -1.8 and +1.8 kV respectively, thus if a muon is incident on the DT, the electrons released in the gas volume drift to the anode and produce avalanches in the increasing field inside the cell. A DT chamber is comprised of three superlayers, where one is placed orthogonally to the remaining two so as to obtain both an $r - \phi$ and $r - z$ position measurement. A superlayer consists of four staggered layers of cells.

Conversely to the barrel case, both the muon rate and the neutron background rate are much higher in the endcaps, thus CSCs are used for their fast response time, owing to the short drift path. The endcaps are also subjected to a higher and non-uniform magnetic field and the CSCs, unlike the DTs, can tolerate this environment. Another benefit to the use of CSCs is their ability to be finely segmented providing an increased momentum resolution. Covering an $|\eta|$ region of 0.9 to 2.4, there are four stations of chambers mounted onto the faces of steel disks perpendicular to the beam line, and each chamber consists of 6 layers of CSCs with cathode strips running radially out, while the 50 μm diameter anode wires run perpendicularly to the strip orientation

and are spaced out by 3.16 - 3.12 mm distances. Each station provides the muon position in $r - \phi$. The CSCs are multi-wire proportional counters with cathode strips which allow for the precise measurement of the position at which a muon or charged particle crosses the gas gap. The CSC stations are further divided into rings where n denotes the ring number and increases radially outward in the naming convention ME1/n-ME4/n. The innermost ring of the first station (ME1/1) is subdivided into two regions in order to allow for triggering and independent readout from the region closest to the beam line.

In addition to the tracking detector technologies, the CMS muon detector also makes use of resistive plate chambers (RPCs) which are interspersed in the endcaps and barrel between the CSCs and DTs, respectively. Primarily used in fast and independent triggering over a range in $|\eta|$ up to 1.6, the RPCs consist of two gas gaps with readout strips aligned in η between the gas gaps. Charged particles traversing an RPC will ionize the gas in both volumes causing avalanches to generate as a result of the high electric field. The avalanches, in turn, induce an image charged which is caught by the readout strips.

The CMS triggering system relies heavily on the muon detector, where two independent and complementary technologies are employed. The DTs and CSCs in the barrel and endcaps respectively are tracking detectors which provide excellent position and time resolution, whereas the RPCs are used to correspondingly to provide a very good timing resolution, but a cruder spatial resolution. For muons with p_T up to approximately 200 GeV, the momentum resolution is largely dominated by multiple scattering in the steel flux-return yoke, especially in the endcaps, thus the multi-layer CSCs are exploited by the trigger hardware processor in order to be able to achieve a high precision in constructing the track segments in the chambers. With the large number of layers and consequently track segments, sharp p_T trigger thresholds at

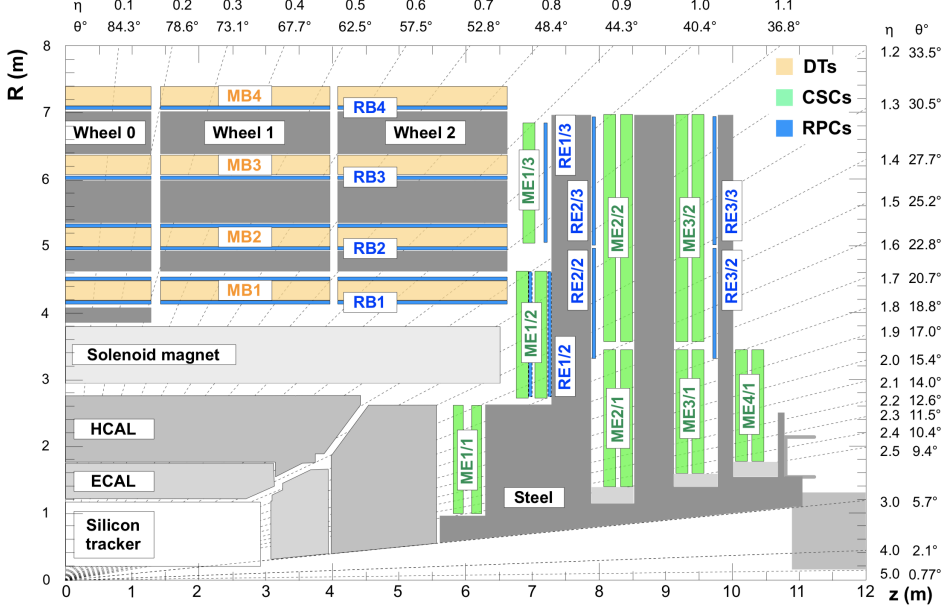


Figure 2.10.: A quadrant view of CMS where the IP is at the lower left corner. The dark grey areas denote the locations of the various muon stations and the steel disks. The 4 drift tube (DT, in light orange) stations are labeled MB (muon barrel) and the cathode strip chambers (CSC, in green) are labeled ME (muon endcap). The resistive plate chambers (RPC, in blue) located in the barrel and the endcaps of CMS, are labeled RB and RE, respectively.

L1 are achieved for muons with p_T up to approximately 100 GeV. The muon trigger system consists of three hierarchical layers, the first of which is called the “local” trigger and makes use of the individual chamber information. This local chamber trigger information is combined to form a “regional” trigger for each of the DT, CSC, and RPC subsystems. Finally, the regional triggers are combined in the “global” muon trigger, which functions as one of the primary L1 triggers. More details on the CMS triggering and readout system can be found in the following section.

2.2.5. The readout system

The 2016 run of the LHC delivered more than 6.5×10^{15} collisions to each of the general purpose detectors. The time spacing of 25 ns between each collision corresponds to a beam crossing frequency rate of 40 MHz. In addition to this exceptionally high

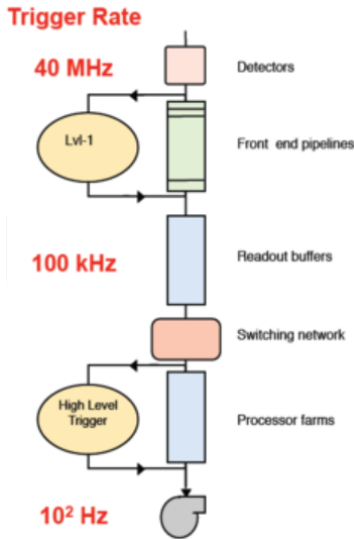


Figure 2.11.: A schematic of the two stage CMS trigger architecture and the corresponding rate reduction at each stage [30].

rate, on average 27 particle interactions per bunch crossing occurred during the 2016 proton-proton run at $\sqrt{s} = 13$ TeV during which the LHC operated at unprecedented luminosities. In addition, the fine segmentation of the CMS subdetectors results in nearly 100 million readout channels and a correspondingly immense volume of data at the sub-detector front-end level. Hence, in order to maintain a high acceptance for events of interest, while simultaneously rejecting QCD multi-jet events which drive the readout rate to high values, CMS employs a two-level robust triggering and detector readout system: a hardware-based Level-1 (L1) trigger which reduces the readout rate from 40 MHz to 100 kHz, and a software-based High-Level trigger (HLT) which further reduces the rate to approximately 200-300 Hz, before storing the data. The architecture of the triggering system can be seen in Figure 2.11.

The L1 CMS trigger system uses information from the previously described calorimeters and muon system to select the most interesting events in a fixed time interval of less than $4 \mu\text{s}$, which allows for $1 \mu\text{s}$ of processing time. The muon trigger, as briefly described in the previous section, uses hits in the DTs and CSCs to construct track stubs at the chamber/sector level before forwarding these to the designated

sub-detector track-finders (DTTF and CSCTF). In order to guarantee the full coverage over the barrel-endcap transition region, these stubs are shared between the TFs. Correspondingly, the RPC uses hits in pattern comparator logic (RPC PAC) to identify potential muon candidates. The trigger primitives from these regional muon triggers are then forwarded to the Global Muon Trigger (GMT) where they are combined and the four best muon candidates in the barrel and endcap are forwarded to the Global Trigger (GT). In addition to the muon trigger, the ECAL and HCAL contribute to the calorimeter trigger. Energy deposits are calculated in barrel trigger towers, which are 0.0875×0.0875 regions in $\eta - \phi$ space, and subsequently sent to the Regional Calorimeter Trigger (RCT). At this stage e/γ candidates are identified and the energy is further summed into $0.35\eta \times 0.35\phi$ regions. This information is then passed to the Global Calorimeter Trigger (GCT) which performs the sorting of e/γ candidates, identifies jets, and energy sums. The GCT then sends the GT 4 isolated and 4 non-isolated e/γ candidates, and 4 jets of each category: forward, central, and tau. In addition, the GCT passes along total and missing energy sums (E_T and \cancel{E}_T), and total and missing scalar sums of transverse jet momenta (H_T and MH_T) [31]. A trigger menu is programmed at the GT level, which consists of approximately 128 trigger algorithms used to make specific requirements on the candidates that have been received from the GCT and GMT. Along with requirements on energy and p_T thresholds of these candidates, the GT is able to require combinations of objects and specify criteria having to do with their relative positions. The decision of whether to keep or discard data from a particular bunch crossing, known as a “L1 accept” is based on whether the trigger primitives, such as the electrons, muons, photons, and jets, pass the set E_T or p_T thresholds, and the total allocated time for the decision is $3.2 \mu\text{s}$.

Following the receipt of an L1 accept, a readout of the front-end electronics signals is performed and events are then processed by the HLT, the second tier of the CMS trigger. The entire CMS HLT system is implemented in a single processor cluster

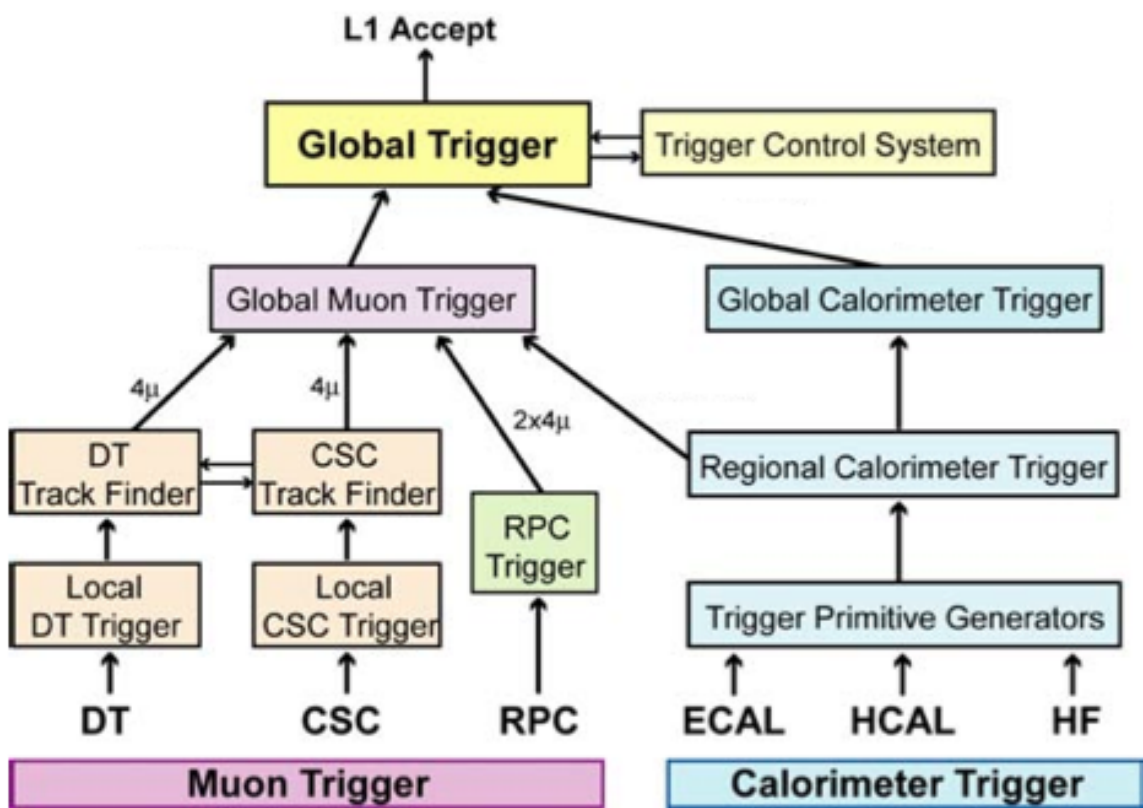


Figure 2.12.: An overview of the CMS L1 trigger where the detector inputs are at the bottom and the subsequent steps in rate reduction proceed vertically upwards.

farm comprised of commercial computers running Linux. This so-called “Event Filter Farm” consists of three main components including the Readout Unit (RU), which is connected to the detector front-end readout and executes the primary step of data concentration by assembling fragments of an event from given detector partitions. Following this, the Builder Unit (BU) performs a full event assembly using the event fragments from the RUs, which are subsequently buffered while they proceed through the final event selection in the Filter Unit (FU) [32]. In order to satisfy the requirements of a high and inclusive selection efficiency for various physics objects, as well as maintain a rate of accepted events within $O(100)$ Hz, the HLT algorithms employed in the FU are as close as possible to those used in standard offline reconstruction.

In order to strike a balance between the fast rejection of uninteresting events and minimization of overall CPU usage, reconstruction and selection at the HLT level makes use of two steps which nearly resemble distinct trigger systems. Denoted as “Level-2” and “Level-3”, the major distinction between the each step is the reconstruction of full tracks in the tracker used at Level-3, where Level-2 solely makes use of information from the calorimeter and muon systems. Track reconstruction requires significantly larger amounts of CPU time than the correlation of calorimeter and muon detector data owing to the high number of readout channels from the inner tracker, the complex pattern recognition algorithms, and the higher rate of combinatorics.

In electron and photon selection, the Level-2 algorithms involve the clustering of energy deposits in the ECAL and the measurement of the cluster energy and position solely from the calorimetric information. Since electrons radiate in the material between the interaction point and the ECAL, and the 4T magnetic field causes bending, the spray of radiated energy reaches the ECAL. The Level-2 algorithm reconstructs the electron energy by clustering cells along a ϕ road, since the radiated spray of energy from the electron is contained in the ϕ direction, to a good approximation. The

following step is termed as “Level-2.5” since only partial as opposed to full tracking information is employed, such that superclusters (groups of energy clusters along the ϕ direction) are matched to hits within the pixel detector. Precise electron position and momentum can be determined solely by using the pixel hits, since most of the tracker material proceeds the pixel layers hence any photon conversions usually take place after these layers. This matching step further divides the electromagnetic triggers into two streams: one for electron candidates and one for photon candidates, which pass much higher energy threshold requirements. At the final stage, the “Level-3” step involves a full track reconstruction which is seeded by the hits in the pixel layers from the previous step [1]. At this stage requirements on the fraction of energy to momentum (E/p) and the distance between the supercluster position and the position extrapolated to the ECAL from the track reconstruction ($\Delta\eta(\text{track} - \text{cluster})$) are made. In the endcaps, requirements on the fraction of energy found behind the ECAL supercluster (in the HCAL) over the supercluster energy (H/E) is made in order to discriminate hadronic activity (i.e. π^0) from e/γ candidates.

For muon selection requirements at the HLT level, the Level-2 algorithm is seeded by the maximum of four muon candidates found by the L1 GMT and employs the digitized hits in the muon detectors to reconstruct and verify the trajectories that lead to the L1 accept. Tracks are reconstructed according to the Kalman filter technique, described in greater detail in Ref. [33], which ameliorates the p_T measurement from L1. Isolation criteria on the basis of the calorimetric energy sum contained within a cone around the muon candidate can be applied at Level-2. The defining feature of the Level-3 muon selection, is the addition of silicon tracker hits to the trajectory which further refines the p_T measurement and provides a sharper trigger threshold. At this final stage, the number of pixel tracks in a region around the muon trajectory projected towards the inner detector can be used to suppress contributions from non-prompt muon decays of b , c , π and K particles.

The HLT algorithm for jet selection is a simplified version of the more involved offline algorithms described in the following chapter dedicated to object reconstruction. The algorithm requires the organization of calorimeter data into towers for which the HCAL segmentation in $\eta \times \phi$ is 0.0875×0.0875 in the barrel and approaches an η segmentation of 0.0175 near the edges of the endcaps. Correspondingly, for each HCAL barrel tower, there are approximately 25 ECAL crystals, whereas in the endcap regions the crystal number varies with η . The basic iterative algorithm for jet finding at HLT consists of designating a “seed tower” which has the highest tower E_T , and using this to calculate the direction of the “protojet”. By determining the transverse-energy-weighted angles of the towers in a cone around the protojet in $\eta - \phi$ space, the direction measurement of the seed protojet is updated and the energy in the cone is summed to obtain the protojet E_T . The procedure is repeated until the protojet energy changes by less than 1% between iterations and the direction in $\Delta\eta^2 + \Delta\phi^2$ space changes by less than 0.01, or on the other hand, 100 iterations have been completed. Towers that are associated with a stable protojet found after this procedure are removed from the listed sorted by descending tower E_T , and the entire jet finding procedure is repeated until no objects remain in the list or conversely, the tower with the highest E_T is below a preset “seed” threshold dictated by the algorithm. More details on the respective parameters such as cone-size, seed energy threshold, and minimum jet energy threshold can be found in Ref. [34].

The ability to use simple trigger requirements to attain high efficiencies for most physics objects is a key feature of the HLT system, along with the flexibility it allows for the modification of existing trigger thresholds or the addition of new triggers should the available computing bandwidth allow for such options. Using a single processor farm, the HLT selection of 1:1000 is achieved and subsequently the data are transmitted to the online and offline computing services.

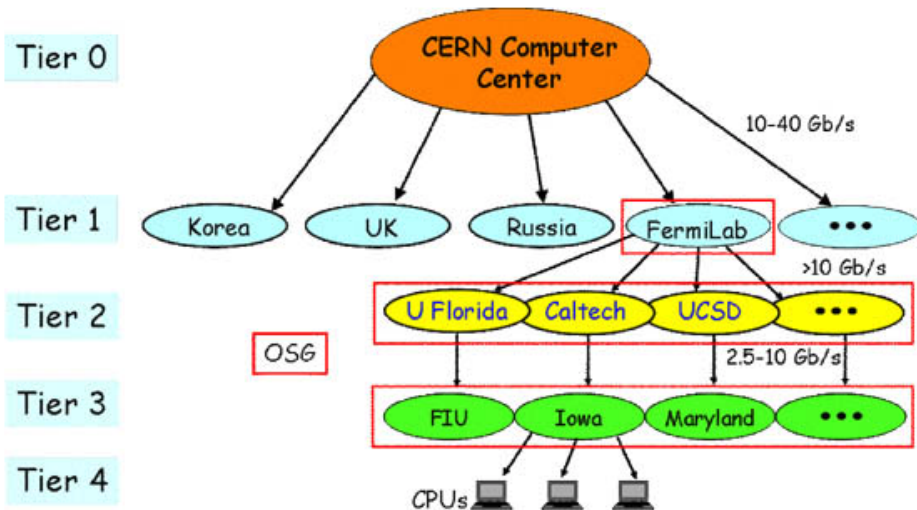


Figure 2.13.: A flow chart of the multi-tier worldwide LHC computing grid, where the components circled in red are examples of the U.S. resources that are part of Open Science Grid (OSG) as defined in detail in Ref. [35]. The computing resources at Northwestern University fall under the Tier 3 computing category.

2.2.6. Computing and Data Storage

The events selected by the HLT for physics analysis, along with events that are selected for calibration purposes, and a fraction of events rejected by the HLT are then processed either online or transmitted to the offline systems for event reconstruction, selection, and any other offline processing. The HLT farm writes “raw” data events of $O(1.5)$ MB size at an approximate rate of 100 Hz which are each classified in approximately $O(50)$ primary datasets, each of which is distinguished according to the trigger objects used at the HLT level. The raw data is processed at CERN’s Tier-0 farm where events are reconstructed with timescales ranging from a few to 24 hours depending on the level of priority. The Tier-0 farm writes out “reco” data events of $O(0.25)$ MB size to one of approximately 6 Tier-1 sites, which produce Analysis Object Data (AOD) events of $O(0.5)$ MB [36]. The AOD events are derived from reco events and contain a copy of the high-level physics objects along with a summary of reco information which enable additional analysis handles such as track refitting. In 2014, in an effort to

reduce the event size while simultaneously retaining all the necessary data from the AOD data formats, a MiniAOD format [37] was introduced as a derivation from the AOD. MiniAOD event sizes are of $O(0.05)$ MB and contain high-level physics objects, along with Particle Flow candidates which are described in the following chapter, and information from the simulated particles. At this stage, the MiniAOD data format can be skimmed according to the objects and selection necessary for data analysis. The multi-tier worldwide LHC computing grid shown in Figure 2.13 displays the full computing chain down to the individual CPUs employed by the end-user, the analyzer.

Chapter 3.

Object and event reconstruction

In order to target $t\bar{t} + \chi\bar{\chi}$ production in the dilepton final state, where both top quarks have leptonically decaying W bosons, the selection criteria is compatible with that of SM $t\bar{t}$ decays in the dilepton final state, but with an additional requirement that the event contain a moderate amount of p_T^{miss} .

Sections 3.1-3.3 are dedicated to detailing the criteria each object in an event must adhere to in order to be considered a potential signal event. Section 4.2 explains how the reconstructed event objects are used together to target a region where a $t\bar{t}(2\ell) + \chi\bar{\chi}$ signal is expected.

3.1. Leptons

A top and anti-top quark are expected in the signal event, and each emits a W^+ and W^- respectively. The W^\pm boson in turn decays to a lepton and its corresponding lepton neutrino, as shown in Figure 3.1. Although the W^\pm boson decays democratically to each lepton generation, only the first and second generation are considered in this

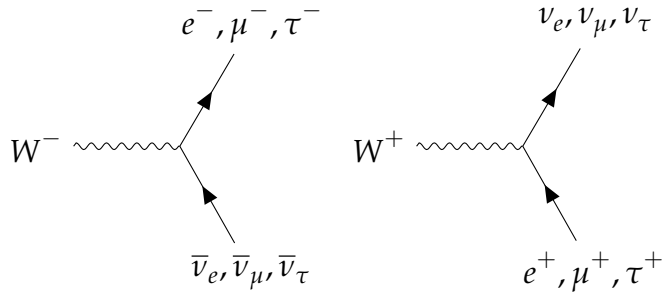


Figure 3.1.: W^+ and W^- decay to leptons and corresponding lepton neutrinos for all lepton generations.

analysis. Namely, since the top and anti-top produce a positively and negatively charged W boson, the final state topology is expected to contain two oppositely charged leptons of either the same lepton flavor or opposite lepton flavor. The term flavor is used to distinguish between the first and second lepton generations. Thus, events with two electrons (ee), two muons ($\mu\mu$), or an electron and muon pair ($e\mu$) are selected. τ leptons are not considered because of challenges in detector reconstruction.

3.1.1. Muons

In order to be selected, muons must pass a stringent set of criteria which guarantee a high muon identification efficiency. The following list of criteria describe the “Tight” working point employed to select a well-identified muon:

- *Global Muon* (outside-in) reconstruction: A standalone muon in the outer muon detectors is matched to a tracker track and a *global-muon track* is fitted, which combines hits from the tracker track and standalone-muon track.
- *Tracker Muon* (inside-out) reconstruction: Tracker tracks with $p_T > 0.5 \text{ GeV}/c$ and $p > 2.5 \text{ GeV}/c$ are taken to be muon candidates and are extrapolated to the muon system, factoring in energy loss expected and the uncertainty from multiple

scattering. An extrapolated track qualifies as a tracker-muon track if it is matched with at least one short stub from DT or CSC hits.

- *Particle Flow Muon* identification: As a general definition, the Particle Flow (PF) algorithm combines information from all CMS subdetectors in order to reconstruct and identify individual particles. For muons, the PF algorithm applies selection criteria on the reconstructed *Global Muon* and *Tracker Muon* dependent on the environment of the muon. The criteria are modified accordingly to the environment, in order to make use of the pertinent sub-detectors. For example, energy deposits in the calorimeter may be used to assign the momentum of a muon that is not well isolated.
- $\chi^2/\text{ndof} < 10$ for *Global Muon* track fit: intended to suppress particles originating from hadronic punchthrough
- At least one muon-chamber hit included in *Global Muon* track fit: This requirement is intended to suppress particles originating from hadronic punchthrough and muons coming from in-flight decays
- Muon segments in at least two muon stations: A tracker track must be matched to these segments, using more than 10 inner-tracker hits, with at least 5 tracker layers containing hits, and at least one pixel hit. This suppresses the punchthrough rate, any accidental track-to-segment matching, and guarantees a good p_T measurement.
- $|d_{xy}| < 2 \text{ mm}$: The tracker track must have a transverse impact parameter, d_{xy} , less than 2 mm with respect to the location of the primary vertex iteration point. This requirement is intended to suppress backgrounds from cosmic muons and further suppress muons originating from in-flight decays.

- $|d_z| < 5$ mm: The tracker track must have a longitudinal distance, d_z , less than 5 mm with respect to the location of the primary interaction vertex in order to further suppress cosmic muons, muons originating from in-flight decays, and tracks from pile-up.

In addition to the aforementioned selection criteria, to further reduce contamination from jets, muon candidates are required to be isolated from all other reconstructed particles within a radius of 0.4 according to the isolation variable defined as,

$$I = I_{h^+} + \max\left(I_{h^0} + I_\gamma - 0.5 \cdot I_{\text{pu}}, 0\right). \quad (3.1)$$

where h^+ , γ , and h^0 correspond to charged hadrons, photons, and neutral hadrons, respectively, and each I quantity is the sum p_T (sum E_T for γ , and h^0) of these particle types in the $R = 0.4$ cone. I_{pu} is the contribution from charged hadrons from pileup and is referred to as the $\Delta\beta$ correction meant to account for effects of additional charged particles not associated with the primary vertex. The value computed in Eq. 3.1 is divided by the muon p_T which is not included in the calculation, hence the value is turned into a relative isolation, I_{rel} . Muons in the event are required to have a relative isolation of less than 0.15.

A looser set of muon identification and isolation requirements are also used in this analysis. In one case the “Fake-able Object” (FO) working point is employed in a background estimation method described later. In addition, a “Loose” muon identification and isolation working point is also used to veto any additional muons in an event. The three muon working points are summarized in Tab. 3.1.

Variable	FO WP	Loose WP	Tight WP
PF-muon	true	true	true
global muon	-	-	true
global OR tracker muon	true	true	-
χ^2/ndof of global muon fit <	-	-	10
No. of muon chamber hit in global muon fit \geq	-	-	1
No. of muon stations with muon segments \geq	-	-	2
$ d_{xy} \text{ (cm)} <$	-	-	0.2
$ d_z \text{ (cm)} <$	-	-	0.5
No. of pixel hits $>$	-	-	0
No. of tracker layers with hits $>$	-	-	5
relative isolation <	0.4	0.25	0.15
track isolation <	0.4	-	-

Table 3.1.: Variables and thresholds that define “FO”, “Loose”, and “Tight”. “-” indicates the variable is not considered for that working point.

3.1.2. Electrons

Electrons must also pass a stringent set of selection requirements in order to be considered a candidate component of the signal event. The criteria are outlined in the following list:

- $\sigma_{i\eta i\eta}$: This variable describes the lateral extension of the hadronic shower along the η direction. It is defined as,

$$(\sigma_{i\eta i\eta})^2 = [\sum (\eta_i - \bar{\eta}) w_i] / \sum w_i \quad (3.2)$$

and the sum runs over the 5x5 matrix of crystals around the highest E_T crystal of the supercluster (SC), and w_i denotes a weight that is logarithmically dependent on the contained energy.

- $|\Delta\phi_{in}| = |\phi_{SC} - \phi_{in}^{\text{extrap}}|$: This denotes the azimuthal separation between the SC energy-weighted ϕ position and the track ϕ extrapolated from the innermost track position and direction to the point of closest approach (PCA) to the SC.
- $|\Delta\eta_{in}| = |\eta_{SC} - \eta_{in}^{\text{extrap}}|$: This denotes the lateral separation between the SC energy-weighted η position and the track η position extrapolated from the innermost track position and direction to the PCA to the SC.
- H/E : The ratio between the energy deposits in the HCAL and ECAL supercluster.
- $|1/E - 1/p|$: This quantity expresses an energy-momentum matching requirement using the SC energy, E , and the track momentum, p , at the PCA to the track vertex. The requirement helps to reject backgrounds from hadronic activity where the spread of the E is not localized resulting in a low E/p , but also backgrounds where a π^0 decays to e^+e^- in the close vicinity of a charged hadron, resulting in a very high E/p ratio.
- $|d_{xy}|$: The transverse impact parameter of the tracker track with respect to the primary interaction vertex.
- $|d_z|$: The longitudinal impact parameter of the tracker track with respect to the primary interaction vertex.
- Missing hits: After track-fitting is performed to electron-tracks seeded by an ECAL crystal with maximum energy in a considered region, if several tracker hits are found to be compatible with those expected in a layer from the track trajectory, at most one missing hit is allowed for an accepted candidate. Furthermore, in order to avoid the inclusion of hits originating from bremsstrahlung photons converted to e^+e^- pairs, in the reconstruction of primary electron tracks, an increased χ^2 penalty is applied to trajectory candidates which have one missing hit.

- Pass conversion veto: In order to reject secondary electrons produced in the conversion of photons in the tracker material, a vertexing algorithm is used. The hits in the tracker from the converted photon are fit to a common vertex using the well-defined topological constraint that tracks from conversions have virtually the same tangent at the conversion vertex in both the (r, ϕ) and (r, z) planes. The converted photon candidates are rejected according to the χ^2 probability of the fit.

In addition to the aforementioned selection criteria, electrons are required to be isolated from nearby activity, namely significant energy flow that may be a result of misidentified jets or that may be due to genuine electrons within a jet resulting from a semileptonic b or c quark decay. Similarly to the isolation definition for muons in Eq. 3.1, the electron isolation definition is a sum of PF-candidates within $R = 0.3$ of the electron. Explicitly, the isolation is computed as,

$$I = I_{h^+} + \max \left(I_{h^0} + I_\gamma - A_{eff} \cdot \rho, 0 \right), \quad (3.3)$$

where I_{h^+} , I_{h^0} , and I_γ are the contributions from charged hadrons, neutral hadrons, photons, respectively. ρ denotes the event energy density. Effects due to pileup are mitigated using corrections based on the “effective area”, denoted as A_{eff} in Eq. 3.3. In order to obtain the A_{eff} , the isolation is plotted as a function of ρ in bins of η , and the value at which the isolation is 90% efficient is determined in slices of ρ , known as the cutoff. A first order polynomial is fit to the cutoff and the slope is taken as the value of the correction, as listed in Tab. 3.2 for the various $|\eta|$ ranges.

A looser set of electron identification and isolation requirements are also used in this analysis. In one case the “Fake-able Object” (FO) working point is employed in a background estimation method described later. In addition, a “Veto” electron identi-

$ \eta $ range	A_{eff}
0.0 – 1.0	0.1703
1.0 – 1.479	0.1715
1.479 – 2.0	0.1213
2.0 – 2.2	0.1230
2.2 – 2.3	0.1635
2.3 – 2.4	0.1937
2.4 – 2.5	0.2393

Table 3.2.: Effective areas for electron isolation PU subtraction.

fication and isolation working point is also used to veto events with any additional electrons. The three electron working points are summarized in Tab. 3.3, for both the barrel and endcap regions, where an electron is defined as being in the barrel if it has a supercluster $|\eta| < 1.479$.

Variable	FO WP		Veto WP		Tight WP	
	Barrel	Endcap	Barrel	Endcap	Barrel	Endcap
$\sigma_{i\eta i\eta} <$	0.011	0.031	0.0115	0.037	0.00998	0.0292
$\Delta\eta_{in} <$	0.04	-	0.00749	0.00895	0.00308	0.00605
$\Delta\phi_{in} <$	0.02	-	0.228	0.213	0.0816	0.0394
H/E	0.06	0.06	0.356	0.211	0.0414	0.0641
$ 1/E - 1/p <$	0.013	0.013	0.299	0.15	0.0129	0.0129
$ d_{xy} \text{ (cm)} <$	0.1	0.2	0.05	0.10	0.05	0.10
$ d_z \text{ (cm)} <$	0.373	0.602	0.10	0.20	0.10	0.20
No. of missing expected hits \leq	1	1	2	3	1	1
relative isolation $<$	-	-	0.175	0.159	0.0588	0.0571
relative ECAL PFCluster iso $<$	0.16	0.12	-	-	-	-
relative HCAL PFCluster iso $<$	0.12	0.12	-	-	-	-
relative track iso $<$	0.08	0.08	-	-	-	-
pass conversion veto	true	true	true	true	true	true

Table 3.3.: Variables and thresholds that define “FO”, “Veto”, and “Tight” electrons. An electron is in the barrel if it has supercluster $|\eta| < 1.479$, otherwise it is in the endcap.

3.2. Jets

Jets are reconstructed from particle candidates obtained by the PF algorithm, using the anti- k_T clustering algorithm with size parameter, $R = 0.4$.

The anti- k_T algorithm is part of a group of sequential jet clustering algorithms that make use of the distance between candidate particles and their respective energies when forming a jet. Such algorithms make the assumption that the particles contained in a jet have minimal differences in p_T , hence the grouping is performed based on momentum-space. These algorithms share a similar underlying method where a distance is computed between two candidate particles according to:

$$d_{ij} = \min \left(p_{T_i}^a, p_{T_j}^a \right) \times \frac{R_{ij}^2}{R} \quad (3.4)$$

where $R_{ij} = (\eta_i - \eta_j)^2 + (\phi_i - \phi_j)^2$ is the $(\eta - \phi)$ distance between the two particles and R is the radius parameter of the jet cone. These methods also require the computation of a second distance variable, $d_{iB} = p_{T_i}^a$, the momentum-space distance between the beam axis and the candidate particle. Subsequently, the minimum of the entire set d_{ij}, d_{iB} is determined and if d_{ij} is the minimum, then particles i and j are combined by the summation of their respective four-vectors, and removed from the list of particles. If d_{iB} is determined as the minimum, the candidate i is taken as the final jet and removed from the list of particles. The process is repeated until either a desired number of jets have been found (exclusive), or the separation between particles in a jet, R_{ij} , is greater than the jet size parameter R (inclusive).

In the anti- k_T algorithm, the value of a corresponds to -2, such that Eq. 3.4 results in,

$$d_{ij} = \min\left(\frac{1}{p_{Ti}^2}, \frac{1}{p_{Tj}^2}\right) \times \frac{R_{ij}^2}{R} \quad (3.5)$$

and $d_{iB} = \frac{1}{p_{Ti}^2}$. The anti- k_T algorithm is minimally affected by activity from the underlying event and pile-up, since Eq. 3.5 is dominated by high p_T particles, so the algorithm preferentially begins clustering hard particles, causing the jet area to fluctuate a small amount.

In order to reduce the effects of “in-time” pile-up, that is additional pp collisions occurring in the same bunch-crossing as the collision of interests, a charge hadron subtraction (CHS) treatment is performed during the anti- k_T clustering of PF jets. The CHS technique removes any charged hadrons well-matched to PU vertices, allowing for the clustering of remaining PF candidates to form jets. In the PF algorithm, a charged hadron is defined as a track possibly associated with hits in the ECAL and HCAL. In order to determine a primary vertex, the proto-vertex with the largest magnitude of the sum of squares of the track transverse momenta ($\sum |p_T^{TRK}|^2$) is chosen. Subleading vertices are deemed as originating from PU and their minimum degrees of freedom, N_{dof} , in the vertex fit is required to be larger than four. Based on the chi-square per degree of freedom ($\chi^2/d.o.f$), a charged hadron can be assigned to the chosen PV if this value is less than 20, otherwise it is associated to a PU vertex. The final step of the CHS procedure entails the removal of PU tracks which are determined by the association of the charged hadron track to a good PU PV. The tracks associated to the PV, and any other tracks not associated to the PU vertices, are kept. The primary effect of the application of CHS is the removal of jets from pileup, although the procedure also improves the angular and p_T resolution of jets, along with reducing the rate of low p_T jets created solely from PU in the tracker acceptance region ($|\eta| < 2.5$).

Furthermore, a set of loose identification criteria on the relative fractions of reconstructed PF jet constituents are imposed in order to suppress noise contributions from the HCAL and ECAL. The PF candidates are denoted as “charged EM” (electron or muon), “neutral EM” (photon), “charged hadron”, and “neutral hadron”, and the requirements are made on the relative jet energy fraction that are carried by each type. Tracker acceptance limits the validity region of the “charged” variables to $|\eta| < 2.4$, however the “neutral” variables extend up to $|\eta| < 5$. The “loose” PF jet identification working point defined in Tab. 3.4 targets the removal of jets emerging from calorimetric noise.

Variable	$ \eta < 2.7$	$2.7 < \eta < 3$	$ \eta > 3$
Neutral Hadron Fraction	< 0.99	< 0.98	-
Neutral EM Fraction	< 0.99	> 0.01	< 0.9
Number of Constituents	> 1	-	-
Number of Neutrals	-	> 2	> 10
<i>Additional cuts for $\eta < 2.4$</i>			
Charged Hadron Fraction	> 0		
Charged Multiplicity	> 0		
Charged EM Fraction	< 0.99		

Table 3.4.: Variables and thresholds that define the “Loose” PF jet ID.

The jet is not considered if it is within $\Delta R < 0.4$ of a “Tight” electron or muon.

3.2.1. b jet tagging

In addition to the preceding jet requirements, an algorithm developed to distinguish jets originating from the hadronization of b quarks is employed in the analysis. This identification relies heavily on the precise reconstruction of secondary vertices associ-

ated to weakly decaying b hadrons present in jets origination from the hadronization of b quarks.

The algorithm, known as the Combined Secondary Vertex (v2) (CSV) makes use of the Inclusive Vertex Finder (IVF), which is exploited in the reconstruction of secondary vertices. The IVF is seeded by a collection of reconstructed tracks in the event which satisfy a loose set of requirements, such that tracks with at least 8 hits in the silicon pixel tracker are selected. The selected tracks must have a p_T greater than 0.8 GeV and the longitudinal impact parameter, the distance between the primary vertex and the track at their point of closest approach, should be smaller than 0.3 cm. In order to create the secondary vertices, the tracks must be displaced, having an IP no larger than $50 \mu m$ and IP significance (IP divided by its uncertainty) of at least 1.2. Clusters are then formed from the displaced seed tracks using requirements on minimum distances and the opening angles between them. An adaptive vertex fitter is used to fit the clusters. The vertex reconstruction algorithm then proceeds with multiple iterations of track arbitration in order to appropriately associate the cluster tracks with the primary or secondary vertex. Each step makes requirements on the fraction of tracks from the secondary vertex shared with the primary and the angular distances between the two vertices.

The CSV algorithm subsequently makes use of the tracks and vertices passing the requirements of the IVF. In the CSV algorithm, at least two displaced tracks identified with the IVF procedure are required within a jet, and furthermore must have an angular distance, ΔR , less than 0.3 with respect to the jet axis. The CSV algorithm categorizes the input vertices into three independent categories. The categories are listed and briefly defined below.

- Jets are associated with at least one reconstructed SV: Vertices are sorted according to increasing uncertainty on the flight distance if more than one reconstructed SV

is found. Most discriminating variables relying on a SV are such that the leading SV is required, such as the vertex mass or the flight distance significance.

- Jets are associated with a “pseudo-vertex”: No vertex fit is applied to candidates satisfying this category since the jet contains at least two tracks incompatible with a window of 50 MeV around the K_s^0 meson mass and a signed IP larger than 2. Since the calculation of a flight distance is not feasible, the discriminating variables are reduced in this category as compared to the previous.
- Jets are not associated with any reconstructed SV or “pseudo-vertex”: This category complements the above two, meaning only variables related to the displaced track vertex are exploited.

The variables defined in each category are combined in each respective category via a multilayer perceptron (MLP) with one hidden layer. An MLP is a type of artificial neural network where the information in each layer is fed uni-directionally to the next. It has the advantage of distinguishing non-linearly separable data. A likelihood ratio taking into account the expected fraction of jet flavors in $t\bar{t}$ events is combined with the information from the three categories, to yield the final CSV discriminant, as shown in Figure 3.2, for multi-jet events where at least one jet satisfies an online p_T requirement of greater than 40 GeV.

3.3. Missing transverse energy

A crucial aspect of this search requires the precise modeling of the missing transverse momentum, denoted \vec{p}_T^{miss} , and its magnitude, referred to as the missing transverse energy, and denoted by p_T^{miss} . Owing to momentum conservation, \vec{p}_T^{miss} corresponds to the transverse momentum that is carried by weakly interacting particles, such

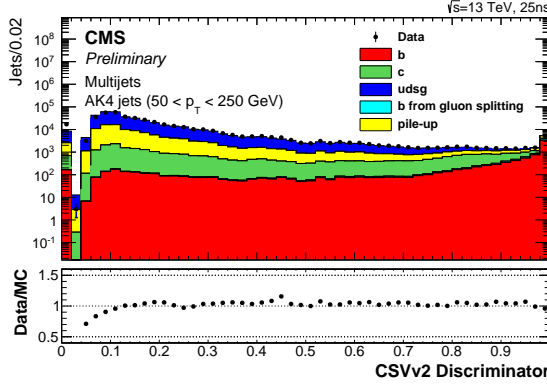


Figure 3.2.: Discriminator values for the CSVv2 algorithm for an inclusive multi-jet topology, where the total number of entries in the simulation is normalized to the observed number of entries in the data.

as neutrinos. This observable is of particular importance in the search for $t\bar{t} + \chi\bar{\chi}$, since the neutral DM particles are also predicted to interact weakly, hence they will escape the detector volume without being detected. Consequently, the measurement of p_T^{miss} relies heavily on the detectable and reconstructed physics objects mentioned in the preceding sections. Thus, p_T^{miss} is defined as the imbalance in the transverse momentum of all particles that interact with the detectors. As mentioned in Sec. , the CMS PF algorithm reconstruction uses all the available detector information to create a list of identified and reconstructed PF particles. It then follows that the \vec{p}_T^{miss} is defined as the negative vectorial sum of the transverse momenta of all PF particles reconstructed in the event, such that,

$$\vec{p}_T^{\text{miss}} = - \sum_{i=\text{PF particles}} \vec{p}_{T_i} \quad (3.6)$$

The measurement of the p_T^{miss} can be mismeasured as a cause of a variety of reasons. The nonlinear response of the calorimeter for neutral and charged hadrons due to its noncompensating nature, minimum energy thresholds in the calorimeters,

inefficiencies in the tracker, or neutrinos from semileptonic particle decays are a sources from which bias can be introduced in the p_T^{miss} measurement. In order to mitigate these biases, the p_T^{miss} derived from PF particles, denoted by $\text{PF-}p_T^{\text{miss}}$, is corrected for using jet energy scale corrections, so Eq. 3.6 then becomes,

$$\text{PF}\vec{p}_T^{\text{miss}} = \text{PF}\vec{p}_T^{\text{miss}} - \sum_{\text{jets}} \left(\vec{p}_{T,\text{jet}}^{\text{corr}} - \vec{p}_{T,\text{jet}} \right) \quad (3.7)$$

All jets with $p_T > 15 \text{ GeV}$ and less than 0.9 of their energy deposited in the ECAL are corrected. In addition, the muon four-momentum is subtracted from the jet four-momentum when the correction is performed, if a muon is found within a jet. Jet energy corrections consist of several stages and are derived and applied in a factorized manner, although the underlying procedure of scaling the jet four-momentum with a scale factor (SF) which depends on jet quantities such as p_T , η , and flavor is universal. The corrections are listed and described briefly below in the order they are applied.

- L1 Pile up: Aimed at removing any energy contributions from pile-up events, this correction is determined from a simulation sample of QCD dijet events which are processed with and without pileup overlay. The corrections are parametrized as a function of the jet area (A), jet η and p_T , and the offset energy density (ρ). The correction applied to data is parametrized in η and determined using zero bias events.
- L2L3 MC-truth corrections: The reconstructed jet p_T is compared to the particle level jet p_T in order to derive jet response corrections from a QCD dijet simulation sample. The jet response is made uniform over p_T and η , the jet variables in which it is derived.

- L2L3 Residuals: These corrections are applied to jets in data and include both an η and p_T component. For the η dependence (relative corrections), dijet events are compared to a jet of similar p_T in the barrel region ($|\eta| < 1.3$). For the p_T dependence (absolute corrections), the JES relative to the reference JES of the barrel jet is taken into account. The jet absolute scale corrections are derived using $Z(\mu \mu/e e) + \text{jets}$, photon+jet, and multijet events.

Chapter 4.

Signal simulation and event selection

4.1. $t\bar{t} + \chi\bar{\chi}$ simplified models

The dark matter collider signal under investigation is characterized by the production of a top quark pair recoiling against a spin-0 mediator which decays to a pair of dark matter particles, as shown in Figure 4.1. As described in greater detail in Sec, this model predicts the production of dark matter via a scalar (ϕ) or pseudoscalar (a) mediator, which couples to SM fermions (in this case top quarks) and the Dirac fermion DM particles, with unitary coupling strength ($g_q = g_\chi = 1$).

The most important characteristic of $t\bar{t} + \chi\bar{\chi}$ models is the p_T of the $\chi\bar{\chi}$ system. This quantity is equivalent to the mediator p_T and is translated to the p_T^{miss} detector observable in an event. The p_T^{miss} spectra for the $t\bar{t} + \chi\bar{\chi}$ models, although dependent on the mediator mass, are expected to peak at higher values than that of the SM $t\bar{t}$ process, owing to the additional contribution from the $\chi\bar{\chi}$ system. In general, the mediator p_T spectrum broadens with increasing mediator mass, as demonstrated in Figure 4.2, where the p_T is shown for various scalar and pseudoscalar mediator masses with

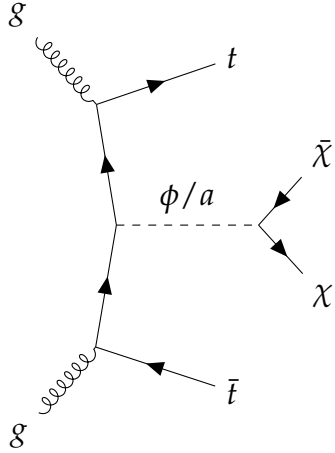


Figure 4.1.: The representative diagram of a top quark pair produced in association with a pair of DM particles ($\chi\bar{\chi}$) which decay via an explicit scalar or pseudoscalar mediator coupled to the tops.

$M_\chi = 1 \text{ GeV}$. It is also the case that at low masses, the pseudoscalar p_T is harder than the scalar p_T of equivalent mediator mass, however the distributions converge to at higher mediator mass. The trend of broadening mediator p_T spectra with increasing mediator mass does not hold in the off-shell regime where the mediator mass is less than twice the DM fermion mass ($2M_\chi > M_\phi$). In the off-shell regime, the p_T of the mediator is not dependent on the mass, and in addition, if the M_χ is varied for a fixed mediator mass, the p_T distribution is harder for the off-shell production rather than the on-shell. Due to the finite mediator width, in the area near the on/off-shell threshold, the kinematics will contain contributions from both types of production, as seen in Figure 4.3.

The $t\bar{t} + \chi\bar{\chi}$ signals are generated in the dilepton final state at LO accuracy in perturbative QCD using MADGRAPH5_AMC@NLO v2.2.2 [38] with up to one additional jet. The MLM parton-jet matching prescription [39] is used to match jets from the matrix element to the parton shower. The spin correlations in the decays of top quarks are preserved through the use of MADSPIN. The partial width formulae given in [40] are used to calculate the minimum decay widths for the mediators. The calculation

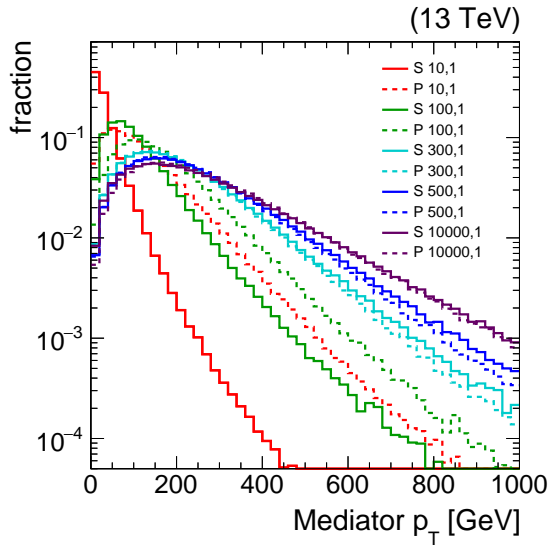


Figure 4.2.: Generator level p_T distributions for scalar (solid lines) and pseudoscalar (dashed lines) mediators, with $M_\chi = 1 \text{ GeV}$, where distributions with the same color have the same mediator mass.

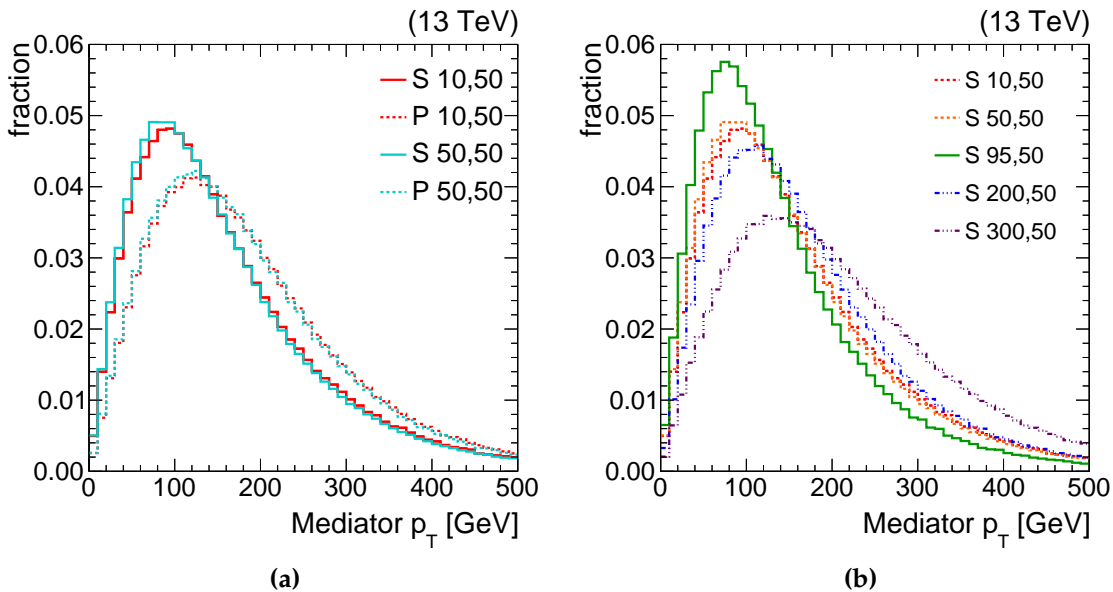


Figure 4.3.: (a) Generator level p_T distributions for off-shell production, with solid lines for scalar and dashed lines for pseudoscalar, and $M_\chi = 50 \text{ GeV}$. (b) Near the on-shell/off-shell threshold (green solid line), the kinematics has contributions from on-shell and off-shell production.

assumes that the mediator couples only to SM quarks and the fermion DM particle (χ), and decays exclusively to a DM pair.

4.2. Signal region event selection

The objects defined in Sec. 3.1-3.3 are all employed to target the selection of events consistent with $t\bar{t} + p_T^{\text{miss}}$ where both tops have leptonically decaying W bosons. The selection is as follows,

- Two “Tight” leptons with opposite charge (ee or $e\mu$ or $\mu\mu$) with $p_T > 25 \text{ GeV}$ for the leading lepton and $p_T > 15 \text{ GeV}$ for the trailing lepton,
- No additional leptons with $p_T > 10 \text{ GeV}$ and passing “Loose” muon or “Veto” electron criter ia,
- Two or more jets where at least one jet is b-tagged,
- $M_{\ell\ell} > 20 \text{ GeV}$,
- $|M_{\ell\ell} - M_Z| > 15 \text{ GeV}$ for ee and $\mu\mu$ events,
- $p_T^{\text{miss}} > 50 \text{ GeV}$,

Dilepton candidate events with an invariant mass $M_{\ell\ell} < 20 \text{ GeV}$ are removed in order to suppress any backgrounds from low-mass Drell-Yan processes, as well as any contributions from heavy-flavor resonances. The requirement for events in the same flavor (ee and $\mu\mu$) channel to have an invariant mass $\pm 15 \text{ GeV}$ away from the Z boson pole mass is also used to reject $Z(\ell\ell)$ background events. The moderate requirement of $p_T^{\text{miss}} > 50 \text{ GeV}$ aims to further suppress contamination from DY events in the same flavor channel.

4.2.1. The $M_{\text{T}2}^{\ell\ell}$ variable

Along with categorization according to lepton flavor (same or opposite), events are also categorized based on the stransverse mass quantity, $M_{\text{T}2}^{\ell\ell}$, defined as,

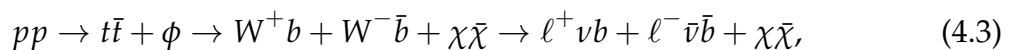
$$M_{\text{T}2}^{\ell\ell} = \min_{\vec{p}_{\text{T}1}^{\text{miss}} + \vec{p}_{\text{T}2}^{\text{miss}} = \vec{p}_{\text{T}}^{\text{miss}}} \left(\max \left[M_{\text{T}} \left(\vec{p}_{\text{T}}^{\ell_1}, \vec{p}_{\text{T}1}^{\text{miss}} \right), M_{\text{T}} \left(\vec{p}_{\text{T}}^{\ell_2}, \vec{p}_{\text{T}2}^{\text{miss}} \right) \right] \right), \quad (4.1)$$

$M_{\text{T}2}^{\ell\ell}$ is partially motivated from the transverse mass, denoted $M_{\text{T}} \left(\vec{p}_{\text{T}}^{\ell}, \vec{p}_{\text{T}}^{\text{miss}} \right)$ in Eq. 4.1, where the most notable use of M_{T} is in the measurement of the W boson mass in the $W \rightarrow \ell\nu$ decay mode. The transverse mass, defined in the context of a leptonic W boson decay, is as follows,

$$M_{\text{T}} = \sqrt{M_{\ell}^2 + M_{\nu}^2 + 2(E_{\text{T}}^{\ell} E_{\text{T}}^{\nu} - \vec{p}_{\text{T}}^{\ell} \cdot \vec{p}_{\text{T}}^{\nu})} \quad (4.2)$$

where M_{ℓ} and M_{ν} are the masses of the lepton and neutrino, respectively, and $\vec{p}_{\text{T}}^{\ell}$ and \vec{p}_{T}^{ν} are their transverse momenta. E_{T}^{ℓ} and E_{T}^{ν} denote their transverse energies.

The utility of M_{T} is best for cases wherein one missing particle is expected (i.e. the neutrino in the leptonic W decay). However, once more than one missing particle is expected in an event, it is no longer possible to calculate the M_{T} since the p_{T} of an individual missing particle cannot be resolved. Recalling that $t\bar{t} + \chi\bar{\chi}$ production and decay follows this route:



a signal event is expected to contain four particles that leave their signature in the detector collectively as \vec{p}_T^{miss} , namely the ν , $\bar{\nu}$, χ , $\bar{\chi}$. Similarly, in the case of the SM $t\bar{t}(2\ell)$ process, the two lepton neutrinos are the sole contributors to the total \vec{p}_T^{miss} , and as postulated by the authors in [41], if the \vec{p}_T^ν and $\vec{p}_T^{\bar{\nu}}$ were obtainable, the maximum M_T value is bounded from above by the W boson mass such that,

$$M_W^2 \geq \max \{ M_T^2 \left(\vec{p}_T^{\ell^+}, \vec{p}_T^\nu \right), M_T^2 \left(\vec{p}_T^{\ell^-}, \vec{p}_T^{\bar{\nu}} \right) \}. \quad (4.4)$$

The partitioning of the \vec{p}_T^{miss} is however unknown, since neither the energy nor direction of either neutrino four-vector can be resolved, so the best that can be assumed is,

$$M_W \geq M_{T2}^{\ell\ell} = \min_{\vec{p}_{T1}^{\text{miss}} + \vec{p}_{T2}^{\text{miss}} = \vec{p}_T^{\text{miss}}} \left(\max \left\{ M_T \left(\vec{p}_T^{\ell_1}, \vec{p}_{T1}^{\text{miss}} \right), M_T \left(\vec{p}_T^{\ell_2}, \vec{p}_{T2}^{\text{miss}} \right) \right\} \right). \quad (4.5)$$

The minimization in Eq. 4.5 occurs over all the possible two-way partitions of \vec{p}_T^{miss} in the event. For the case of the SM $t\bar{t}(2\ell)$ background, a kinematic endpoint in the $M_{T2}^{\ell\ell}$ distribution, shown in Figure 4.4, occurs at the W boson pole mass. With this in mind, two signal regions are formed using the $M_{T2}^{\ell\ell}$ variable, where events with $M_{T2}^{\ell\ell} > 110 \text{ GeV}$ comprise the high signal purity region, since the signal is not expected to be contained in the region below the M_W as is the case for the SM $t\bar{t}(2\ell)$ background. The low signal purity category is formed by the remaining events, for which $M_{T2}^{\ell\ell} < 110 \text{ GeV}$.

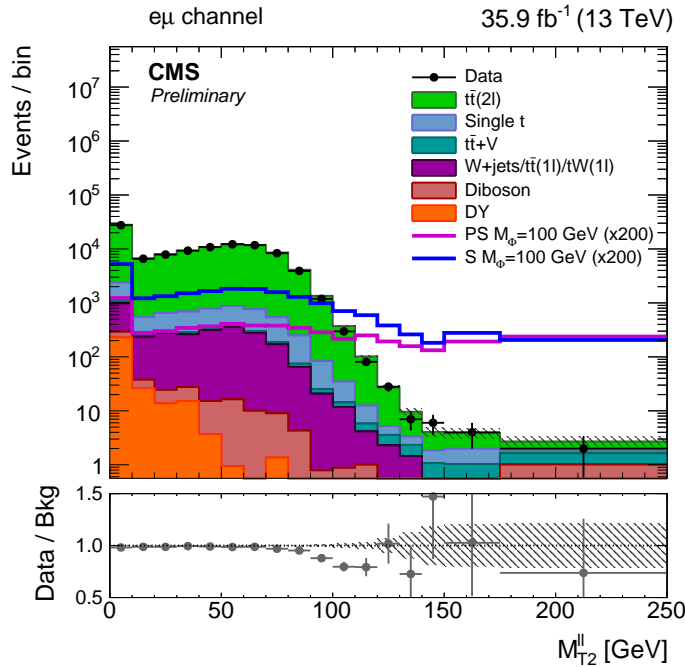


Figure 4.4: The M_{T2}^{ll} distribution in data and simulation for events passing selection requirements for the $e\mu$ channel. The distribution of two example signals (scalar and pseudoscalar mediator, $M_{\phi/a} = 100$ GeV) with $M_\chi = 1$ GeV is scaled up by a factor of 200. The last bin includes overflow. Uncertainties are statistical only.

Chapter 5.

Background processes

Two classes of background processes are present in this search: reducible and irreducible. For the former category, a particle in the background process may “fake” the signature of a particle that is expected in the signal process. On the contrary, in the case of the latter category, the final state topology of the background process yields the same expected particles as a potential signal process. A key feature of reducible backgrounds is the ability to suppress such processes by employing the selection cuts as described in Sec. 4.2. Furthermore, some of the reducible background contributions are estimated using data-driven techniques. In large part, however, the dominant backgrounds in the search are estimated from simulations.

Sec. 5.1-5.4 describe the relevant SM backgrounds in the search for $t\bar{t}(2\ell) + \chi\bar{\chi}$. The production cross sections at $\sqrt{s} = 13$ TeV for these backgrounds are shown in Figure 5.1, giving a sense of the relative importance of the processes. The phase space targeted by the selection requirements as described in Sec. 4.2 also affects the relative hierarchy of the backgrounds, though it remains true that processes with larger cross sections, such as $t\bar{t}$ and Drell-Yan, are dominant in the regions of highest sensitivity.

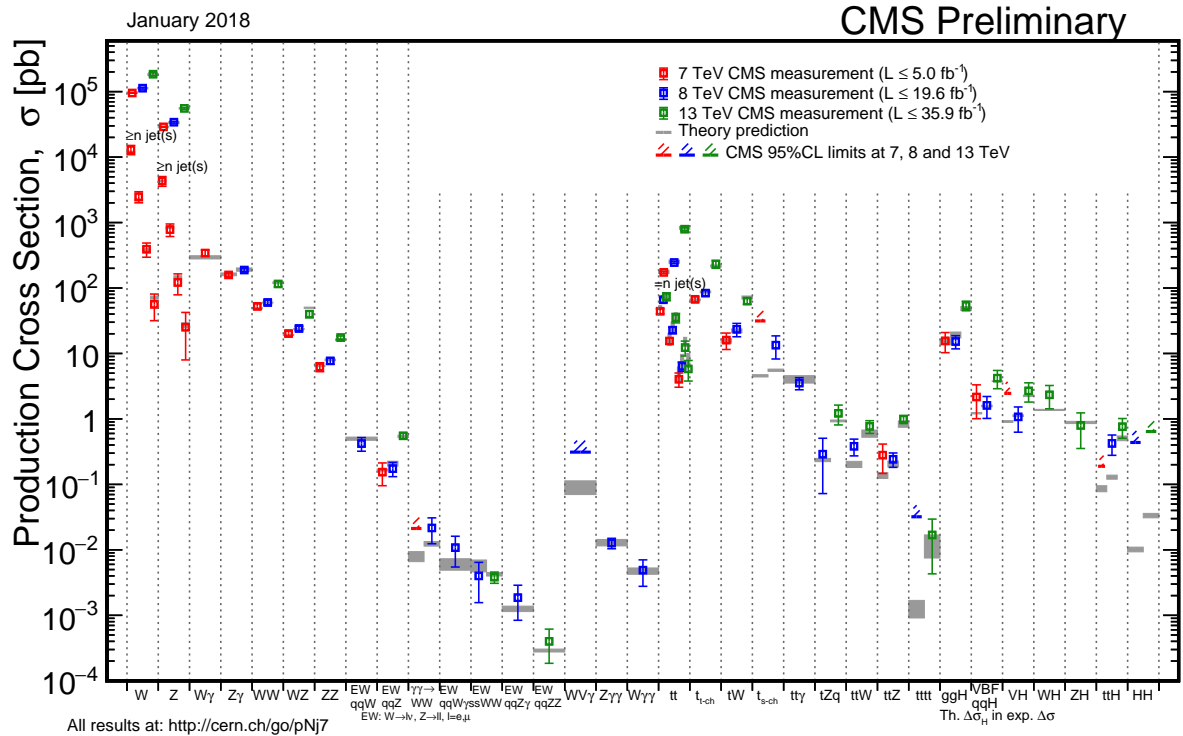


Figure 5.1: Summary of the cross section measurements of SM processes as of January 2018 with data collected by the CMS experiment at $\sqrt{s} = 7, 8$, and 13 TeV .

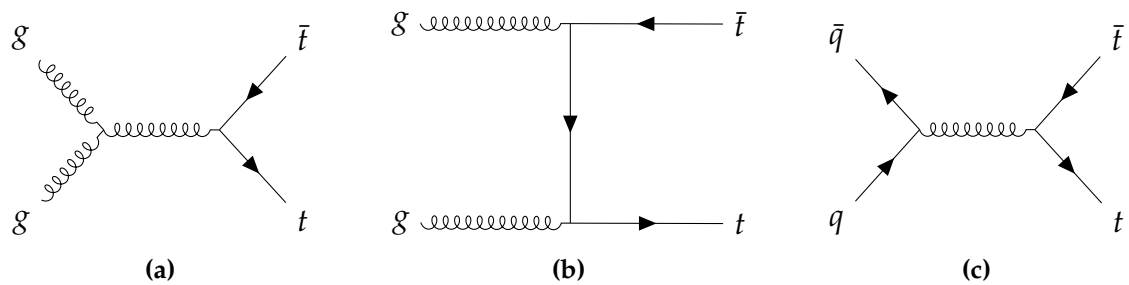


Figure 5.2: Leading order $t\bar{t}$ production diagrams probed at the LHC via (a), (b) gluon fusion, and (c) quark-antiquark annihilation.

5.1. $t\bar{t}(2\ell)$

SM $t\bar{t}(2\ell)$ is the dominant background contribution and is irreducible, owing to the similarity of the final state topology with the signal processes topology. At the LHC, approximately 90% of $t\bar{t}$ events are produced via gluon fusion as shown in Figure 5.2a and Figure 5.2b, in contrast to the Tevatron at Fermilab, where quark-antiquark annihilation shown in Figure 5.2c constituted roughly 85–90% of the relative $t\bar{t}$ production.

The theoretical uncertainties incurred at leading order (LO) in perturbative QCD are quite large for $t\bar{t}$ production. In addition to the LO simulation, the $t\bar{t}$ process decaying to the dilepton final state is simulated at next-to-leading order (NLO) using the POWHEG v2 [42, 43] generator, with the top quark mass assumed to be $m_{top} = 172.5$ GeV. These events are then interfaced to Pythia v8.2 [44] for parton fragmentation, hadronization, and to simulate the underlying event. As pertains to all simulated samples subsequently described, once the $t\bar{t}(2\ell)$ events are showered, the detector response is simulated using the GEANT4 program [45]. Finally, the $t\bar{t}(2\ell)$ events are normalized to the theoretical cross section calculated at next-to-next-to-leading order (NNLO) in perturbative QCD, which also includes soft-gluon resummation calculations at next-to-next-to-leading-order (NNLL) [46–50]. The cross-section folds in the branching fraction of $t\bar{t}$ to the dilepton final state, which is 10.5%. The cross-section value used is $\sigma_{t\bar{t}(2\ell)} = 87.31$ pb.

As mentioned in Sec. 4.2.1, the $t\bar{t}(2\ell)$ background should be suppressed below the kinematic endpoint, M_W , in the $M_{T2}^{\ell\ell}$ distribution. This would only be possible in ideal measurement conditions, however as a cause of detector and energy resolution effects, the mismeasurement of the objects in $t\bar{t}(2\ell)$ background events can contribute to values of $M_{T2}^{\ell\ell} > M_W$.

5.2. $t\bar{t} + V$, diboson, and single top processes

Among the more rare processes considered as backgrounds to this search are processes wherein a top quark pair is produced in association with a boson, denoted as $t\bar{t} + V$ (where $V=\gamma, Z, W$). In particular for the $t\bar{t}+Z$ process, as shown in Figure 5.3a, the same final state is expected as the signal so this process falls under the class of irreducible backgrounds. Although the production cross-sections for $t\bar{t} + V$ processes are orders of magnitude smaller than the $t\bar{t}$ production cross-section, this background is significant in the high $M_{T2}^{\ell\ell}$ categories. The moderate p_T^{miss} requirement is inefficient in $t\bar{t} + V$ background reduction, since large values of p_T^{miss} are expected. In addition, the $t\bar{t}+Z$ process will leak into the high $M_{T2}^{\ell\ell}$ category as a cause of the additional expected p_T^{miss} from the neutrinos, which bias the minimization over all the two-way partitions of the p_T^{miss} , resulting in high values of $M_{T2}^{\ell\ell}$.

The diboson background processes encompass WW , ZZ , and WZ production where all possible final states (i.e. decays to $q\bar{q}, \ell\nu, \ell\ell$, and $\nu_\ell\bar{\nu}_\ell$) are considered for the relevant boson. Owing in part to the largest relative production cross-section, the WW process is the dominant diboson process. In particular, the dilepton signal region requirement targets the final state where both W bosons decay to lepton-neutrino pairs.

The single top background is also expected to contribute sub-dominantly in the signal region. The lepton multiplicity requirement serves to suppress the contributions from s- and t-channel production (i.e. processes whose amplitudes go as $\mathcal{M} \sim 1/s$ and $\mathcal{M} \sim 1/t$, where s and t correspond to the Mandelstam variables), as seen in Figure 5.4a and Figure 5.4b, since only one prompt lepton is expected. Thus, the dilepton final state tW associated production diagram, shown in Figure 5.4c, contributes the most significantly to the single top background.

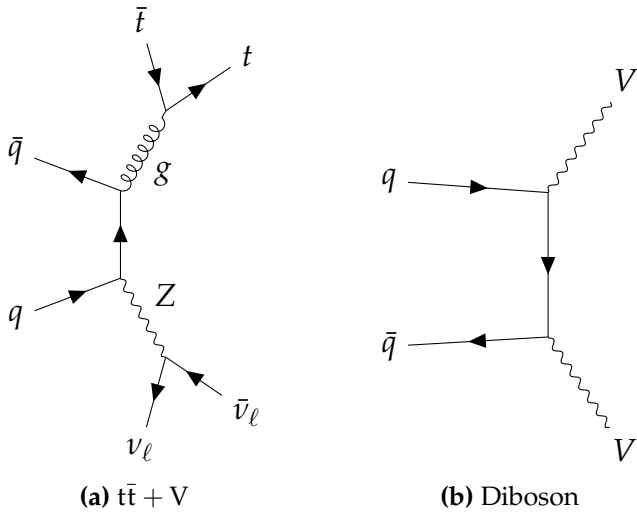


Figure 5.3.: Examples of the (a) $t\bar{t} + V$ process, and (b) diboson production at LO.

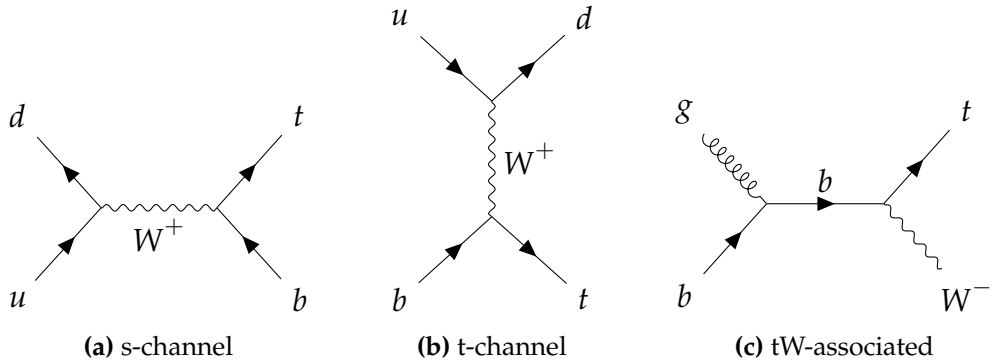


Figure 5.4.: Single top quark production via (a) s-channel, (b) t-channel, and (c) in association with a W boson.

Similarly to the $t\bar{t}(2\ell)$ process, the $t\bar{t} + V$, diboson, and single top processes are simulated at NLO. The $t\bar{t} + V$ processes are generated using `MADGRAPH5_AMC@NLO v2.2.2`. For single top, the s- and t-channel processes are simulated using `POWHEG v2` and interfaced with `MADSPIN` which decays the top and preserves the spin correlation and any finite width effects in narrow resonance decays. The tW channel, on the other hand, is generated using `POWHEG v1` at NLO accuracy and normalized to the approximate NNLO cross-section. The diboson samples are generated at NLO using either `MADGRAPH5_AMC@NLO v2.2.2` or `POWHEG v2`.

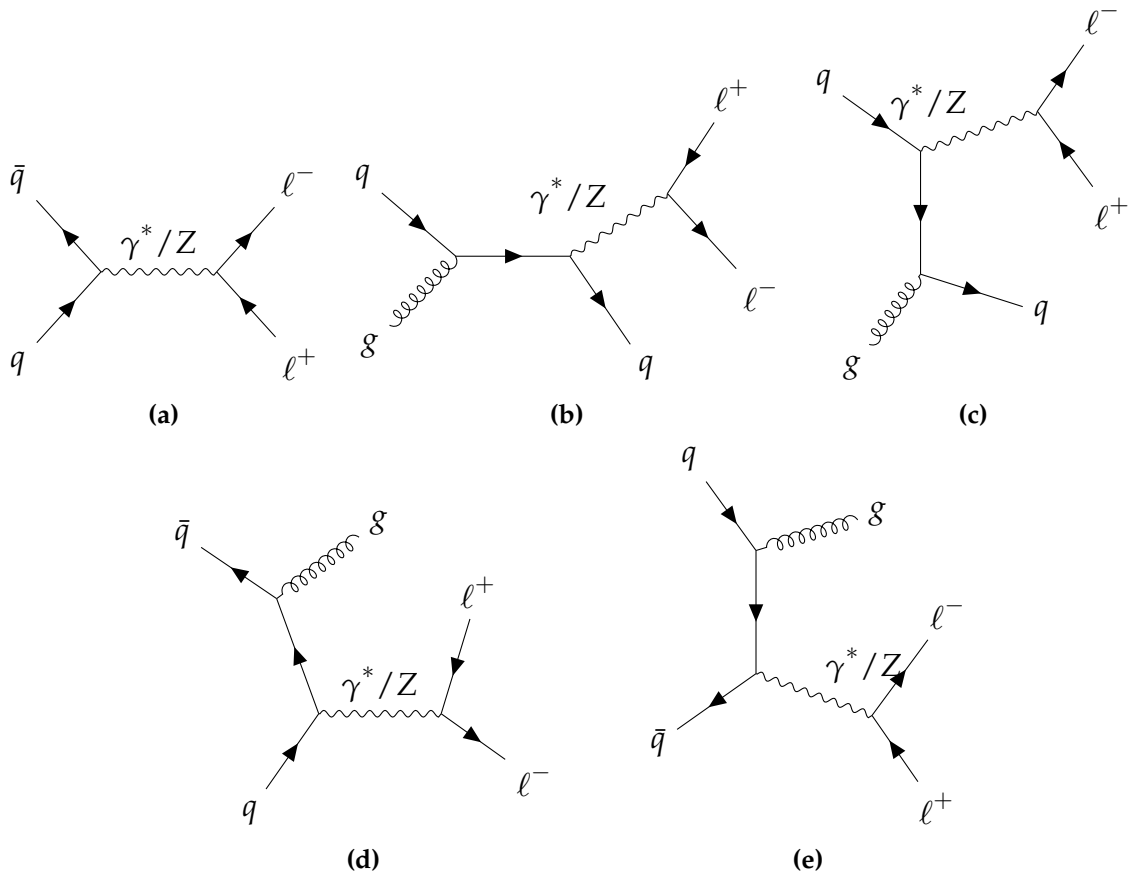


Figure 5.5.: The Drell-Yan lepton pair-production process mediated by a virtual photon (γ^*) or Z boson at (a) $\mathcal{O}(\alpha)$ and (b),(c),(d),(e) $\mathcal{O}(\alpha\alpha_s)$.

5.3. Drell-Yan

From the diagrams in Figure 5.5, the Drell-Yan pair-production process falls under the class of reducible backgrounds, since many of the selection criteria act to suppress processes where the selected same flavor opposite sign (SFOS) leptons are produced at the same vertex, such as from the exchange of a real Z boson or a virtual photon (γ^*). Namely, the requirement for the mass of the selected SFOS lepton pair to be outside of the Z mass window, $75 \text{ GeV} < M_Z < 105 \text{ GeV}$, removes a large contribution of dilepton decays stemming from real Z bosons/off-shell virtual photons. Furthermore, the low dilepton mass requirement, $M_{\ell\ell} > 20 \text{ GeV}$ suppresses the contribution from low mass

decays of J/ψ mesons to SFOS pairs. In addition, the requirement for the event to contain at least two jets, with at least one b-tagged jet acts to eliminate contributions from Figure 5.5a, where the quark-antiquark annihilation to a SFOS pair proceeds at LO in α . The DY process is simulated at NLO using `MADGRAPH5_AMC@NLO` v2.3.3, and thus includes contributions from higher order processes as shown in Figure 5.5b-Figure 5.5e, where at least one jet is expected from the fragmentation and hadronization of particles emitted in initial state radiation.

Although the relative shape of the DY contribution is taken from simulation, a data-driven process is used to estimate the normalization of this background. The signal region still contains a sizeable DY contribution, meaning that exceptional DY events evading the above-mentioned Z boson mass veto tend to be accompanied by a significant amount of p_T^{miss} . Since the instrumental detector effects which influence this final state topology are non-trivial to simulate, it is more appropriate to use calibrated samples from data to arrive at these estimates.

5.3.1. The $R_{\text{in/out}}$ method

The method is used to predict the DY normalization, N_{DY} , by extrapolating from the observed DY yield inside the Z mass window (within $\pm 15 \text{ GeV}$ of M_Z), N_{in} , according to:

$$N_{DY} = N_{in} \frac{R_{MC}^{0b}}{R_{MC}^{1b} \cdot R_{data}^{0b}}, \quad (5.1)$$

where each quantity R in Eq. 5.1 is defined as the ratio of DY yields **inside** to **outside** the Z mass window,

$$R_{\text{in/out}} = \frac{N(|M_{\ell\ell} - M_Z| < 15 \text{ GeV})}{N(|M_{\ell\ell} - M_Z| > 15 \text{ GeV and } M_{\ell\ell} > 20 \text{ GeV})}. \quad (5.2)$$

Hence, the events originally rejected by the Z veto are used to estimate the residual contributions from $DY \rightarrow e^+e^-$ and $\mu^+\mu^-$ in the remaining selected sample. The yields are computed with all other selection cuts applied. Ideally, the $R_{\text{in/out}}$ in a region where the number of b-tagged jets is required to be zero would be equal to the $R_{\text{in/out}}$ in a region where at least one b-tagged jet is required, such that $R_{\text{in/out}}^{0b} = R_{\text{in/out}}^{1b}$. This assumption, however, is invalid since the numerator and denominator in Eq. 5.2 differ significantly when measured in DY simulation with a looser set of selection cuts, such as the removal of the p_T^{miss} requirement or a looser jet multiplicity requirement. A weaker assumption is then made, which is as follows:

$$\frac{(R_{\text{in/out}}^{1b})_{\text{data}}}{(R_{\text{in/out}}^{1b})_{\text{MC}}} = \frac{(R_{\text{in/out}}^{0b})_{\text{data}}}{(R_{\text{in/out}}^{0b})_{\text{MC}}}, \quad (5.3)$$

so the ratio of the measured $R_{\text{in/out}}^{0b}$ between data and MC should be equivalent to the ratio of the measured $R_{\text{in/out}}^{1b}$ between data and MC. Then the estimate for the DY normalization in the signal region as defined in Eq. 5.1 is expanded into,

$$(N_{\text{out}}^{1b})_{\text{data}} = \frac{(N_{\text{in}}^{1b})_{\text{data}}}{(R_{\text{in/out}}^{1b})_{\text{data}}} = \frac{(N_{\text{in}}^{1b})_{\text{data}}}{(R_{\text{in/out}}^{1b})_{\text{MC}}} \cdot \frac{(R_{\text{in/out}}^{0b})_{\text{MC}}}{(R_{\text{in/out}}^{0b})_{\text{data}}} \quad (5.4)$$

Thus, every quantity on the right-hand side of Eq. 5.4 is measured. However, it should be noted that non-DY contributions are present in the measurements made in the data, and hence must be subtracted off from events that fall both inside and outside the Z mass window in the zero b-tag and the one-or-more b-tag regions (i.e. all the quantities N_{in}^{0b} , N_{out}^{0b} , N_{in}^{1b} , and N_{out}^{1b}). The non-DY contributions in the $\{0b, 1b\} \otimes \{\text{in, out}\}$ regions, such as $t\bar{t}(2\ell)$, are estimated from data using opposite flavor (e^\pm, μ^\mp) events, that are denoted by $N_{\text{in}}^{e\mu}$ and $N_{\text{out}}^{e\mu}$. Thus, the number of events in data in each of the aforementioned regions, after the subtraction of non-DY backgrounds is,

$$N = N^{\ell\ell} - 0.5 \cdot k_{\ell\ell} \cdot N^{e\mu}, \quad (5.5)$$

where the 0.5 factor accounts for combinatorics, and $k_{\ell\ell}$ is a correction factor applied to account for the differences in reconstruction efficiencies between electrons and muons. The correction factor is derived from an inclusive selection targeting $Z \rightarrow \ell\ell$, and is defined as,

$$k_{ee} = \sqrt{\frac{N^{ee}}{N^{\mu\mu}}}, \quad k_{\mu\mu} = \sqrt{\frac{N^{\mu\mu}}{N^{ee}}} \quad (5.6)$$

The value for $k_{ee}(k_{\mu\mu})$ measured in data is 0.64 (1.55).

In order to capture any p_T^{miss} dependence of the DY normalization, the various $R_{\text{in/out}}$ quantities are computed in four bins of p_T^{miss} , shown in the fifth column of Table 5.1-Table 5.4, since the relative contribution of DY is expected to drop off at higher p_T^{miss} values and incur larger statistical uncertainties in the simulation. The “on” Z

peak (i.e. $|M_{\ell\ell} - M_Z| < 15 \text{ GeV}$) yields for a 0 b-tag selection listed in the second column of Table 5.1 and Table 5.2 can be seen in Figure 5.6 and Figure 5.7 for the ee and $\mu\mu$ channels, respectively. The predicted DY normalization in the signal region in each p_T^{miss} bin is listed in Table 5.5 and Table 5.6 under the column heading $(N_{\text{out}}^{1b})_{\text{data}}$. The simulation yields, under the column heading $(N_{\text{out}}^{1b})_{\text{MC}}$, are scaled by the factors in the last column of Table 5.5 and Table 5.6, and shown in Figure 5.8 in red and blue markers, respectively for the ee and $\mu\mu$ channel. The dashed line in Figure 5.8 represents the inclusively calculated scale factors, which are not used in the analysis but simply as a cross-check. The larger scale factors for the ee channel are attributed to a broader Drell-Yan line shape in data compared to simulation, while in the $\mu\mu$ channel the line shapes in data and simulation are more similar.

Table 5.1.: DY yields and $R_{\text{in/out}}$ values in the ee channel, for 0 b-tag selection

		$ M_{\ell\ell} - M_Z < 15 \text{ GeV}$	$ M_{\ell\ell} - M_Z > 15 \text{ GeV}$	$R_{\text{in/out}}^{0b}$
$50 \text{ GeV} < p_T^{\text{miss}} < 75 \text{ GeV}$	data	35602.72 ± 191.00	4912.88 ± 92.65	7.25 ± 0.14
	MC	38417.99 ± 233.36	4932.28 ± 155.12	7.79 ± 0.25
$75 \text{ GeV} < p_T^{\text{miss}} < 100 \text{ GeV}$	data	4503.12 ± 72.21	875.04 ± 61.05	5.15 ± 0.37
	MC	5651.58 ± 86.47	865.83 ± 58.83	6.53 ± 0.45
$100 \text{ GeV} < p_T^{\text{miss}} < 150 \text{ GeV}$	data	714.20 ± 37.79	415.24 ± 56.38	1.72 ± 0.25
	MC	746.41 ± 31.32	225.78 ± 21.53	3.31 ± 0.34
$150 \text{ GeV} < p_T^{\text{miss}} < 1000 \text{ GeV}$	data	221.68 ± 22.05	415.24 ± 56.38	0.53 ± 0.090
	MC	55.27 ± 7.33	105.28 ± 11.92	0.24 ± 0.040

Table 5.2.: DY yields and $R_{\text{in/out}}$ values in the $\mu\mu$ channel, for 0 b-tag selection

		$ M_{\ell\ell} - M_Z < 15 \text{ GeV}$	$ M_{\ell\ell} - M_Z > 15 \text{ GeV}$	$R_{\text{in/out}}^{0b}$
$50 \text{ GeV} < p_T^{\text{miss}} < 75 \text{ GeV}$	data	76878.78 ± 282.38	11061.48 ± 151.71	$6.95 +/- 0.099$
	MC	84516.00 ± 353.40	12266.77 ± 277.25	$6.89 +/- 0.16$
$75 \text{ GeV} < p_T^{\text{miss}} < 100 \text{ GeV}$	data	9757.90 ± 109.88	1551.43 ± 104.12	$6.29 +/- 0.43$
	MC	11972.59 ± 130.57	2267.89 ± 104.23	$5.28 +/- 0.25$
$100 \text{ GeV} < p_T^{\text{miss}} < 150 \text{ GeV}$	data	1468.25 ± 61.59	401.18 ± 96.96	$3.66 +/- 0.90$
	MC	1639.18 ± 45.61	646.05 ± 43.72	$2.54 +/- 0.19$
$150 \text{ GeV} < p_T^{\text{miss}} < 1000 \text{ GeV}$	data	305.85 ± 34.16	396.34 ± 97.66	$0.77 +/- 0.20$
	MC	86.42 ± 10.45	290.42 ± 21.26	$0.33 +/- 0.018$

Table 5.3.: DY yields and $R_{\text{in/out}}$ values in the ee channel, for ≥ 1 b-tag selection

		$ M_{\ell\ell} - M_Z < 15 \text{ GeV}$	$ M_{\ell\ell} - M_Z > 15 \text{ GeV}$	$R_{\text{in/out}}^{1b}$
$50 \text{ GeV} < p_T^{\text{miss}} < 75 \text{ GeV}$	data	5236.16 ± 90.60	—	—
	MC	5132.28 ± 84.32	623.60 ± 58.67	$8.23 +/- 0.79$
$75 \text{ GeV} < p_T^{\text{miss}} < 100 \text{ GeV}$	data	1038.20 ± 58.76	—	—
	MC	915.35 ± 34.19	137.98 ± 22.97	$6.63 +/- 1.13$
$100 \text{ GeV} < p_T^{\text{miss}} < 150 \text{ GeV}$	data	289.88 ± 51.08	—	—
	MC	193.95 ± 14.94	27.61 ± 8.35	$7.02 +/- 2.19$
$150 \text{ GeV} < p_T^{\text{miss}} < 1000 \text{ GeV}$	data	154.72 ± 29.57	—	—
	MC	22.96 ± 5.00	17.32 ± 4.47	$1.33 +/- 0.45$

Table 5.4.: DY yields and $R_{\text{in/out}}$ values in the $\mu\mu$ channel, for ≥ 1 b-tag selection

		$ M_{\ell\ell} - M_Z < 15 \text{ GeV}$	$ M_{\ell\ell} - M_Z > 15 \text{ GeV}$	$R_{\text{in/out}}^{1b}$
$50 \text{ GeV} < p_T^{\text{miss}} < 75 \text{ GeV}$	data	10398.33 ± 141.70	—	—
	MC	11001.22 ± 126.39	1444.20 ± 92.95	$7.62 +/- 0.50$
$75 \text{ GeV} < p_T^{\text{miss}} < 100 \text{ GeV}$	data	1689.88 ± 97.73	—	—
	MC	1867.68 ± 50.40	293.68 ± 38.12	$6.36 +/- 0.84$
$100 \text{ GeV} < p_T^{\text{miss}} < 150 \text{ GeV}$	data	372.47 ± 89.03	—	—
	MC	342.57 ± 21.09	113.32 ± 16.96	$3.02 +/- 0.49$
$150 \text{ GeV} < p_T^{\text{miss}} < 1000 \text{ GeV}$	data	100.40 ± 49.44	—	—
	MC	30.05 ± 6.52	41.85 ± 9.82	$0.72 +/- 0.23$

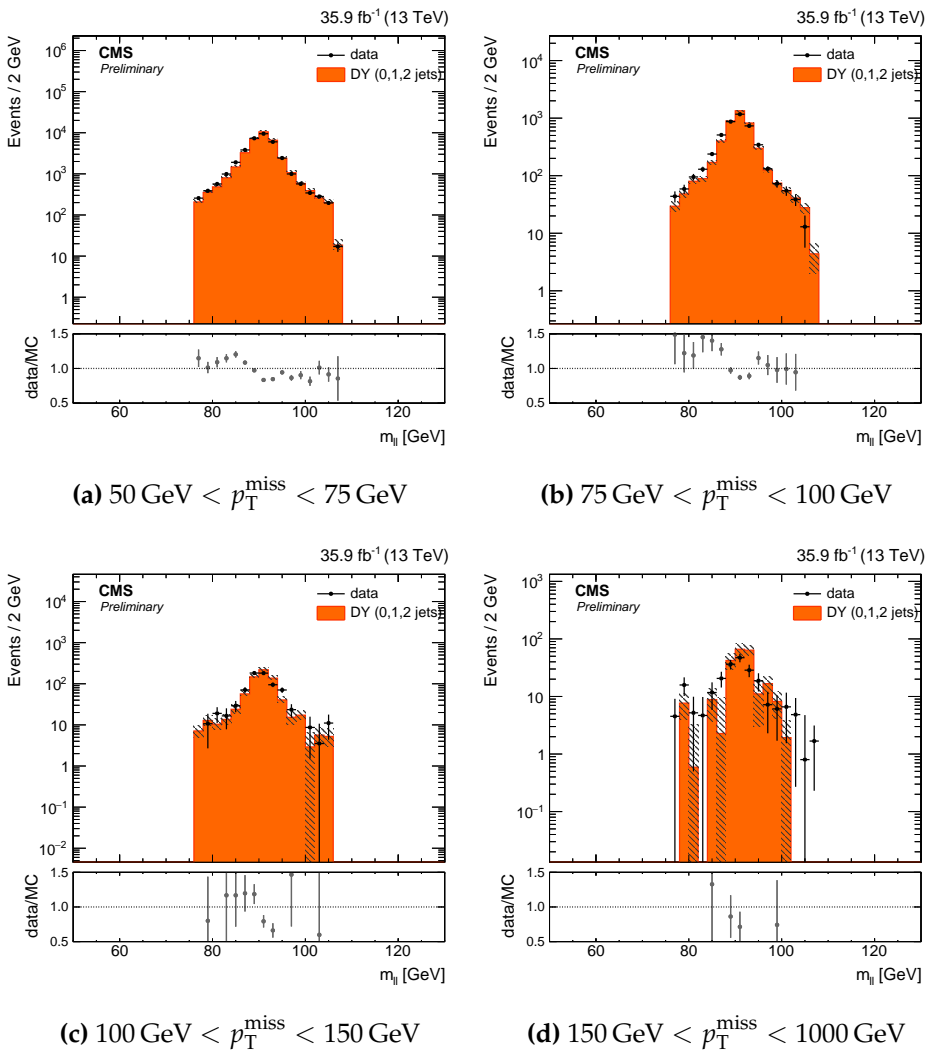


Figure 5.6: Z peak in data and MC after subtraction of non-Drell-Yan contribution estimate from opposite-flavor data events in the ee channel for various p_T^{miss} bins.

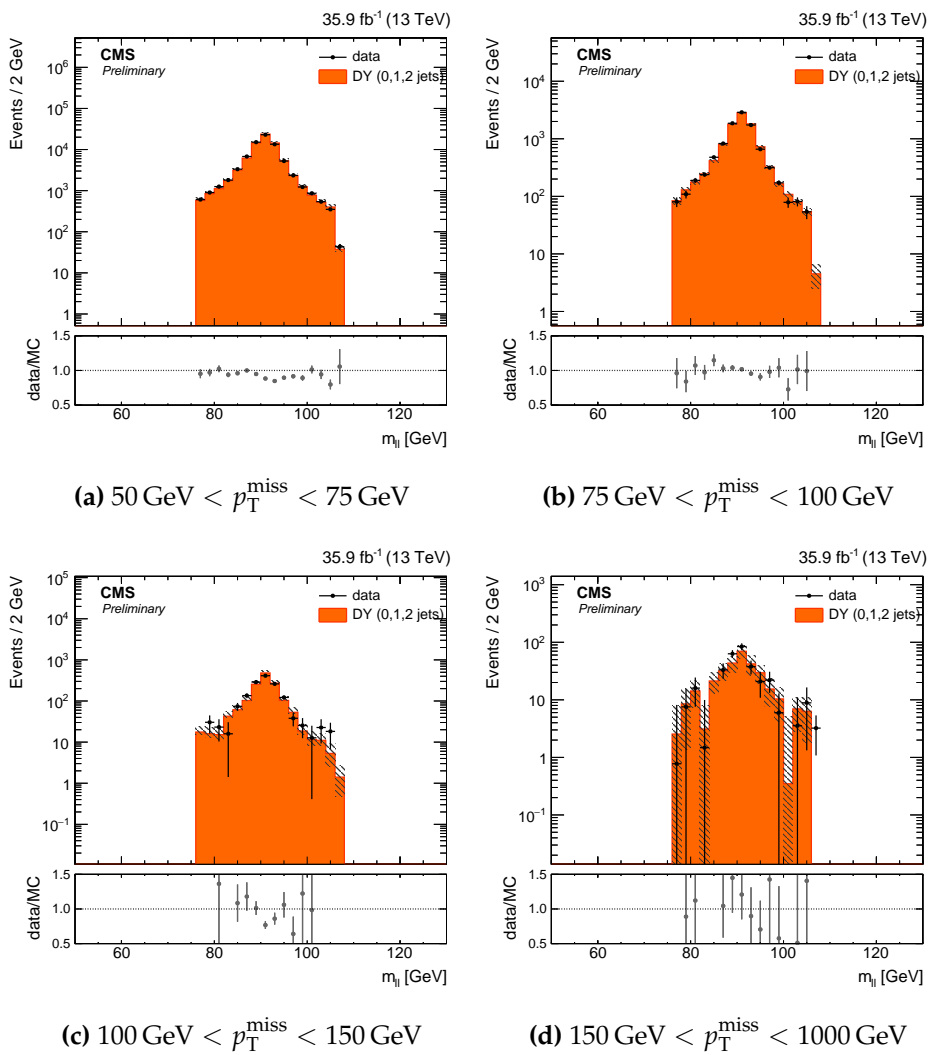


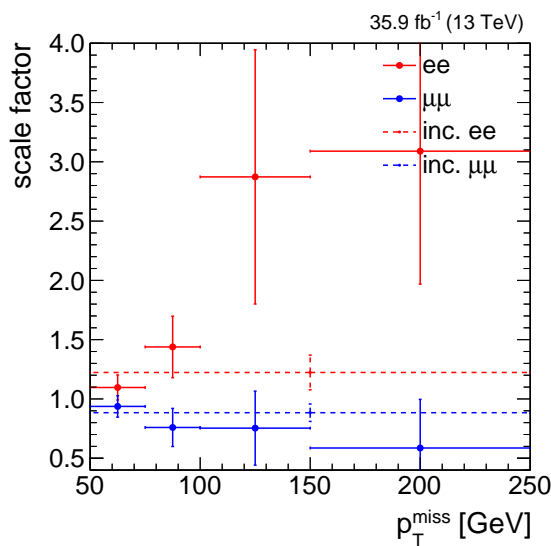
Figure 5.7.: Z peak in data and MC after subtraction of non-Drell-Yan contribution estimate from opposite-flavor data events in the $\mu\mu$ channel for various p_T^{miss} bins.

Table 5.5.: Signal region DY yields in MC and data (from $R_{\text{in/out}}$ prediction) in the ee channel

	$(N_{\text{out}}^{1b})_{\text{MC}}$	$(N_{\text{out}}^{1b})_{\text{data}}$	scale factor
$50 \text{ GeV} < p_T^{\text{miss}} < 75 \text{ GeV}$	623.60 ± 58.67	683.83 ± 13.85	1.10 ± 0.11
$75 \text{ GeV} < p_T^{\text{miss}} < 100 \text{ GeV}$	137.98 ± 22.97	198.51 ± 13.65	1.44 ± 0.26
$100 \text{ GeV} < p_T^{\text{miss}} < 150 \text{ GeV}$	27.61 ± 8.35	79.32 ± 17.34	2.87 ± 1.07
$150 \text{ GeV} < p_T^{\text{miss}} < 1000 \text{ GeV}$	17.32 ± 4.47	53.58 ± 13.66	3.09 ± 1.12

Table 5.6.: Signal region DY yields in MC and data (from $R_{\text{in/out}}$ prediction) in the $\mu\mu$ channel

	$(N_{\text{out}}^{1b})_{\text{MC}}$	$(N_{\text{out}}^{1b})_{\text{data}}$	scale factor
$50 \text{ GeV} < p_T^{\text{miss}} < 75 \text{ GeV}$	1444.20 ± 92.95	1353.21 ± 97.49	0.94 ± 0.091
$75 \text{ GeV} < p_T^{\text{miss}} < 100 \text{ GeV}$	293.68 ± 38.12	223.03 ± 37.18	0.76 ± 0.16
$100 \text{ GeV} < p_T^{\text{miss}} < 150 \text{ GeV}$	113.32 ± 16.96	85.42 ± 32.96	0.75 ± 0.31
$150 \text{ GeV} < p_T^{\text{miss}} < 1000 \text{ GeV}$	41.85 ± 9.82	24.53 ± 16.18	0.59 ± 0.41

**Figure 5.8.:** Data/MC scale factors binned in p_T^{miss} applied to MC events used for the estimate of the Drell-Yan normalization in the dilepton channel signal regions.

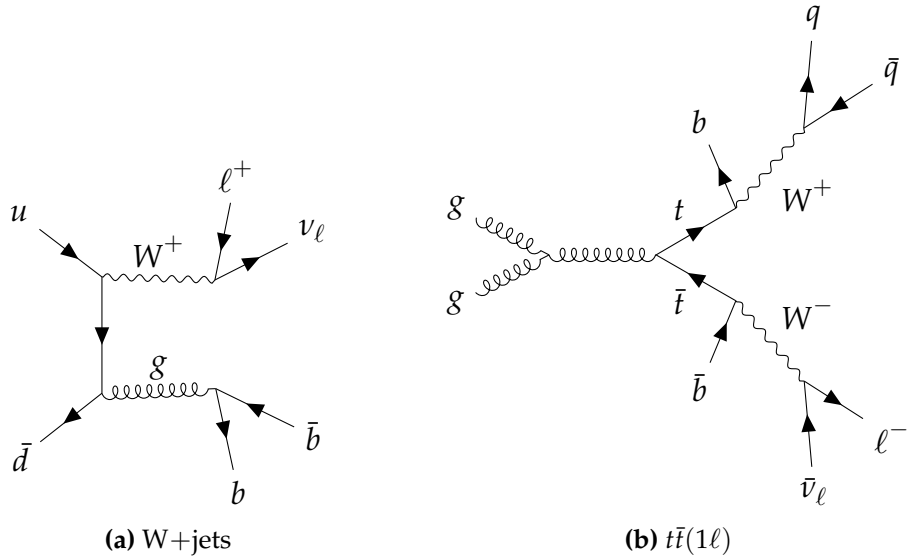


Figure 5.9.: Examples of (a) W +jets, and (b) semileptonic $t\bar{t}$ that contribute to the fake lepton background.

5.4. Fake lepton background

Another type of reducible background, the fake (or non-prompt) lepton background, is also estimated using observed events. Processes which are expected to contain only one prompt electron or muon in the final state may pass the signal region selection as described in Sec. 4.2 by a jet-induced faking of a second lepton. Namely, processes such as W +jets, semileptonic decays of $t\bar{t}$ and tW associated production, and leptonic single top decays, a few of which are shown in Figure 5.9, comprise the fake lepton background processes.

The data-driven technique used to estimate the relative contribution of fake lepton backgrounds in the signal regions is based on the measurement of the fake rate. This rate is obtained from a sample in data which is enriched in QCD multijet events. Very loose working points for an electron object and muon object are defined; these are called “fake-able objects” (“FO”) and their definitions are found under the heading “FO WP” in Tables 3.3 and 3.1 for electrons and muons respectively.

The method has two main steps,

1. **Measurement:** in a QCD enriched sample in data, measure the probability of a “FO” to pass “Tight” lepton selection: the “fake rate”
2. **Application:** in a sample consisting of one “Tight” lepton and one “FO” that fails “Tight” selection, use the fake rate to estimate the background in the signal region

5.4.1. Fake rate measurement

To obtain a sample enriched in jet-induced fakes in order to perform the fake rate measurement, the following selection is applied,

- Event passes one of the following triggers:
 - HLT_Ele[12,23]_CaloIdM_TrackIdM_PFJet30
 - HLT_Ele[12,23]_CaloIdL_TrackIdL_IsoVL_PFJet30
 - HLT_Mu[8,17]_TrkIsoVVL
- there is exactly one “FO” in the event, matched to the trigger that fired
- $p_T^{\text{miss}} < 40 \text{ GeV}$
- $M_T < 35 \text{ GeV}$
- at least one jet with $p_T > 30 \text{ GeV}$ and $|\eta| < 4$
- $\Delta\phi > 2$ between the leading jet in the event and the “FO”

The cuts are chosen to suppress the W+jets contribution (i.e. the low M_T requirement), and to enhance the multi-jet QCD contribution. Even then, the level of contamination from electroweak processes (W+jets, Z+jets, t \bar{t}) in this sample ranges from 10% at low p_T to 70% at high p_T . The contamination is thus significant, particularly in the

measurement sample for muon “FO”, that a subtraction of prompt, real leptons must be done (based on expectations from simulation). The fake rate (FR) is defined as the efficiency of a “FO” to pass “Tight” requirements,

$$\text{FR}_{ij} = \left[\frac{\left(N_{\text{Tight}}^{\text{data}} - N_{\text{Tight}}^{\text{EWK}} \right)}{\left(N_{\text{FO}}^{\text{data}} - N_{\text{FO}}^{\text{EWK}} \right)} \right]_{i=\eta, j=p_T} \quad (5.7)$$

The measured fake rates are listed in Tables 5.7 and 5.8. The fake rates depend more strongly on η than on p_T as shown in Fig. 5.10 and Fig. 5.11.

	$0.0 < \eta < 0.5$	$0.5 < \eta < 1.0$	$1.0 < \eta < 1.5$	$1.5 < \eta < 2.0$	$2.0 < \eta < 2.5$
$10 < p_T < 15$	0.063 ± 0.008	0.088 ± 0.009	0.121 ± 0.008	0.181 ± 0.009	0.176 ± 0.012
$15 < p_T < 20$	0.085 ± 0.003	0.085 ± 0.003	0.106 ± 0.003	0.164 ± 0.004	0.153 ± 0.005
$20 < p_T < 25$	0.062 ± 0.008	0.059 ± 0.007	0.080 ± 0.009	0.131 ± 0.010	0.148 ± 0.012
$25 < p_T < 30$	0.073 ± 0.011	0.078 ± 0.078	0.090 ± 0.011	0.140 ± 0.012	0.162 ± 0.012
$p_T > 30$	0.065 ± 0.007	0.091 ± 0.008	0.089 ± 0.007	0.169 ± 0.008	0.190 ± 0.008

Table 5.7.: Electron fake rates

	$0.0 < \eta < 0.5$	$0.5 < \eta < 1.0$	$1.0 < \eta < 1.5$	$1.5 < \eta < 2.0$	$2.0 < \eta < 2.4$
$10 < p_T < 15$	0.192 ± 0.004	0.210 ± 0.004	0.235 ± 0.004	0.283 ± 0.004	0.294 ± 0.005
$15 < p_T < 20$	0.202 ± 0.001	0.214 ± 0.001	0.253 ± 0.001	0.293 ± 0.001	0.307 ± 0.002
$20 < p_T < 25$	0.187 ± 0.001	0.200 ± 0.001	0.240 ± 0.001	0.286 ± 0.001	0.307 ± 0.002
$25 < p_T < 30$	0.177 ± 0.002	0.196 ± 0.002	0.239 ± 0.002	0.279 ± 0.002	0.310 ± 0.003
$p_T > 30$	0.172 ± 0.002	0.200 ± 0.002	0.233 ± 0.002	0.279 ± 0.002	0.311 ± 0.003

Table 5.8.: Muon fake rates

5.4.2. Fake rate application

The FR does not give a direct measure for an absolute lepton fake rate; it is the probability for a fake lepton which passes loose identification criteria, to additionally pass tight identification and isolation criteria. Thus, to perform the estimate of the

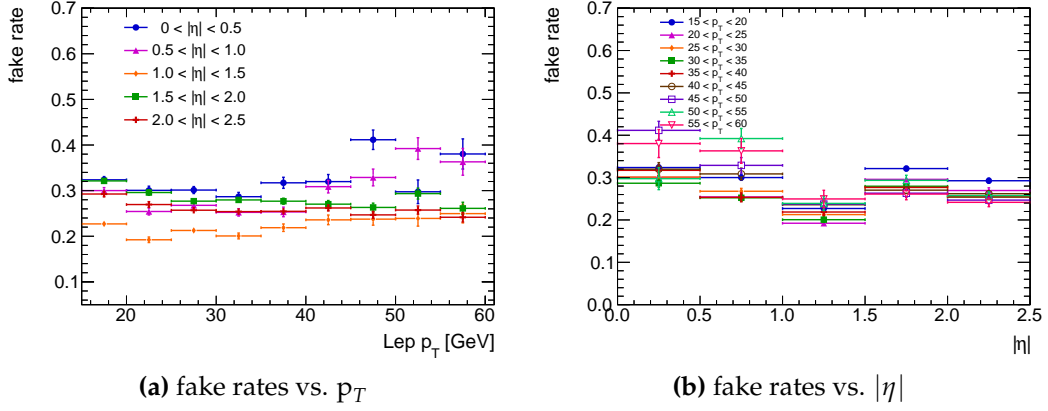


Figure 5.10.: Measured electron fake rates as a function of lepton (a) p_T and (b) $|\eta|$.

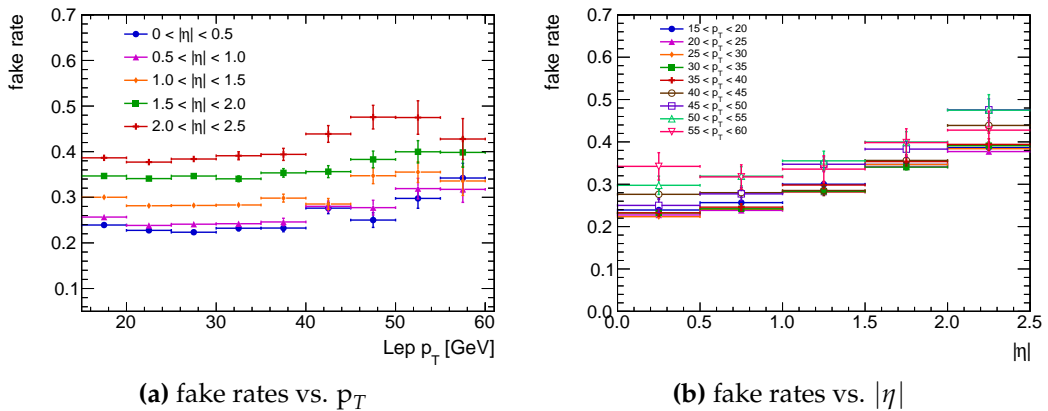


Figure 5.11.: Measured muon fake rates as a function of lepton (a) p_T and (b) $|\eta|$.

fake lepton background, an application sample of “Tight”+“FO” pairs are obtained by requiring the signal selection with the only modification being that instead of two “Tight” leptons, one “Tight” lepton and one “FO” that fails “Tight” selection is required. Each pair is then assigned a weight, $FR/(1 - FR)$, corresponding to a likelihood that the “FO” in the pair will be promoted to a “Tight” lepton, and the sum of these weighted pairs give a prediction for the background yield and distributions. In principle, a single event can contribute multiple “Tight”+“FO” pairs to the application sample, but in practice there is rarely more than one pair from an event.

Dileptonic processes can contaminate the application sample and needs to be subtracted off. MC expectations are used to perform the subtraction; about 95% of this contamination comes from dileptonic $t\bar{t}$ events.

5.4.3. Fake rate closure test

As a way to validate the estimation procedure, a closure test is performed in a fakes enriched region. The events in this region are required to pass the same selection as for the signal region, with the modified requirement that the selected leptons must have the same sign. Along with guaranteeing a region enriched in fake leptons, this validation region is also orthogonal to the signal region. A categorization based on $M_{T2}^{\ell\ell} > 110 \text{ GeV}$ is not performed because too few events pass the high $M_{T2}^{\ell\ell}$ requirement, to make a meaningful test. Good agreement between the data and the combination of simulation and data-driven fake lepton prediction is observed in the p_T^{miss} distribution, as shown in Figure 5.12. The degree in which the observed and predicted yields disagree is included in the normalization uncertainty on the fakes background prediction in the signal regions.

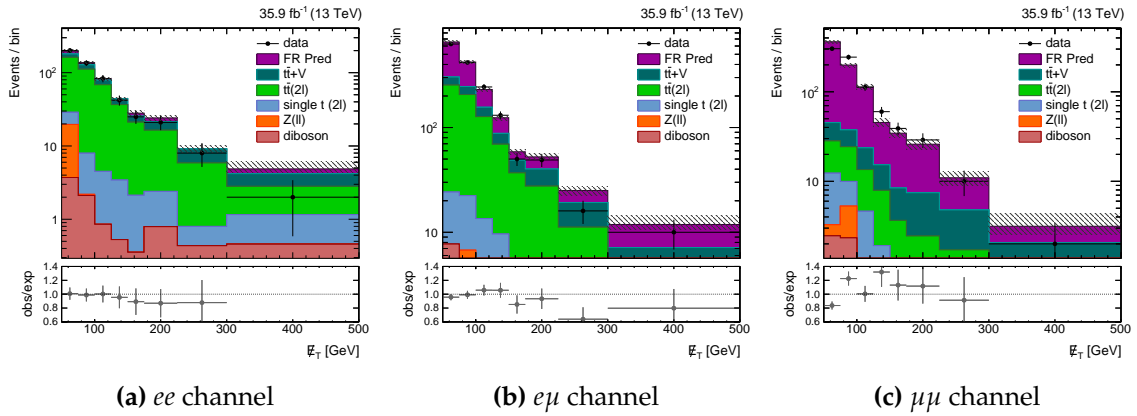


Figure 5.12.: The p_T^{miss} distributions in the fake rate method validation region. All expected backgrounds are estimated using simulation, except for the fake lepton contribution, denoted “FR Pred” which is estimated via the fake rate method.

Chapter 6.

Analysis

6.1. Search strategy

The strategy employed in this search is to define regions targeting a high signal acceptance, called signal regions (SRs). As described in Sec. 4.2, events passing the outlined selection criteria are also categorized according to whether the leptons in the dilepton pair are same or opposite flavor. Additionally, events are divided according to the whether the $M_{T2}^{\ell\ell}$ quantity is greater or less than 110 GeV. Thus, events are split into the following four SRs: high $M_{T2}^{\ell\ell}$ -SF, high $M_{T2}^{\ell\ell}$ -OF, low $M_{T2}^{\ell\ell}$ -SF, and low $M_{T2}^{\ell\ell}$ -OF. The high $M_{T2}^{\ell\ell}$ categories are classified as high signal purity regions, whereas the low $M_{T2}^{\ell\ell}$ categories are dominated by SM $t\bar{t}(2\ell)$ background and thus denoted as low signal purity regions. A potential signal observation would manifest as an excess over the expected p_T^{miss} from SM background processes, thus the signal extraction strategy is to fit the p_T^{miss} distribution in the four SRs simultaneously. This approach exploits the kinematic differences between the p_T^{miss} shapes of the $t\bar{t}+\chi\bar{\chi}$ signals described in Chap. 4 and the p_T^{miss} shapes of SM backgrounds detailed in Chap. 5. The fitting procedure and statistical method is described in Sec.(results/stats chapter).

6.2. Data to simulation corrections

Various corrections are applied to the simulation to account for mismodeling of distributions in the MC simulation, or to take into account the difference between efficiencies measured in the data compared to those measured in the simulation. The corrections are listed and described below.

6.2.1. Trigger efficiency

6.2.2. PU reweighting

The simulation does not predict the PU distribution as observed in the data, so in order to alleviate this discrepancy, the simulation is re-weighted to the estimated PU distribution in data. The re-weighting is derived from the measured instantaneous luminosity of the bunch crossings during the 2016 pp collision data-taking period and the estimated total inelastic cross section. The cross section estimate for 2016 data-taking is 69.2 mb for minimum bias events, with an uncertainty of 4.6%. The ratio of normalized distributions of the number of PU interactions in data and $t\bar{t}(2\ell)$ simulation is used to extract the scale factors that are applied to the simulation on an event-by-event basis. The PU profiles in data and simulation are shown in Figure 6.1, where the simulation is also shown with the minimum bias cross section varied by $\pm 4.6\%$ in Figure 6.1b. The effect of the PU re-weighting can be seen in Figure 6.2, where the distribution of the number of reconstructed primary vertices (PV) is shown before and after the re-weighting.

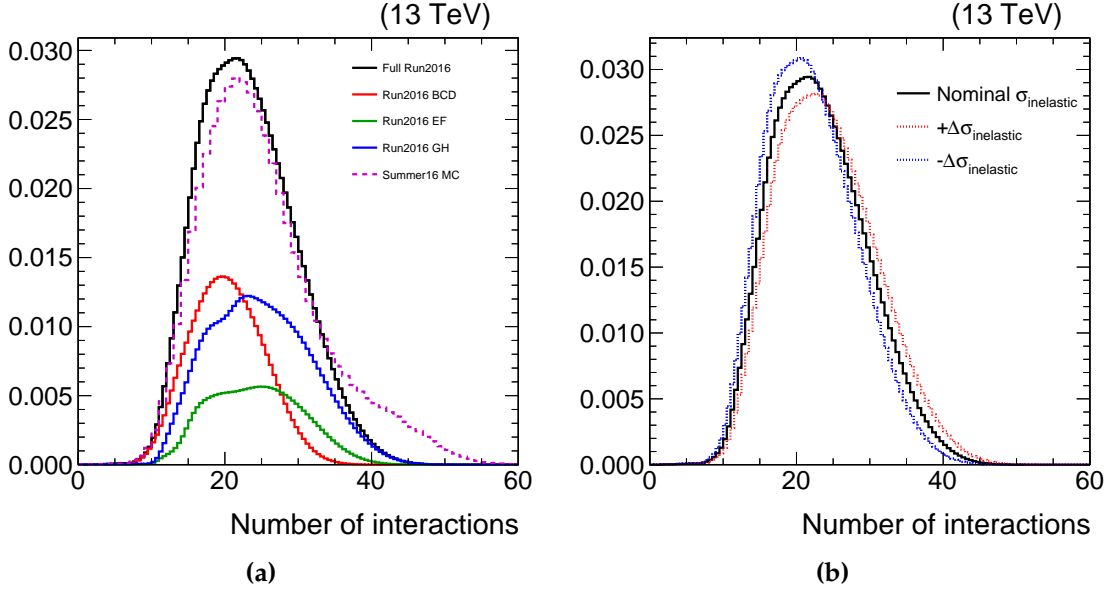


Figure 6.1.: (a) Pileup distributions in data and MC. Also shown are the pileup profiles in a few run ranges scaled to the relative contribution to the total integrated luminosity.(b) The pileup distributions from varying the total inelastic cross section by $\pm 4.6\%$.

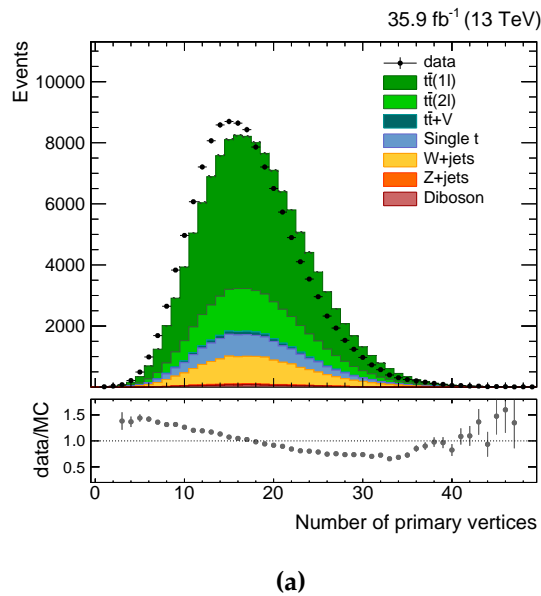


Figure 6.2.: N_{PV} distributions in data and MC pre and post PU re-weighting in a region dominated by semileptonic $t\bar{t}$ events. The MC is normalized to the observed yield.

6.2.3. Top p_T re-weighting

The generated top quark p_T in $t\bar{t}$ simulation appears to disagree with the distribution observed in data. The discrepancy arises due to the harder p_T in the simulation as compared to data, thus a correction based on a comparison of the top p_T spectrum between data and the predicted distribution at NLO accuracy from POWHEG v2 interfaced with Pythia v8.2 is used as, developed in [51]. For each top in a $t\bar{t}$ MC event, a scale factor is computed according to,

$$SF(p_T) = e^{0.0615 - 0.0005 \cdot p_T}, \quad (6.1)$$

where the exponential function describes the fit to the ratio of data to POWHEG +Pythia simulation for dileptonic and semileptonic $t\bar{t}$ events. The p_T in Eq. 6.1 is taken at the matrix element level. Subsequently, a weight is applied on an event-by-event basis where the weight is given by the geometric mean of the scale factors,

$$w = \sqrt{SF(p_{T_t}) \cdot SF(p_{T_{\bar{t}}})}. \quad (6.2)$$

The effect of the re-weighting is seen in Figure 6.3 for dilepton signal region events with $M_{T2}^{\ell\ell} < 110$ GeV and $M_{T2}^{\ell\ell} > 110$ GeV. The correction tends to grow with increasing p_T^{miss} , since this observable is correlated with top p_T .

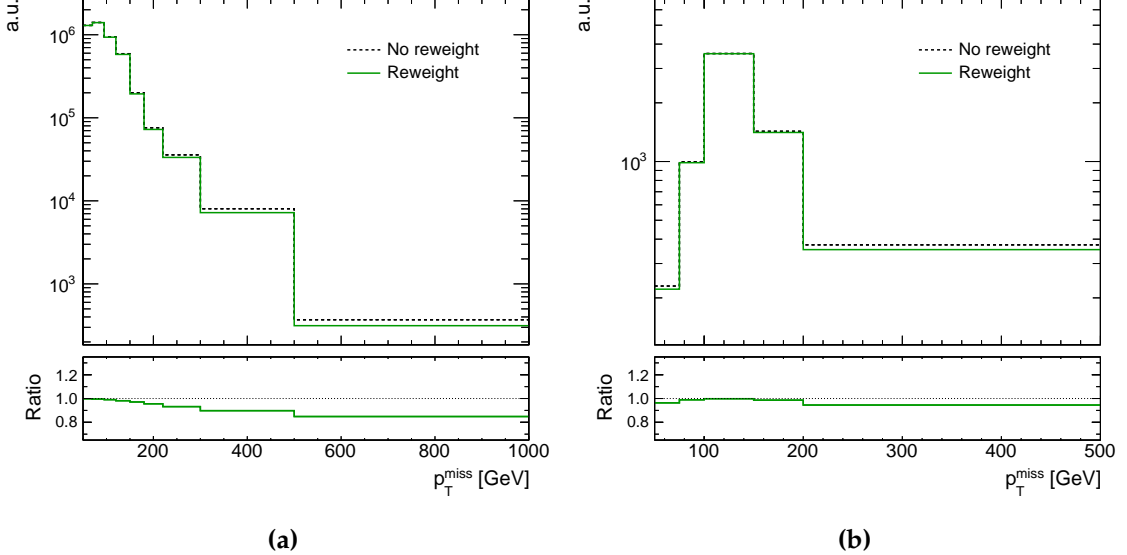


Figure 6.3.: Effect of the top p_T reweighting on the expected $t\bar{t}$ background p_T^{miss} shape for (a) $M_{T2}^{\ell\ell} < 110 \text{ GeV}$ and (b) $M_{T2}^{\ell\ell} > 110 \text{ GeV}$ events.

6.2.4. b-tagging efficiency

The efficiency to tag jets originating from b-quark hadronization is dependent on the working point of the b-tagging algorithm used (in this case the CSV algorithm as defined in Sec. 3.2.1), and the jet kinematics in the signal region of interest. Hence, the performance is characterized based on the probabilities to correctly tag a b jet (ϵ_b), to misidentify the hadronization of a c-quark as a b jet (ϵ_c), and to misidentify light flavor or gluon initiated jets as b jets ($\epsilon_{uds g}$). Each efficiency is defined by,

$$\epsilon_f(i, j) = \frac{N_f^{\text{b-tagged}}(i, j)}{N_f^{\text{Total}}(i, j)}, f = b, c, uds g \quad (6.3)$$

where the efficiency is defined in jet p_T bin i and η bin j , and N_f^{Total} and $N_f^{\text{b-tagged}}$ are the total number of jets and the number of b-tagged jets of flavor f . The efficiency

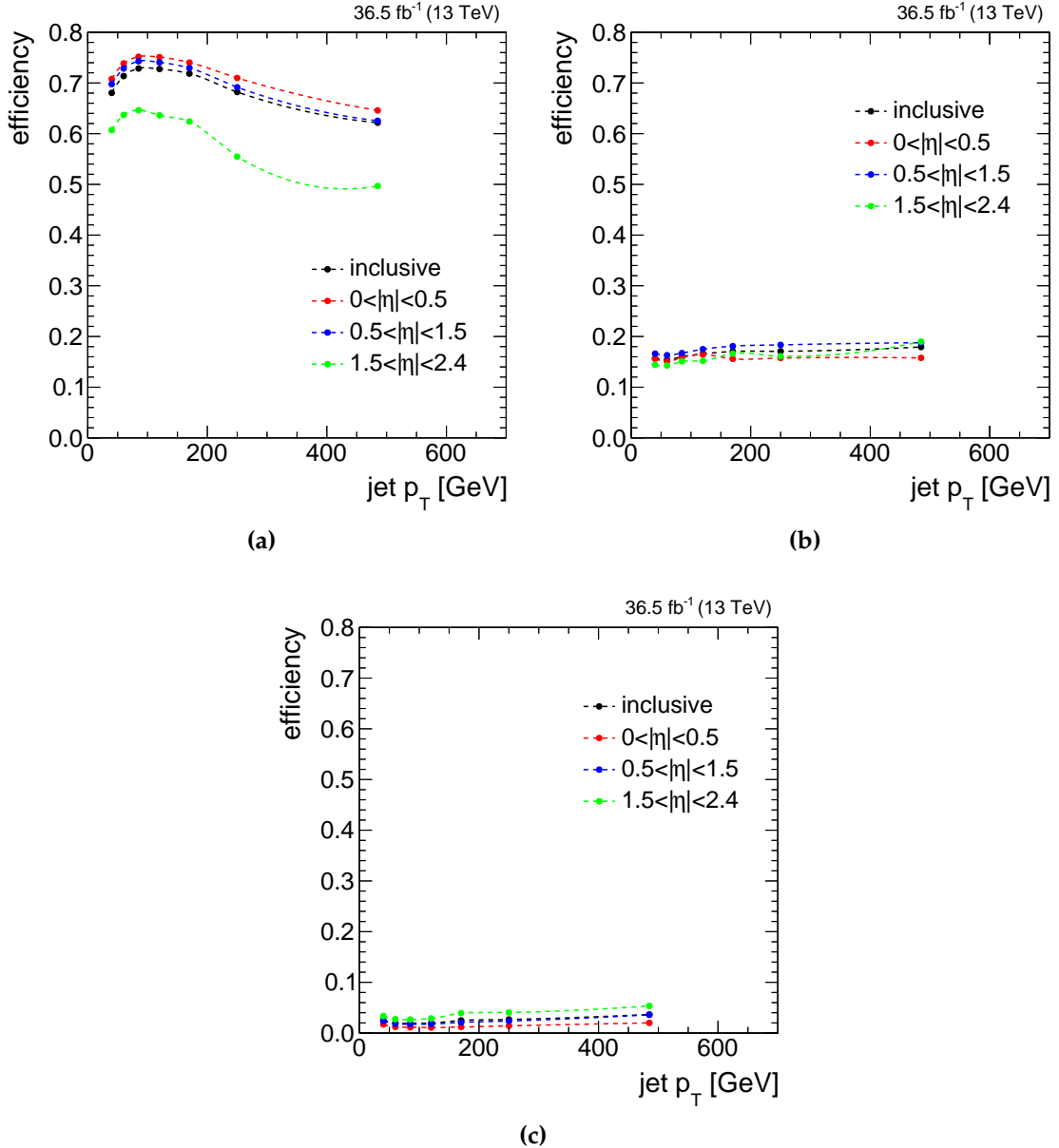


Figure 6.4: The efficiency measured as a function of jet p_T and various η bins for (a) correctly tagging b jets, (b) misidentifying c jets, (c) and misidentifying light flavor or gluon jets.

is measured in a simulation sample of dilepton $t\bar{t}$ and shown in Figure 6.4 for each jet flavor as a function of p_T and η .

The CSV algorithm has three working points which correspond to different values of $\epsilon_{uds g}$ as measured in data. They are defined as loose ($\epsilon_{uds g} = 10\%$), medium

($\epsilon_{uds_g} = 1\%$), and tight ($\epsilon_{uds_g} = 0.1\%$). In the following analysis, the medium working point is used and corresponds to a b-tagging efficiency of $\epsilon_b = 69\%$, and an c-jet mistag efficiency of $\epsilon_c = 35\%$ in data. The corrections are applied to the simulation based on the ratio of efficiencies measured in the data and simulation, in order to cover any differences in efficiency with respect to the performance in data.

6.3. Discriminating observables

p_T^{miss} is the detector observable which provides the strongest discrimination between the $t\bar{t} + \chi\bar{\chi}$ signal and the dominant SM dileptonic $t\bar{t}$ background. In addition to the main observable used for the signal extraction, multiple other observables are scrutinized as a means to check the background modeling and ascertain if discrepancies between the data and the simulation exist in the signal region. These can be seen in the same flavor and opposite flavor channels, respectively, in Figure 6.5 and Figure 6.6. The observables include the multiplicity of jets (N_{jets}), and that of b-tagged jets ($N_{\text{b-jets}}$), as well as kinematic distributions for the highest p_T (leading) lepton and jet in the event. The 4-vectors of the two leptons in the event are summed to obtain the p_T and mass of the dilepton system, $p_T^{\ell\ell}$ and $m_{\ell\ell}$. The azimuthal separation between the dilepton system and the \vec{p}_T^{miss} , $\Delta\phi(\ell\ell, \vec{p}_T^{\text{miss}})$, is also shown, along with the uncategorized p_T^{miss} spectrum.

The $M_{\text{T2}}^{\ell\ell}$ distribution used to categorize events into a low ($M_{\text{T2}}^{\ell\ell} < 110 \text{ GeV}$) and high ($M_{\text{T2}}^{\ell\ell} > 110 \text{ GeV}$) signal purity category is shown in Figure 6.7. The subsequent p_T^{miss} spectra in the low and high purity signal regions are shown in Figure 6.8 and Figure 6.9, respectively.

6.4. Systematic uncertainties

The signal and background p_T^{miss} templates derived from simulation are subject to effects incurred from experimental and theoretical sources of uncertainty. The p_T^{miss} distributions are parametrized in order to allow for constrained shape and normalization variations as a cause of the systematic uncertainties, referred to throughout as “systematics”. Each systematic is represented by a nuisance parameter, θ , with a probability density function, pdf , denoted as $\rho(\theta)$, that contains the central value of the nuisance, $\tilde{\theta}$, and other parameters that describe the overall shape of the pdf , such as its width.

Uncertainties which affect the normalization of the signal and background processes are modeled using nuisance parameters with log-normal probability densities. The log-normal pdf follows the form [52],

$$\rho(\theta) = \frac{1}{\sqrt{2\pi} \ln \kappa} \exp \left(-\frac{(\ln(\theta/\tilde{\theta}))^2}{2(\ln \kappa)^2} \right) \frac{1}{\theta}. \quad (6.4)$$

where the width of the log-normal distribution is characterized by κ , and $\tilde{\theta}$ represents the best estimate of the nuisance θ . In the limit of small uncertain (ϵ), the width of a Gaussian pdf is given by $\sigma = \epsilon$, which equates directly to the log-normal width via a Taylor expansion for $\kappa = e^\epsilon$, such that $\kappa = 1 + \epsilon$. The log-normal pdf is useful in the case of large uncertainties as the distribution has a longer tail in comparison with a Gaussian pdf , and avoids the problem of negative parameter values obtained from a Gaussian probability density, since $\rho(\theta) \rightarrow 0$ for $\theta = 0$.

A number of uncertainties influence the overall shape of the signal and background p_T^{miss} templates along with the normalization. Systematics of this type are implemented

using a general technique known as “vertical morphing” [53]. A change in a particular type of uncertainty (such as an energy scale) can cause a distortion in both the shape and overall normalization of the efficiency as a function of the observable (p_T^{miss}) bin. Raising and lowering a particular parameter to its corresponding values at one standard deviation will cause the bin efficiencies, denoted as ϵ_{ij} for source i in observable bin j , to also shift, thus resulting in three measures of the bin efficiency shape, referred to as ϵ_{ij}^+ , ϵ_{ij}^0 , and ϵ_{ij}^- . In order to transform the three shape measures into a continuous estimate as a function of the parameter value, a morphing parameter, represented by f and nominally equal to 0 with a unitary uncertainty, is used. A quadratic interpolation is used for values where $|f| < 1$, to express the efficiency in a bin as a function of the morphing parameter such that,

$$\epsilon_{ij} = \frac{f(f-1)}{2}\epsilon_{ij}^- - (f-1)(f+1)\epsilon_{ij}^0 + \frac{f(f+1)}{2}\epsilon_{ij}^+. \quad (6.5)$$

The form of Eq. 6.5 guarantees that the value of the expression is ϵ_{ij}^\pm for $f = \pm 1$.

6.4.1. Sources of systematic uncertainty

The following sources of uncertainty affect the normalization of the signal and background processes:

- **Pileup modeling:** As described in Sec. 6.2.2, the total inelastic cross section used to calculate the data pileup distributions is varied by $\pm 4.6\%$, in order to account for systematic uncertainties due to pileup modeling. Normalization differences in the range of 0.3 – 11% result from reweighting the simulation accordingly.

- **Integrated luminosity:** The overall uncertainty of the measurement of the integrated luminosity delivered to the CMS Experiment during the 2016 LHC proton-proton run at $\sqrt{s} = 13$ TeV is estimated to be 2.5% [54].
- **Lepton reconstruction and selection:** The uncertainty on lepton reconstruction and selection efficiency is associated with the efficiency measurement with samples of Z bosons decaying to dielectrons or dimuons [55]. The p_T - and η -dependent scale factors are varied within their uncertainties which amounts to $\approx 2\%$ per lepton.
- **Lepton trigger:** The uncertainty on lepton triggering efficiency is associated with the efficiency measurement with samples of Z bosons decaying to dielectrons or dimuons. The corresponding uncertainty ranges from 1% to 2%.
- **b-tagging efficiency:** The b-tagging efficiency and mis-tag rate and the respective uncertainties are measured on independent control samples. Uncertainties from gluon splitting, the b quark fragmentation function, and the selections used to define the control samples are propagated to the efficiency scale factors [56]. The uncertainties on the mis-tag rate range from 0.1 – 4%, while the b-tagging efficiency uncertainties range from 0.1 – 2%.
- **Single top and diboson normalization:** In practice, the expected yields for background processes are either scaled to data or to theory predictions with the best available accuracy. The uncertainties on the cross section predictions are taken into account in the PDF as well as the renormalization and factorization scale uncertainties. However, in the single top and diboson simulation samples used, the aforementioned variations are not available, so a conservative uncertainty of 20% and 10% is assigned respectively to the normalizations, and these uncertainties are treated independently of each other.

- **Drell-Yan background uncertainty:** The uncertainties incurred from the data-driven estimate of the Drell-Yan background normalization are dominated by the statistical uncertainties on N_{in} and R_{MC}^{1b} , quantities used to extrapolate yields from a region near the Z boson mass to regions away from it, as described in Sec. 5.3. The uncertainties are 11% and 6% for the ee and $\mu\mu$ channels and only applies to the DY background.
- **Fake lepton background uncertainty:** The sources of uncertainty in the fake lepton background stem from the uncertainty in the measured fake rate, and from the statistical uncertainty of the single-lepton control sample to which the rate is applied, as described in Sec. 5.4. The uncertainties are 78% (ee), 70% ($e\mu$), 74% ($\mu\mu$) in the high signal purity category and 47% (ee), 12% ($e\mu$), and 20% ($\mu\mu$) in the low signal purity category, and are dominated by the statistical uncertainty associated with the single-lepton control sample. Since the fake lepton background is small, these relatively large uncertainties do not significantly degrade the sensitivity of the search.

The systematics affecting the overall p_T^{miss} shape and normalization listed below in order of decreasing dominance on the final result:

- **Jet energy scale (JES):** Reconstructed jet four-momenta in the simulation are simultaneously varied according to the uncertainty on the JES. JES uncertainties are coherently propagated to all observables impacted, including jet kinematics and multiplicity, p_T^{miss} , and $M_{T2}^{\ell\ell}$. Uncertainty effects due to the jet energy resolution (JER) were found to be negligible.
- **Fake p_T^{miss} uncertainty:** For the high signal purity ($M_{T2}^{\ell\ell} > 110 \text{ GeV}$) category, an uncertainty is assigned to the background p_T^{miss} shapes derived from simulation to account for potential mismodeling of the rate of events with large fake p_T^{miss} in simulation. This uncertainty is derived using Z bosons decaying to dielectrons

and dimuons, as a function of hadronic recoil (i.e. p_T^{miss} with the two leptons removed), and also passing $M_{T2}^{\ell\ell} > 110 \text{ GeV}$. The difference between the simulation and data after the subtraction of non-Drell-Yan events as expected from simulation, is taken as the uncertainty and added/subtracted to the nominal recoil distribution to obtain the one standard deviation variations. A second-order polynomial is fit to the fake p_T^{miss} uncertainty scale factor distributions in an effort to smoothen the uncertainty as a function of the recoil, as shown in Figure 6.10.

- **Factorization and renormalization scales:** Uncertainties due to the renormalization scale μ_R and the factorization scale μ_F employed in the simulation matrix-element generator are modeled by halving or doubling each of the scales independently [57], and propagating the changes to the p_T^{miss} templates. This is accommodated via weights obtained directly from the generator information in the MC simulation where available. The uncertainty is considered to be uncorrelated among the different background processes.
- **Top quark p_T reweighting:** The top quark p_T spectrum as measured in differential top quark pair production is observed to be softer than that of simulation, as discussed in Sec. 6.2.3. In order to cover this effect, the scale factors derived in previous CMS measurements [51] are applied to the $t\bar{t}$ simulation by default. The uncertainty is estimated from a comparison of the top p_T spectrum obtained without the reweighting applied.
- **Parton distribution function (PDF):** Uncertainties due to the choice of PDFs used to simulate the hard scatter process are estimated by reweighting the simulation samples with the ensemble of 100 PDF replicas [58] provided by NNPDF3.0 [59].

6.5. Statistical analysis

The methods by which the statistical analysis is performed are outlined in the following section. A brief description of the model parameter estimation and statistical model inference methods are outlined. Finally, the means by which the signal is extracted is described. An in-depth discussion of statistical methods can be found in

6.5.1. Maximum likelihood

The maximum likelihood estimates the best value of the parameters (i.e. signal strength and background shape and normalizations), for which the observed data has the highest probability of estimating the true parameter value according to the hypothesis model. Following the discussion in [], supposing in a set of N events, we observe a set of measured quanties, \bar{x} . In the space of these observables we can define a set of bins, n_{bin} , and it is assumed that the number of events n_i in each bin i are Poisson-distributed such that,

$$\mathcal{P}(n_i | \lambda_i) = \frac{\lambda_i^{n_i} e^{-\lambda_i}}{n_i!}, \quad (6.6)$$

where λ_i is the number of expected events in the bin containing contributions from both signal and background processes such that $\lambda = \mu s + b$. The number of signal (background) events is denoted by s (b), and subsequently the parameter μ represents the signal strength scaling, where $\mu = 0$ corresponds to the background-only hypothesis, and $\mu = 1$ is the nominal signal hypothesis. The likelihood function is then simply the product of Poisson probabilities for all bins,

$$\mathcal{L} = \prod_{j=1}^N \frac{(\mu s_j + b_j)^{n_j}}{n_j!} e^{-(\mu s_j + b_j)}, \quad (6.7)$$

where the mean number of entries in the j th bin from signal and background are

$$s_j = s_{\text{tot}} \int_{\text{bin } j} f_s(x; \theta_s) dx, \quad (6.8)$$

$$b_j = b_{\text{tot}} \int_{\text{bin } j} f_b(x; \theta_b) dx. \quad (6.9)$$

The functions $f_s(x; \theta_s)$ and $f_b(x; \theta_b)$ are the *pdfs* of the variable x for signal and background events and θ_s and θ_b are the nuisance parameters described in Sec. 6.4, which characterize the shape of the *pdfs*. The integrals in Eq. 6.8 and Eq. 6.9 represent the probabilities for an event to be found in bin j , and s_{tot} and b_{tot} denote the total mean numbers of signal and background events, respectively. It is then clear that the likelihood in Eq. 6.7 is a function of the nuisance parameters, $\mathcal{L}(\theta)$, and the values of θ which maximize this quantity are said to fit the observation best.

6.5.2. Hypothesis testing

In order to determine whether to accept or reject a model depending on the outcome of a measurement, a frequentist test of a hypothesis is performed. In this case, we test the hypothesized value of the signal strength, μ , which is interpreted as the ratio of the measured cross section, σ , to the predicted value from the theory model, σ_{TH} , such

that $\mu = \frac{\sigma}{\sigma_{\text{TH}}}$. Hence, a null value of μ corresponds to an observation compatible with the SM background-only hypothesis, whereas if the observation is compatible with signal events as predicted by the model cross section, then $\mu = 1$.

Quantifying the level of agreement between the observation and a tested hypothesis is done via a test statistic $q(\mu)$, which is defined as the ratio of maximum likelihoods,

$$q(\mu) = \frac{\mathcal{L}(\mathcal{D} | \mu, \hat{\theta}(\mu))}{\mathcal{L}(\mathcal{D} | \hat{\mu}, \hat{\theta})} \quad (6.10)$$

where the $\hat{\theta}(\mu)$ indicates the values of the nuisance parameters θ profiled, which maximize \mathcal{L} for a fixed value of μ , the dataset \mathcal{D} , and global observables. The denominator of the so-called *profile likelihood ratio* defined by Eq. 6.10 is the value of \mathcal{L} when evaluated with the maximum likelihood estimators (MLEs) $\hat{\mu}$ and $\hat{\theta}$. The MLEs and profiled nuisance parameters can analogously minimize the quantity $-2 \ln \mathcal{L}$, so it is common to write the definition of the test statistic as,

$$q(\mu) = -2 \ln \frac{\mathcal{L}(\mu, \hat{\theta}(\mu))}{\mathcal{L}(\hat{\mu}, \hat{\theta})}, \mu' \leq \mu. \quad (6.11)$$

For the purposes of setting limits on theoretical parameters (i.e. determining the values of the parameters that are allowed or excluded given the available data) the test statistic $q(\mu)$ is used to discriminate between the hypothesis of the signal being produced at a rate μ from an alternative hypothesis of signal events being produced at a lesser rate $\mu' < \mu$. Thus, it is a test statistic for a one-sided alternative or moreover provides a one-sided upper limit. If the experiment were to be repeated multiple times, $q(\mu)$ would take on different values, thus the test statistic itself has a particular

probability density function, $f(q(\mu) \mid H)$, dependent on the particular hypothesis, H , being tested. Then the probability that a given $q(\mu)_{\text{obs}}$ is an equal or more 'extreme' outcome than observed, assuming H is,

$$p = \int_{q(\mu)_{\text{obs}}}^{\infty} f(q(\mu) \mid H) dq(\mu). \quad (6.12)$$

The quantity in Eq. 6.12 and visualized in Fig. 6.11, known as the *p-value*, indicates a worse agreement with the corresponding H for small *p*-values. In the language of discovery in high energy physics, it is customary to relate the *p*-value into a quantile of a unit Gaussian to express the significance Z , as shown in Fig. 6.11. The area of the tail starting at an upward fluctuation of Z standard deviations from the mean of the Gaussian random variable, should be equal to the *p*-value. The transformation is defined formally as,

$$Z = \Phi^{-1}(1 - p) \quad (6.13)$$

where Φ^{-1} is the inverse of the cumulative distribution of the signle sided standard Gaussian. A 5σ significance is the common requirement to claim a discovery, which is analogous to a *p*-value of 2.87×10^{-7} .

In the absence of a discovery, i.e. the *p*-value determined from the observed data cannot exclude the background-only hypothesis, then the upper limit on the signal strength parameter, μ , is established. The one-sided modified frequentist confidence level (CL_s) upper limit on μ is defined as,

$$\text{CL}_s = \frac{p_\mu}{1 - p_0} \quad (6.14)$$

where p_0 is the p -value determined given that the hypothesis under test is that of the SM background-only. In practice, results are calculated at 95% CL_s which is defined as the μ that produces CL_s = 0.05.

6.5.3. Signal extraction

An excess of events in the dataset with respect to the expected SM predictions would indicate the presence of the t̄t + χ̄χ signal process. In order to extract the results, a binned maximum likelihood fit is performed simultaneously on the p_T^{miss} distributions in the SRs as defined in more detail in Sec. 6.3. A single strength parameter is used to scale the signal across all the SRs. The sources of systematic uncertainties are represented by nuisance parameters in the fit, as described in greater detail in Sec. 6.4.

The likelihood ratio defined by Eq. 6.11 is used to assess the fit for the saturated model, and provides a generalization of the χ^2 goodness-of-fit test as per [60]. The fitted background-only p_T^{miss} distributions are shown in Figure 6.12 and Figure 6.13. The corresponding observed data yield and post-fit SM background expected yields are presented for the high and low purity categories in Table 6.1 and 6.2, respectively. The p -value of 0.06, as defined by Eq. 6.12, is determined from the distribution of the likelihood ratio obtained from pseudodata generated from the fitted simulation yields. No significant excess in the SRs is observed.

Table 6.1.: Background-only post-fit event yields passing selection in the $M_{T2}^{\ell\ell} > 110$ GeV (high signal purity) category. The expected (pre-fit) yield is also shown for a pseudoscalar $m_a = 100$ GeV, $m_\chi = 1$ GeV signal. The uncertainties include contributions from both systematic and statistical sources.

$M_{T2}^{\ell\ell} > 110$ GeV		
	$ee + \mu\mu$	$e\mu$
Diboson	3.83 ± 0.51	1.42 ± 0.58
Drell-Yan	68.51 ± 9.88	0.85 ± 0.51
Single t (2ℓ)	7.34 ± 1.51	8.59 ± 1.88
$t\bar{t} + V$	7.83 ± 1.12	5.87 ± 0.95
$t\bar{t}(2\ell)$	77.67 ± 5.60	104.91 ± 7.49
Fakes	0.72 ± 0.92	4.14 ± 2.82
SM Expected	165.90 ± 10.26	125.77 ± 8.96
Observed	156	128
$m_a = 100, m_\chi = 1$	5.18 ± 0.089	5.82 ± 0.094

Table 6.2.: Background-only post-fit event yields passing selection in the $M_{T2}^{\ell\ell} < 110$ GeV (low signal purity) category. The expected (pre-fit) yield is also shown for a pseudoscalar $m_a = 100$ GeV, $m_\chi = 1$ GeV signal. The uncertainties include contributions from both systematic and statistical sources.

$M_{T2}^{\ell\ell} < 110$ GeV		
	$ee + \mu\mu$	$e\mu$
Diboson	178.05 ± 10.85	148.68 ± 9.19
Drell-Yan	2633.18 ± 279.35	267.71 ± 29.52
Single t (2ℓ)	3356.63 ± 553.19	3946.44 ± 648.20
$t\bar{t} + V$	232.94 ± 31.56	256.39 ± 33.33
$t\bar{t}(2\ell)$	79534.15 ± 702.17	94338.27 ± 805.11
Fakes	689.18 ± 322.88	792.42 ± 80.64
SM Expected	86624.13 ± 401.67	99749.92 ± 469.50
Observed	86619	99793
$m_a = 100, m_\chi = 1$	19.63 ± 0.17	22.70 ± 0.19

6.5.4. Post-fit diagnostics

The observed *pull* statistic in Eq. 6.15 as defined in [61], is used to assess whether the fit gives unbiased central values of the nuisance parameters and errors of correct coverage. The metric quantifies how far from the expected value, a nuisance parameter had to be “pulled” in order to find the maximum likelihood estimate. The pull is expected to follow a unit Gaussian, with a mean of 0 and unitary width.

$$\text{pull}(\theta) = \frac{\theta^{\text{fit}} - \theta^{\text{true}}}{\sigma_{\theta^{\text{fit}}}} \quad (6.15)$$

The *impact* quantity [62] is measured as a means to gauge how much the parameter of interest (POI), i.e. the signal strength parameter, depends on changes in the nuisance parameters. The impact of a nuisance parameter is defined as,

$$\text{Impact}(\theta) = \Delta\mu^\pm = \hat{\mu}_{\theta^{\text{true}} \pm \sigma_\theta} - \hat{\mu}, \quad (6.16)$$

where $\hat{\mu}_{\theta^{\text{true}} \pm \sigma_\theta}$ is defined as the maximum likelihood estimator of μ when every nuisance parameter except θ is profiled, and θ is set to its expectation value (θ^{true}) plus or minus one standard deviation. The relative importance of the various systematic uncertainties are determined according to their impact on μ , since not all nuisance parameters are of equal importance in the fitting procedure.

The pulls are computed for the nuisance parameters representing the systematic uncertainties defined in Sec. 6.4. Table 6.3 relates the nuisance name as seen in the pulls plot in Figure 6.14 to the corresponding systematic uncertainty. The table also

summarizes which process is affected, and if the uncertainty affects the shape or normalization of a process. Unless indicated under the description heading, a nuisance is treated as correlated across both same and opposite flavor, high and low $M_{\mathrm{T}2}^{\ell\ell}$ signal regions, and across the signal and all background processes. The pulls in Figure 6.14 are computed considering the background-only hypothesis (red markers) and signal-plus-background hypothesis (blue markers), where the signal under consideration is a pseudoscalar mediator with $M_a = 100 \text{ GeV}$ and $M_\chi = 1 \text{ GeV}$. None of the nuisances are pulled significantly relative to the a priori uncertainties (grey hatching). The most constrained nuisances are the jet energy scale (`CMS_scale_j`), constrained to 0.14 of the a priori value, and the renormalization/factorization scale uncertainty on the $t\bar{t}(2\ell)$ (`tt_qcdScale`), constrained to the 0.27 of the a priori value. The constraints come mainly from the high yields in the low $M_{\mathrm{T}2}^{\ell\ell}$ regions.

Name	Description	Type	Signal	$t\bar{t}(2\ell)$	Single $t(2\ell)$	$t\bar{t} + V$	Diboson	Drell-Yan	Fakes
CMS_eff_b	b-tagging efficiency	InN	✓	✓	✓	✓	✓	✓	✓
CMS_eff_e	electron reconstruction/selection efficiency	InN	✓	✓	✓	✓	✓	✓	✓
CMS_eff_m	muon reconstruction/selection efficiency	InN	✓	✓	✓	✓	✓	✓	✓
CMS_eff_mistag	b mistag rate	InN	✓	✓	✓	✓	✓	✓	✓
CMS_norm_SR	single top normalization	InN	✓	✓	✓	✓	✓	✓	✓
CMS_scale_j	jet energy scale	InN	✓	✓	✓	✓	✓	✓	✓
CMS_scale_pu	pile up	InN	✓	✓	✓	✓	✓	✓	✓
RecoilCorr	fake p_T^{miss} uncertainty (high $M_{T2}^{\ell\ell}$)	InN	✓	✓	✓	✓	✓	✓	✓
Zjets_qcdScale	factorization/renormalization uncertainty on DY shape	InN	✓	✓	✓	✓	✓	✓	✓
hi_ee_Rinout	R _{in/out} uncertainty: high $M_{T2}^{\ell\ell}, ee$ events	InN	✓	✓	✓	✓	✓	✓	✓
hi_mm_Rinout	R _{in/out} uncertainty: high $M_{T2}^{\ell\ell}, mm$ events	InN	✓	✓	✓	✓	✓	✓	✓
lo_ee_Rinout	R _{in/out} uncertainty: low $M_{T2}^{\ell\ell}, ee$ events	InN	✓	✓	✓	✓	✓	✓	✓
lo_mm_Rinout	R _{in/out} uncertainty: low $M_{T2}^{\ell\ell}, mm$ events	InN	✓	✓	✓	✓	✓	✓	✓
hi_ee_fakes	fakes uncertainty: high $M_{T2}^{\ell\ell}, ee$ events	InN	✓	✓	✓	✓	✓	✓	✓
hi_em_fakes	fakes uncertainty: high $M_{T2}^{\ell\ell}, em$ events	InN	✓	✓	✓	✓	✓	✓	✓
hi_mm_fakes	fakes uncertainty: high $M_{T2}^{\ell\ell}, mm$ events	InN	✓	✓	✓	✓	✓	✓	✓
lo_ee_fakes	fakes uncertainty: low $M_{T2}^{\ell\ell}, ee$ events	InN	✓	✓	✓	✓	✓	✓	✓
lo_em_fakes	fakes uncertainty: low $M_{T2}^{\ell\ell}, em$ events	InN	✓	✓	✓	✓	✓	✓	✓
lo_mm_fakes	fakes uncertainty: low $M_{T2}^{\ell\ell}, mm$ events	InN	✓	✓	✓	✓	✓	✓	✓
lumi_13TeV	luminosity	InN	✓	✓	✓	✓	✓	✓	✓
pdf	parton distribution function	InN	✓	✓	✓	✓	✓	✓	✓
topPt	top p_T modeling	InN	✓	✓	✓	✓	✓	✓	✓
trigeff_11	dilepton trigger efficiency	InN	✓	✓	✓	✓	✓	✓	✓
ttV_qcdScale	factorization/renormalization uncertainty on $t\bar{t} + V$	InN	✓	✓	✓	✓	✓	✓	✓
tt_qcdScale	factorization/renormalization uncertainty on $t\bar{t}(2\ell)$	InN	✓	✓	✓	✓	✓	✓	✓

Table 6.3: A summary of the naming convention for the nuisance parameters used in the fit, whether each is implemented as “lnN” (normalization uncertainty) or “shape” (shape uncertainty), and which processes each affects. Unless indicated under the description heading, a nuisance is treated as correlated across both same and opposite flavor, high and low $M_{T2}^{\ell\ell}$ signal regions, and across the signal and all background processes.

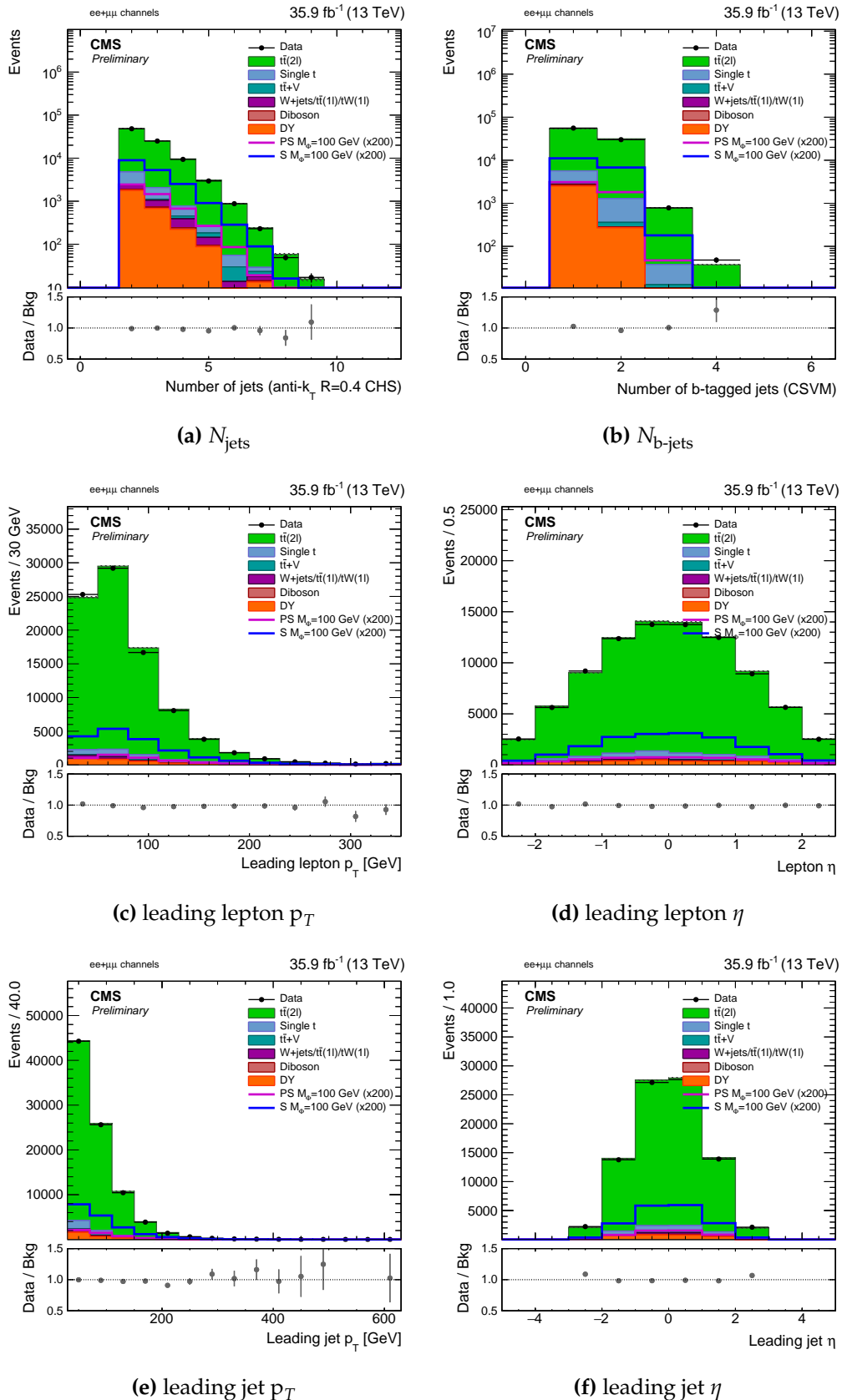


Figure 6.5.

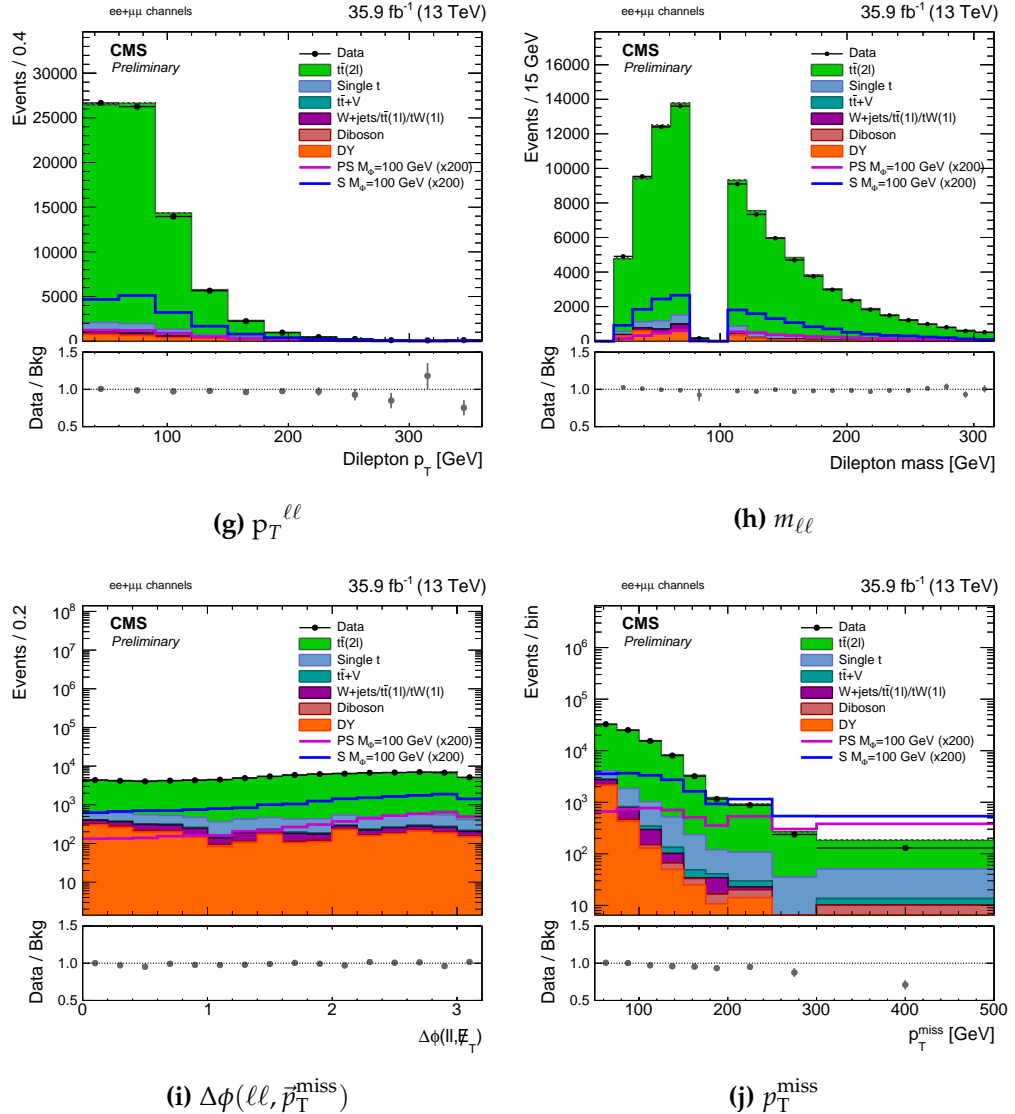


Figure 6.5.: Kinematic distributions in the same flavor ($ee + \mu\mu$) channel. Signals with a pseudoscalar (magenta) and scalar (blue) mediator with $m_\phi = 100$ GeV and $m_\chi = 1$ GeV are overlaid and scaled by a factor of 200 to illustrate the potential shape differences between the signal and background in the various distributions. The uncertainties shown in these plots on the data and background are purely statistical.

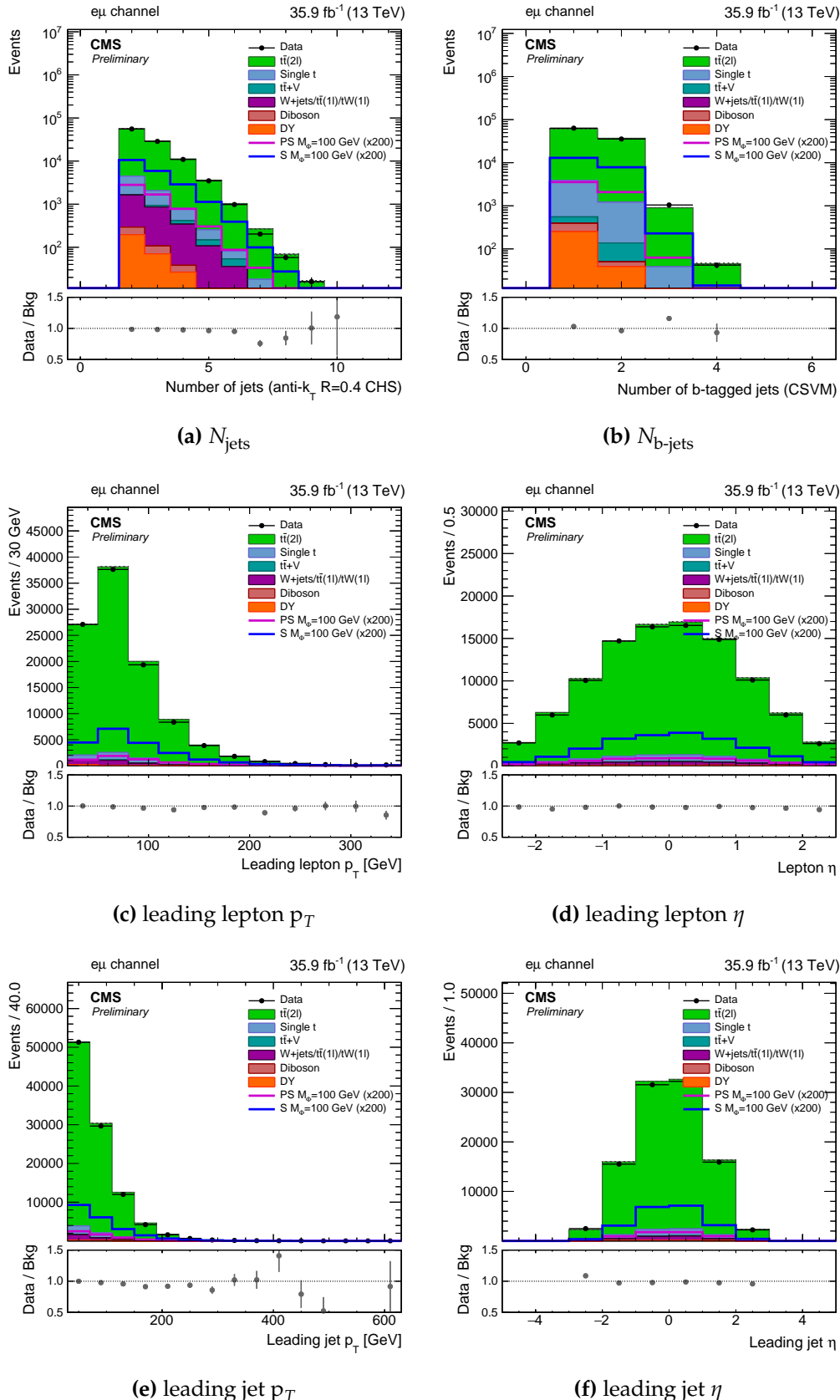


Figure 6.6.

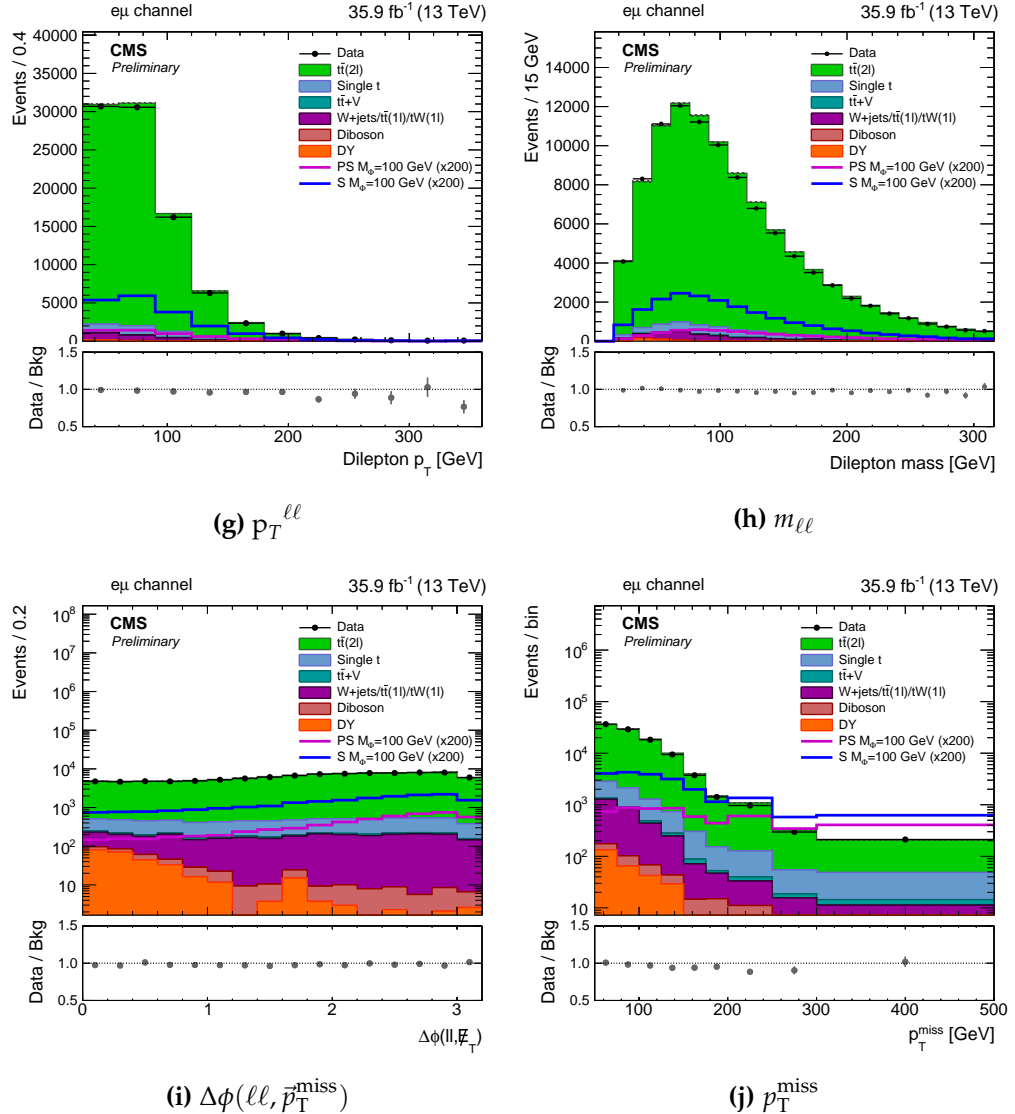


Figure 6.6: Kinematic distributions in the same flavor ($e\mu$) channel. Signals with a pseudoscalar (magenta) and scalar (blue) mediator with $m_\phi = 100$ GeV and $m_\chi = 1$ GeV are overlaid and scaled by a factor of 200 to illustrate the potential shape differences between the signal and background in the various distributions. The uncertainties shown in these plots on the data and background are purely statistical.

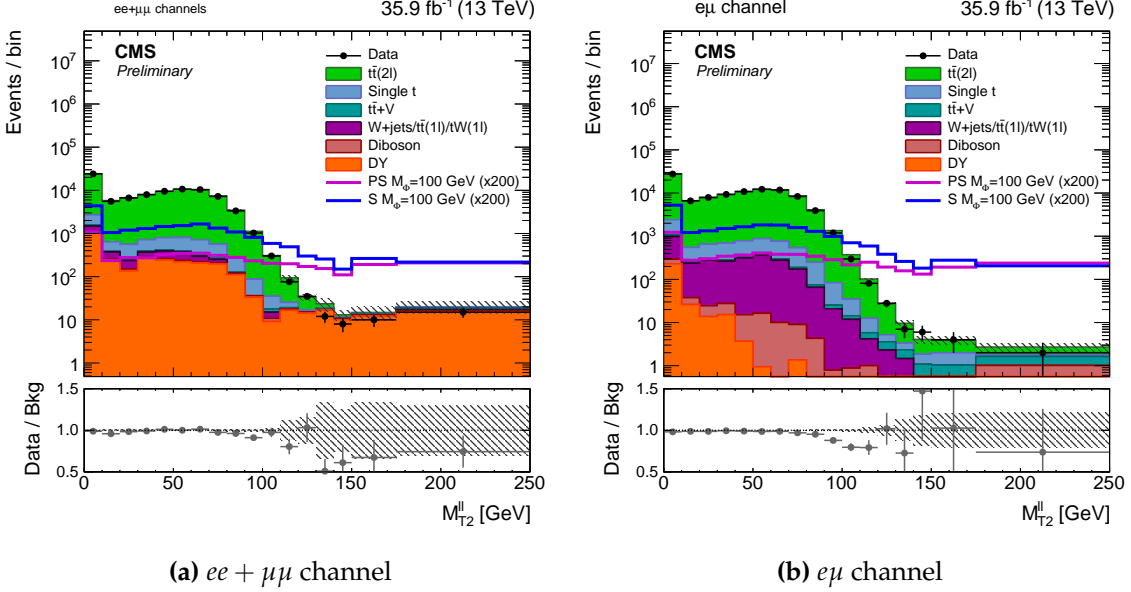


Figure 6.7.: The M_{T2}^{ll} distribution in the (a) same flavor and (b) opposite flavor channels. Events with M_{T2}^{ll} below (above) 110 GeV form the low (high) signal purity categories. The uncertainties in the above plots are statistical only. The M_{T2}^{ll} templates for signals with a pseudoscalar (magenta) and scalar (blue) mediator with $m_\phi = 100$ GeV and $m_\chi = 1$ GeV are overlayed and scaled by a factor of 200.

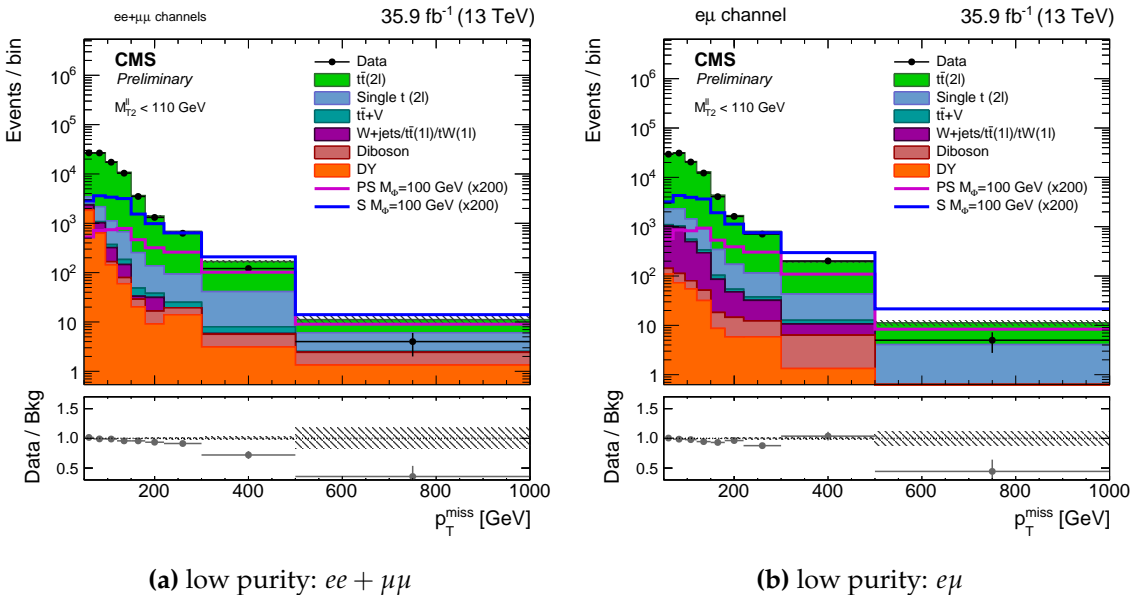


Figure 6.8.: The p_T^{miss} distributions in the low purity signal region for (a) same flavor and (b) opposite flavor events. The uncertainties in the above plots are statistical only. The p_T^{miss} templates in the low purity signal region for signals with a pseudoscalar (magenta) and scalar (blue) mediator with $m_\phi = 100$ GeV and $m_\chi = 1$ GeV are overlayed and scaled by a factor of 200.

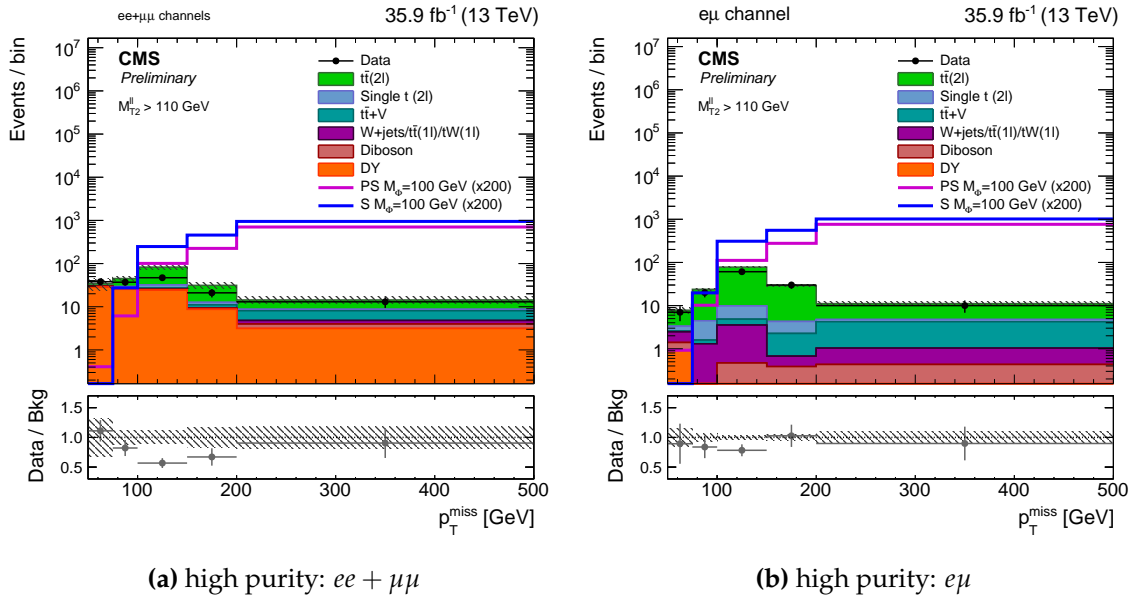


Figure 6.9.: The p_T^{miss} distributions in the high purity signal region for (a) same flavor and (b) opposite flavor events. The uncertainties in the above plots are statistical only. The p_T^{miss} templates in the high purity signal region for signals with a pseudoscalar (magenta) and scalar (blue) mediator with $m_\phi = 100 \text{ GeV}$ and $m_\chi = 1 \text{ GeV}$ are overlaid and scaled by a factor of 200.

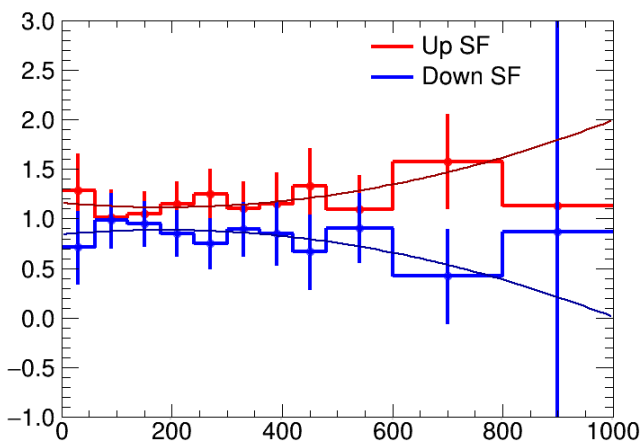


Figure 6.10.: The fake p_T^{miss} uncertainty at one standard deviation from the nominal recoil distribution as derived in simulation using Z bosons decaying to dielectrons and dimuons with $M_{T2}^{\ell\ell} > 110 \text{ GeV}$. In order to smoothen out the binned uncertainty, it is fit with a second-order polynomial.

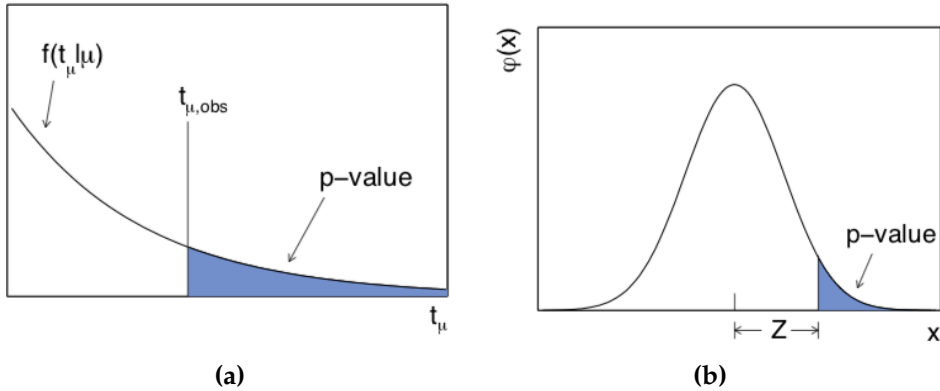


Figure 6.11.: A visualization of the relation (a) between the observed value of the test statistic $q(\mu)_{\text{obs}}$, the probability density function $f(q(\mu) \mid H)$ and the p -value, and (b) between the p -value and the significance Z.

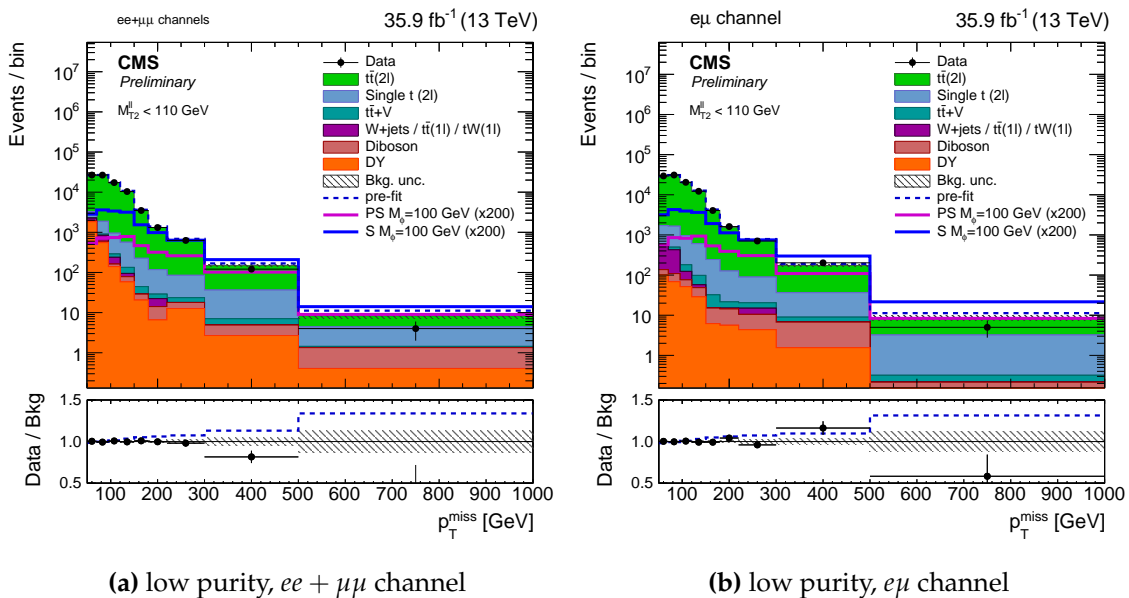


Figure 6.12: The background-only post-fit p_T^{miss} distributions in the low signal purity SRs. The expected (pre-fit) p_T^{miss} distributions for two example signals (scalar and pseudoscalar mediator, $m_{\phi/a} = 100$ GeV) with $m_\chi = 1$ GeV are scaled up by a factor of 200. The dashed blue line represents the total expected (pre-fit) MC background p_T^{miss} shape, and the subsequent ratio between the pre-fit and post-fit shape in the lower ratio panel. The last bin of the distributions includes overflow. Statistical and systematic uncertainties are shown.

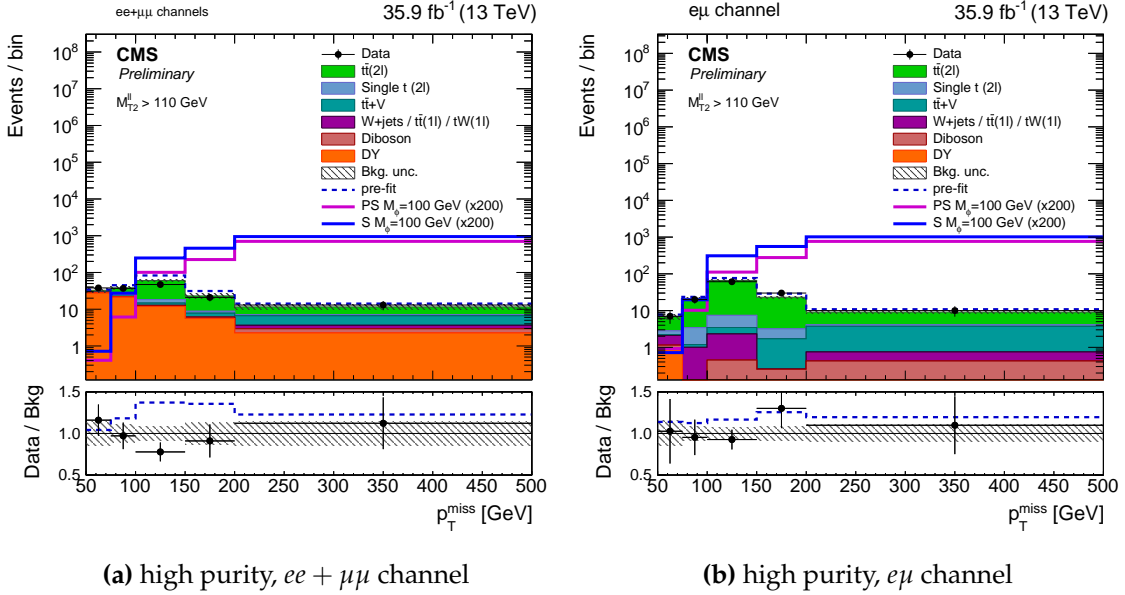


Figure 6.13.: The background-only post-fit p_T^{miss} distributions in the high signal purity SRs. The pre-fit p_T^{miss} distributions for two example signals (scalar and pseudoscalar mediator, $m_{\phi/a} = 100$ GeV) with $m_\chi = 1$ GeV are scaled up by a factor of 200. The dashed blue line represents the total expected (pre-fit) MC background p_T^{miss} shape, and the subsequent ratio between the pre-fit and post-fit shape in the lower ratio panel. The last bin of the distributions includes overflow. Statistical and systematic uncertainties are shown.

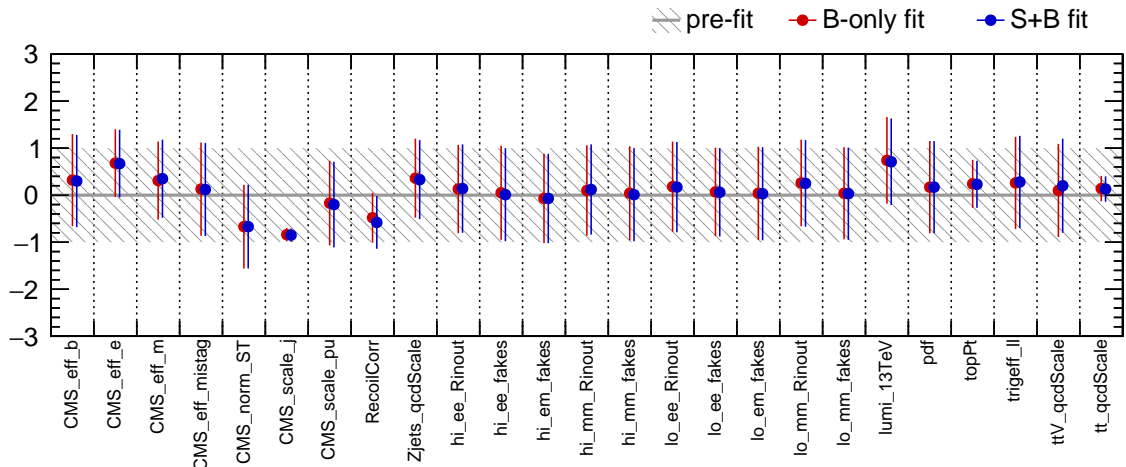


Figure 6.14.: Background-only (red) and signal-plus-background (blue) post-fit nuisance pulls.

Chapter 7.

Results

This chapter covers the results and interpretation of the fitting procedure described in the previous chapter, including the upper limits on signal yields for the $t\bar{t} + \chi\bar{\chi}$ process in the dilepton channel presented in Section 7.2. Section 7.3 presents the results in the same planes as results from direct and indirect dark matter detection experiments.

7.1. Simplified model interpretation

Dark matter production at colliders can be characterized, in large part, by the interaction between the SM and DM particles. The main characteristics of the simplified models under consideration are briefly highlighted in Sec. 4.1, and will be expanded upon in the following section.

Prior to Run II of the LHC, DM searches such as the one detailed in [63], had been traditionally interpreted using Effective Field Theory (EFT) models [64], wherein the interaction between the SM particles and the Dirac fermion WIMPs is mediated through higher dimensional operators. The models are solely characterized by the DM

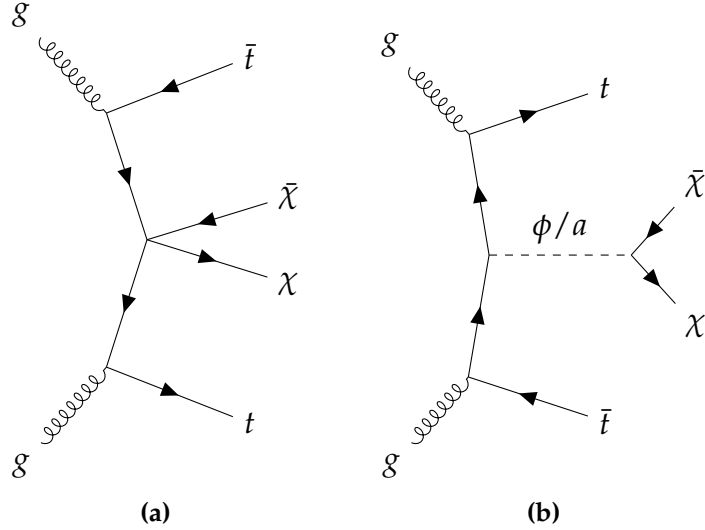


Figure 7.1.: The representative diagram of a top quark pair produced in association with a pair of DM particles ($\chi\bar{\chi}$) using (a) the EFT formalism and (b) the simplified model formalism.

mass, m_χ , and M_* which represents the strength of the interaction and is a function of the masses and coupling strengths of the mediating particles between the DM and SM fields. The benefits of the EFT formulation is the lack of model dependence, and the relative ease encountered in translating experimental collider constraints to the direct detection DM-nucleon cross section- m_χ plane. The shortcoming of such field theories, however, are that they are non-renormalizable, thus they become invalid at arbitrarily high energy scales, and this is represented by the masses of the mediating particles that have been integrated out. In general, for an EFT to make sense, it is required that M_* must be much larger than the energy transfer through quarks at the LHC, i.e. $M_*^2 \gg Q_{\text{tr}}^2$. Thus, since this class of models does not truly account for the mediator, effects from resonant enhancement are not included and EFTs have no sensitivity to off-shell mediator production.

In order to circumvent the deficiencies of the EFT formalism, a class of simplified models have been employed for the interpretation of DM searches during Run II of the LHC. In part, the increase in the center-of-mass collision energy from $\sqrt{s} = 8$ TeV

to $\sqrt{s} = 13$ TeV limits the region of validity for the EFT models. Hence, the contact interaction of the EFT models, as depicted in Figure 7.1a is subsequently resolved into a mediator interaction which couples to the SM and DM particles, as shown in Figure 7.1b.

The interaction Lagrangians of the scalar (ϕ) and pseudoscalar (a) mediators are as follows [65],

$$\mathcal{L}_\phi = g_\chi \phi \chi \bar{\chi} + \frac{\phi}{\sqrt{2}} \sum_i (g_u y_i^u \bar{u}_i u_i + g_d y_i^d \bar{d}_i d_i + g_\ell y_i^\ell \bar{\ell}_i \ell_i), \quad (7.1)$$

$$\mathcal{L}_a = i g_\chi a \chi \gamma_5 \bar{\chi} + \frac{i a}{\sqrt{2}} \sum_i (g_u y_i^u \bar{u}_i \gamma_5 u_i + g_d y_i^d \bar{d}_i \gamma_5 d_i + g_\ell y_i^\ell \bar{\ell}_i \gamma_5 \ell_i) \quad (7.2)$$

where the Yukawa couplings are $y_i^f = \sqrt{2} m_i^f / v$, where m_i^f is the fermion mass, and $v = 246$ GeV is the Higgs boson field vacuum expectation value. g_χ, g_u, g_d and g_ℓ represent the coupling strength between the mediator and the dark sector, up-type quarks, down-type quarks, and leptons respectively. In the report issued by the Dark Matter Forum (DMF) [65], a collaboration between members of CMS, ATLAS and the theory community, a benchmark set of parameters for the relevant simplified models of DM were chosen after scans of the parameter space were performed. In the following analysis, the DMF recommendation of $g_\chi = g_u = g_d = g_\ell = 1$ is followed. This reduces the free parameters to $\{m_\chi, m_\phi\}$ which contribute to the minimal mediator width at LO via,

$$\Gamma_\phi = \frac{m_\chi}{8\pi} \left(1 - \frac{4m_\chi^2}{m_\phi^2}\right)^{x/2} + \sum_{f=fermions} \frac{y_f^2 m_\phi}{16\pi} \left(1 - \frac{4m_f^2}{m_\phi^2}\right)^{x/2}, \quad (7.3)$$

m_ϕ [GeV]	m_χ [GeV]	Scalar (pb)	Pseudoscalar (pb)
10	1	26.09	0.6218
20	1	13.96	0.5653
50	1	3.923	0.4314
100	1	0.8891	0.2716
200	1	0.1229	0.1189
300	1	0.04079	0.05946
500	1	0.007796	0.008171

Table 7.1.: Summary of the signal samples and the correpsonding NLO cross sections used in this analysis for scalar and pseudoscalar mediator masses with $m_\chi = 1$ GeV.

with $x = 3$ for scalar mediators, and $x = 1$ for pseudoscalar mediators. Owing to the choice of SM Higgs-like Yukawa couplings for the SM fermions, the top quark contribution to the mediator width is enhanced at mediator masses above twice the top quark mass, but conversely for lighter mediator masses, the DM contribution dominates since couplings to the lighter quarks are Yukawa-suppressed. Thus the sensitivity of this search is concentrated in the low mediator mass regime, below twice the top quark mass. The signal samples used in the analysis were generated at LO accuracy in QCD with up to one additional parton in the final state, however as described in Ref. [66], the cross section is computed at NLO with no additional partons in the Born process, and the samples are normalized to the NLO values listed in Table 7.1

7.2. Upper limits on $t\bar{t} + \chi\bar{\chi}$ production in the dilepton channel

From the background-only post-fit yields presented in Table 6.1 and 6.2, it is apparent that there is no significant excess of events expected over the SM backgrounds, hence

Model (m_ϕ, m_χ) [GeV]	Obs.	Exp.	$[-1\sigma, +1\sigma]$	$[-2\sigma, +2\sigma]$
S 10, 1	0.72	0.59	[0.41, 0.89]	[0.30, 1.32]
S 20, 1	0.64	0.51	[0.35, 0.76]	[0.25, 1.11]
S 50, 1	0.74	0.62	[0.43, 0.94]	[0.31, 1.36]
S 100, 1	1.29	1.01	[0.69, 1.51]	[0.51, 2.19]
S 200, 1	2.97	2.40	[1.64, 3.58]	[1.19, 5.22]
S 300, 1	5.64	4.61	[3.16, 6.91]	[2.30, 10.11]
S 500, 1	22.93	18.74	[12.78, 28.52]	[9.26, 42.20]
PS 10, 1	1.16	0.92	[0.63, 1.38]	[0.46, 2.01]
PS 20, 1	1.16	0.92	[0.63, 1.38]	[0.46, 2.01]
PS 50, 1	1.26	1.00	[0.69, 1.50]	[0.50, 2.19]
PS 100, 1	1.49	1.18	[0.81, 1.77]	[0.59, 2.59]
PS 200, 1	2.45	1.95	[1.33, 2.93]	[0.96, 4.30]
PS 300, 1	3.99	3.23	[2.19, 4.89]	[1.60, 7.22]
PS 500, 1	22.29	18.06	[12.15, 27.49]	[8.78, 41.31]

Table 7.2.: Observed and expected upper limits at 95% CL_s on μ as a function of scalar (S) and pseudoscalar (PS) mediator masses for $m_\chi = 1$ GeV with $\pm 1\sigma$ and $\pm 2\sigma$ uncertainties on the expected limits.

95% CL_s upper limits on the signal strength parameter μ defined in Section 6.5.3 are set. The expected and observed upper limits on μ for signal models with varying scalar and pseudoscalar mediator masses and $m_\chi = 1$ GeV are listed in Table 7.2 along with the $\pm 1\sigma$ and $\pm 2\sigma$ uncertainties on the expected limit. The results shown in the tables are visualized in Figure 7.2a and Figure 7.2b as a function of m_ϕ , where the couplings are assumed to be $g_q = g_\chi = 1$ and the DM mass is $m_\chi = 1$ GeV. The range of m_ϕ are deemed as excluded by the search, when the upper limit on μ is less than 1. As can be seen in Figure 7.2a and Figure 7.2b, the observed (expected) 95% CL_s exclusions for a scalar mediator are $m_\phi < 74(99)$ GeV, while for a pseudoscalar mediator, the expected exclusion is $m_a < 50$ GeV, and no exclusion is observed.

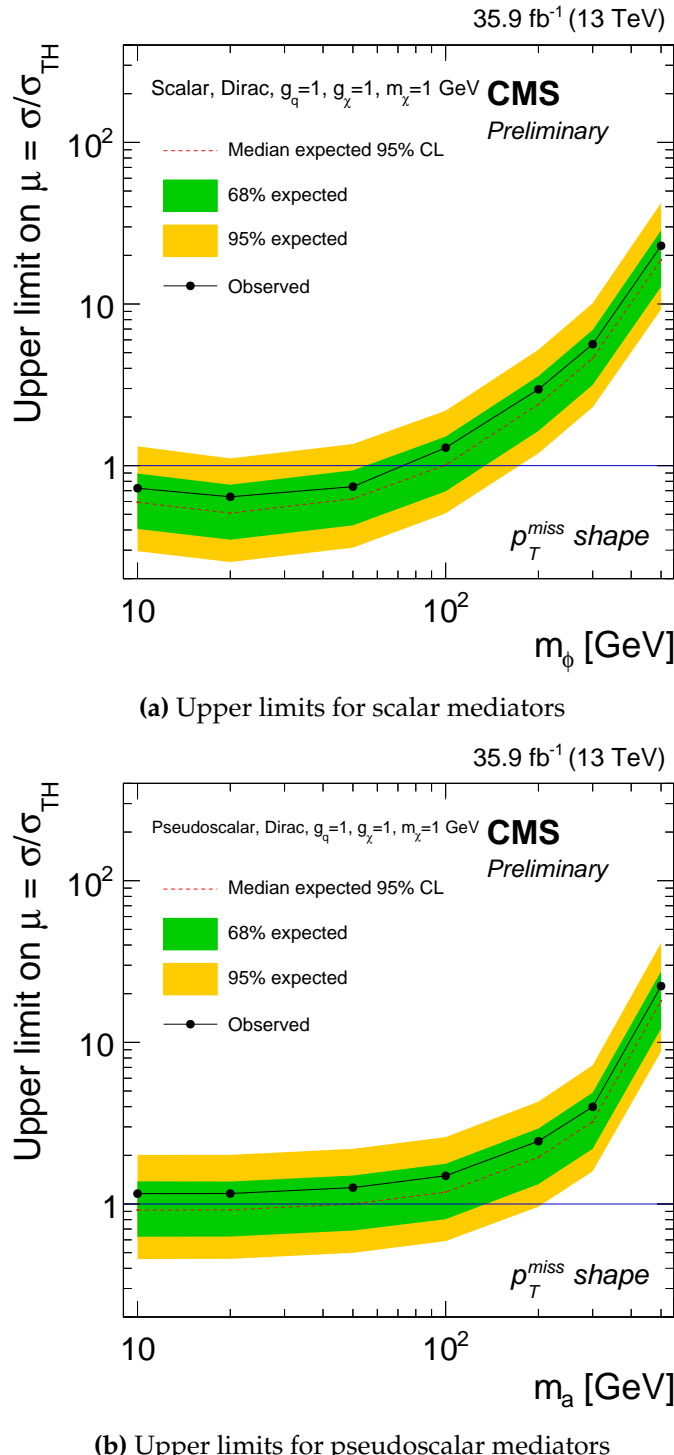


Figure 7.2.: The expected (red dashed) and observed (solid black) 95% CL_s upper limits on the $t\bar{t} + \chi\bar{\chi}$ signal strength in the dilepton channel for various (a) scalar and (b) pseudoscalar mediator masses where $m_\chi = 1$ GeV and $g_q = g_\chi = 1$ is assumed. The results are obtained using 35.9 fb^{-1} collected by the CMS detector in 2016.

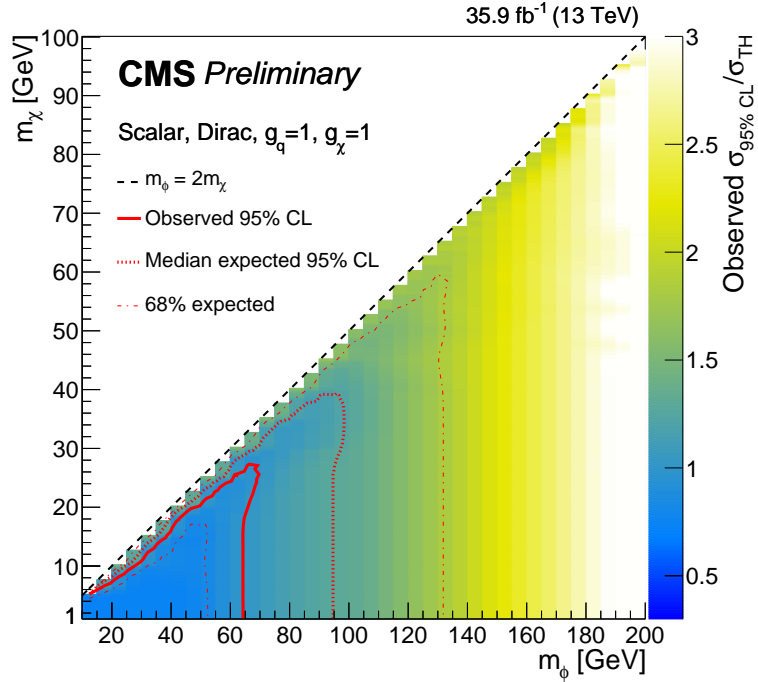


Figure 7.3.: The exclusion limits at 95% CL_s on the signal strength parameter μ for the $t\bar{t} + \chi\bar{\chi}$ process in the dilepton channel, computed as a function of the mediator mass and DM mass, assuming a scalar mediator. The mediator couplings are assumed to be $g_q = g_\chi = 1$.

The upper limits for on the scalar mediated $t\bar{t} + \chi\bar{\chi}$ signal are also shown as a function of m_ϕ and m_χ in Figure 7.3. The solid (finely dashed) contour encloses the region where the observed (expected) upper limit on μ is less than 1. It should be noted that the narrow width of the mediator causes the cross section to drop off very rapidly across the on-/off-shell ($m_\phi = 2m_\chi$) line, therefore the exclusion contour runs close to the diagonal but does not cross it.

7.3. Comparison with direct detection

To facilitate the comparison with constraints from direct detection experiments, the exclusion contours obtained from the scalar $t\bar{t} + \chi\bar{\chi}$ model as shown in Figure 7.3 are calculated at 90% CL_s. Subsequently, the upper limits on μ are translated to upper limits on the spin-independent (SI) DM-nucleon scattering cross section via the approach taken from Ref. [67] as briefly described in the proceeding section.

7.3.1. Spin-indepedent comparison

The general form of the spin-independent DM-nucleon scattering cross section is,

$$\sigma_{\text{SI}} = \frac{f^2(g_q) g_\chi^2 \mu_{n\chi}^2}{\pi m_\phi^4} \quad (7.4)$$

where $\mu_{n\chi} = m_n m_\chi / (m_n + m_\chi)$ is the DM-nucleon reduced mass with $m_n \simeq 0.939$ GeV being the approximate nucleon mass. The mediator-nucleon coupling, denoted by $f(g_q)$, has a non-trivial dependence on the mediator-quark couplings and the Higgs boson vacuum expectation value, so the full definition is ommitted. However, using the most state-of-the-art values for these dependencies from Refs. [68] and [69], the numerical value of $f(g_q)$ is,

$$f(g_q) = 1.16 \times 10^{-3} g_q. \quad (7.5)$$

Thus, Eq. 7.4 takes the form,

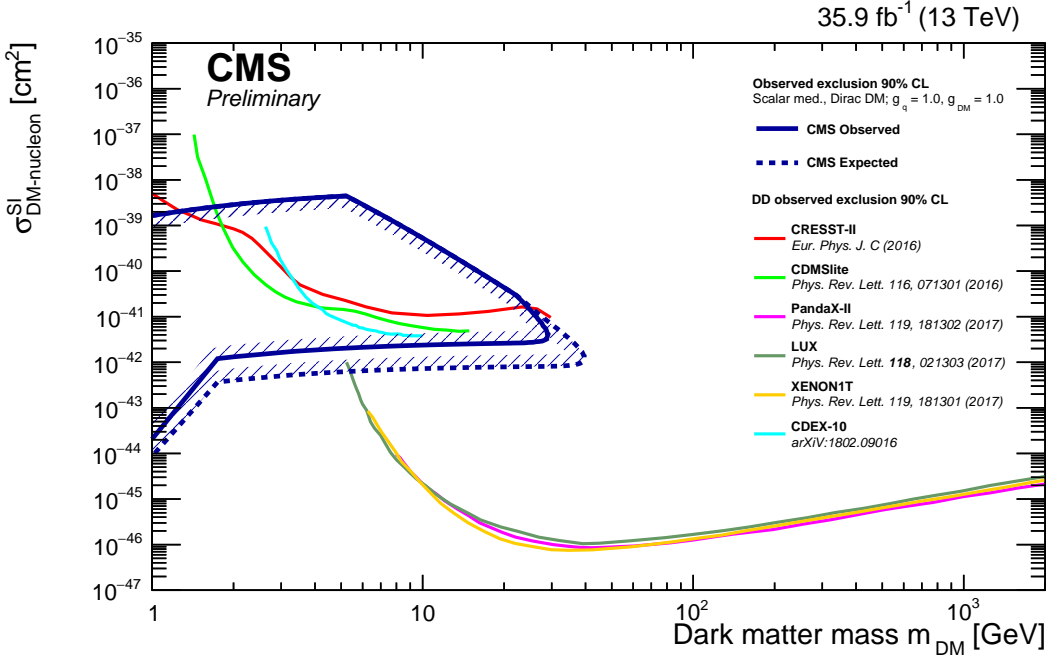


Figure 7.4.: A comparison of the $t\bar{t} + \chi\bar{\chi}$ scalar-mediated results in the dilepton channel (CMS expected and observed lines) to the exclusion contours of the LUX, PandaX-II, XENON1T, CDEX-10, CDMSLite, and CRESST-II limits in the m_χ - σ_{SI} plane. The DM particle is assumed to be a Dirac fermion and $g_q = g_\chi = 1$.

$$\sigma_{\text{SI}} \simeq 6.9 \times 10^{-43} \left(\frac{g_q g_\chi}{1} \right)^2 \left(\frac{125 \text{ GeV}}{m_\phi} \right)^4 \left(\frac{\mu_{n\chi}}{1 \text{ GeV}} \right)^2. \quad (7.6)$$

As a result, the upper limit on μ for the scalar-mediated $t\bar{t} + \chi\bar{\chi}$ process in the dilepton channel is presented as a bound in the m_χ - σ_{SI} plane in Figure 7.4. The assumptions made in the translation include that the DM particle is a Dirac fermion, the coupling values are $g_q = g_\chi = 1$, and the CMS expected and observed exclusions are calculated at 90% CL $_s$, as is standard in the direct detection community. The collider limits are the most constraining at low DM mass, which is well-supported by the strong constraints at low m_ϕ as seen in the limit curve in Figure 7.2a where $m_\chi = 1$ GeV.

Appendix A.

Pointless extras

“Le savant n’étudie pas la nature parce que cela est utile;

il l’étudie parce qu’il y prend plaisir,

et il y prend plaisir parce qu’elle est belle.”

— Henri Poincaré, 1854–1912

Appendices (or should that be “appendices”?) make you look really clever, ‘cos it’s like you had more clever stuff to say than could be fitted into the main bit of your thesis. Yeah. So everyone should have at least three of them…

A.1. Like, duh

Padding? What do you mean?

A.2. $y = \alpha x^2$

See, maths in titles automatically goes bold where it should (and check the table of contents: it *isn't* bold there!) Check the source: nothing needs to be specified to make this work. Thanks to Donald Arsenau for the teeny hack that makes this work.

Colophon

This thesis was made in L^AT_EX 2_& using the “hepthesis” class [70].

Bibliography

- [1] G. Bertone, D. Hooper, and J. Silk, Phys. Rept. **405**, 279 (2005), hep-ph/0404175.
- [2] J. L. Feng, Ann. Rev. Astron. Astrophys. **48**, 495 (2010), 1003.0904.
- [3] T. A. Porter, R. P. Johnson, and P. W. Graham, Ann. Rev. Astron. Astrophys. **49**, 155 (2011), 1104.2836.
- [4] F. Zwicky, General Relativity and Gravitation **41**, 207 (2009).
- [5] Planck, P. A. R. Ade *et al.*, Astron. Astrophys. **594**, A13 (2016), 1502.01589.
- [6] G. Bertone and D. Hooper, Submitted to: Rev. Mod. Phys. (2016), 1605.04909.
- [7] J. F. Meekins, G. Fritz, T. A. Chubb, H. Friedman, and R. C. Henry, Nature **231**, 107 EP (1971).
- [8] V. C. Rubin and W. K. Ford, Jr., Astrophys. J. **159**, 379 (1970).
- [9] S. W. Allen, A. C. Fabian, R. W. Schmidt, and H. Ebeling, Mon. Not. Roy. Astron. Soc. **342**, 287 (2003), astro-ph/0208394.
- [10] A. Refregier, Ann. Rev. Astron. Astrophys. **41**, 645 (2003), astro-ph/0307212.
- [11] J. A. Tyson, G. P. Kochanski, and I. P. Dell'Antonio, Astrophys. J. **498**, L107 (1998), astro-ph/9801193.
- [12] M. Markevitch, (2005), astro-ph/0511345, [ESA Spec. Publ.604,723(2006)].

- [13] R. H. Dicke, P. J. E. Peebles, P. G. Roll, and D. T. Wilkinson, *Astrophysical Journal*, vol. 142, p.414-419 **142**, 414 (1965).
- [14] S. Seager, D. D. Sasselov, and D. Scott, *Astrophys. J. Suppl.* **128**, 407 (2000), astro-ph/9912182.
- [15] WMAP, D. N. Spergel *et al.*, *Astrophys. J. Suppl.* **170**, 377 (2007), astro-ph/0603449.
- [16] Particle Data Group, K. A. Olive *et al.*, *Chin. Phys.* **C38**, 090001 (2014).
- [17] O. S. Bruning *et al.*, (2004).
- [18] G. Brianti, *Phys. Rept.* **403-404**, 349 (2004).
- [19] CMS, S. Chatrchyan *et al.*, *JINST* **3**, S08004 (2008).
- [20] ATLAS, G. Aad *et al.*, *JINST* **3**, S08003 (2008).
- [21] LHCb, A. A. Alves, Jr. *et al.*, *JINST* **3**, S08005 (2008).
- [22] ALICE, K. Aamodt *et al.*, *JINST* **3**, S08002 (2008).
- [23] B. Martin and G. Shaw, *Particle Physics* Manchester Physics Series (Wiley, 2008).
- [24] CMS Collaboration, *The CMS magnet project: Technical Design Report* Technical Design Report CMS (CERN, Geneva, 1997).
- [25] L. Borrello, A. Messineo, E. Focardi, and A. Macchiolo, (2003).
- [26] CMS ECAL, D. J. A. Cockerill, The CMS Electromagnetic Calorimeter at the LHC, in *Proceedings, 34th International Conference on High Energy Physics (ICHEP 2008): Philadelphia, Pennsylvania, July 30-August 5, 2008*, 2008, 0810.0381.
- [27] CMS, S. Chatrchyan *et al.*, *JINST* **8**, P09009 (2013), 1306.2016, [JINST8,9009(2013)].
- [28] CMS, S. Chatrchyan *et al.*, *JINST* **5**, T03014 (2010), 0911.4881.

- [29] C. Leroy and P.-G. Rancoita, *Principles of radiation interaction in matter and detection* (World Scientific, Singapore, 2009).
- [30] V. Halyo, A. Hunt, P. Jindal, P. LeGresley, and P. Lujan, JINST **8**, P10005 (2013), 1305.4855.
- [31] CMS, J. Brooke, PoS **ICHEP2012**, 508 (2013), 1302.2469.
- [32] J.-M. Andre *et al.*, **664**, 082033 (2015).
- [33] R. Fruhwirth, Nucl. Instrum. Meth. **A262**, 444 (1987).
- [34] CMS Collaboration, S. Cittolin, A. Rácz, and P. Sphicas, *CMS The TriDAS Project: Technical Design Report, Volume 2: Data Acquisition and High-Level Trigger*. CMS trigger and data-acquisition project Technical Design Report CMS (CERN, Geneva, 2002).
- [35] P. Avery, First Monday **12** (2007).
- [36] C. Eck *et al.*, *LHC computing Grid: Technical Design Report. Version 1.06* (20 Jun 2005) Technical Design Report LCG (CERN, Geneva, 2005).
- [37] G. Petrucciani, A. Rizzi, and C. Vuosalo, Journal of Physics: Conference Series **664**, 072052 (2015).
- [38] J. Alwall *et al.*, JHEP **07**, 079 (2014), 1405.0301.
- [39] M. L. Mangano, M. Moretti, F. Piccinini, and M. Treccani, JHEP **01**, 013 (2007), hep-ph/0611129.
- [40] P. Harris, V. V. Khoze, M. Spannowsky, and C. Williams, Phys. Rev. D **91**, 055009 (2015).
- [41] C. G. Lester and D. J. Summers, Phys. Lett. **B463**, 99 (1999), hep-ph/9906349.

-
- [42] S. Frixione, P. Nason, and C. Oleari, JHEP **11**, 070 (2007), 0709.2092.
 - [43] S. Alioli *et al.*, JHEP **06**, 043 (2010), 1002.2581.
 - [44] T. Sjöstrand *et al.*, Comput. Phys. Commun. **191**, 159 (2015), 1410.3012.
 - [45] S. Agostinelli *et al.*, Nuclear Instruments and Methods in Physics Research Sec. A: Accelerators, Spectrometers, Detectors and Associated Equipment **506**, 250 (2003).
 - [46] M. Beneke, P. Falgari, S. Klein, and C. Schwinn, Nucl. Phys. B **855**, 695 (2012), 1109.1536.
 - [47] M. Cacciari, M. Czakon, M. Mangano, A. Mitov, and P. Nason, Phys. Lett. B **710**, 612 (2012), 1111.5869.
 - [48] P. Bärnreuther, M. Czakon, and A. Mitov, Phys. Rev. Lett. **109**, 132001 (2012), 1204.5201.
 - [49] M. Czakon and A. Mitov, JHEP **12**, 054 (2012), 1207.0236.
 - [50] M. Czakon and A. Mitov, JHEP **01**, 080 (2013), 1210.6832.
 - [51] CMS, V. Khachatryan *et al.*, Phys. Rev. D**95**, 092001 (2017), 1610.04191.
 - [52] The ATLAS Collaboration, The CMS Collaboration, The LHC Higgs Combination Group, CERN Report No. CMS-NOTE-2011-005. ATL-PHYS-PUB-2011-11, 2011 (unpublished).
 - [53] J. S. Conway, Incorporating Nuisance Parameters in Likelihoods for Multisource Spectra, in *Proceedings, PHYSTAT 2011 Workshop on Statistical Issues Related to Discovery Claims in Search Experiments and Unfolding, CERN, Geneva, Switzerland 17-20 January 2011*, pp. 115–120, 2011, 1103.0354.
 - [54] CMS Collaboration, CERN Report No. CMS-PAS-LUM-17-001, 2017 (unpub-

- lished).
- [55] CMS, S. Chatrchyan *et al.*, JHEP **10**, 132 (2011), 1107.4789.
 - [56] CMS, CERN Report No. CMS-PAS-BTV-15-001, 2016 (unpublished).
 - [57] J. C. Collins, D. E. Soper, and G. F. Sterman, Adv. Ser. Direct. High Energy Phys. **5**, 1 (1989), hep-ph/0409313.
 - [58] J. Butterworth *et al.*, Journal of Physics G: Nuclear and Particle Physics **43**, 023001 (2016).
 - [59] NNPDF, R. D. Ball *et al.*, JHEP **04**, 040 (2015), 1410.8849.
 - [60] S. Baker and R. D. Cousins, Nuclear Instruments and Methods in Physics Research **221**, 437 (1984).
 - [61] T. M. Karbach and M. Schlupp, (2012), 1210.7141.
 - [62] E. Gross, CERN Yellow Reports: School Proceedings **4**, 165 (2017).
 - [63] CMS, V. Khachatryan *et al.*, JHEP **12**, 088 (2016), 1603.08914.
 - [64] J. Goodman *et al.*, Phys. Rev. **D82**, 116010 (2010), 1008.1783.
 - [65] D. Abercrombie *et al.*, (2015), 1507.00966.
 - [66] M. Backovi *et al.*, Eur. Phys. J. **C75**, 482 (2015), 1508.05327.
 - [67] G. Busoni *et al.*, (2016), 1603.04156.
 - [68] M. Hoferichter, J. Ruiz de Elvira, B. Kubis, and U.-G. Meißner, Phys. Rev. Lett. **115**, 092301 (2015), 1506.04142.
 - [69] P. Junnarkar and A. Walker-Loud, Phys. Rev. **D87**, 114510 (2013), 1301.1114.
 - [70] A. Buckley, The heptesis L^AT_EX class.

List of figures

1.1.	The velocities of emission regions from M31 as a function of distance to the center of the galaxy measured in minutes of arc along the NE major axis as reported by Rubin and Ford in Ref. [8].	3
1.2.	A composite image from the Hubble, Chandra, and Magellan telescopes of the 1E 0657-558 cluster of galaxies (Bullet cluster) depicting the X-rays emitted by the baryonic matter as a diffuse red gas, while the approximate location of the DM surrounding the visible matter is represented in a blue hue.	4
1.3.	The CMB radiation temperature anisotropy power spectrum as a function of the multipole order, ℓ , as measured by various experiments [16]. The angular scales that correspond to the multipole orders are listed across the top of the graph. The data points correspond to the experimental measurements and the error bars account for measurement uncertainties. The black curve represents the best global fit of the standard model of cosmology to the Planck data.	7

2.1. The approximate location of the LHC ring traced over the Swiss-French border near Geneva, Switzerland. Also indicated are the relative locations of the two high luminosity experiments (CMS and ATLAS), the low luminosity B-physics dedicated experiment (LHCb), and the dedicated ion experiment (ALICE).	10
2.2. A schematic of the CERN accelerator complex, where protons (blue arrows) and ions (lime green arrows) begin their journey to the main LHC ring at the Linac 2 and Linac 3, respectively.	12
2.3. The integrated luminosity as a function of time that the LHC delivered at $\sqrt{s} = 7 \text{ TeV}$ and $\sqrt{s} = 8 \text{ TeV}$ during 2011 and 2012, and at $\sqrt{s} = 13 \text{ TeV}$ during 2015 and 2016.	13
2.4. A diagram of the cylindrical coordinate system for the CMS detector. .	14
2.5. The total integrated luminosity that the LHC machine delivered to CMS, and the total integrated luminosity that the detector collected during the 2016 data-taking period.	16
2.6. Cross-section view of CMS	17
2.7. Schematic cross-section through the CMS tracker, where a single detector modules is represented by a line, and double lines signify back-to-back modules.	19
2.8. The strip hit resolution for the TIB and TOB layers which are comprised of Si sensors with varying strip pitch. The tracks selected have $p_T > 3 \text{ GeV}$, at least 6 hits in the inner tracker, and χ^2 probability greater than 9.	22

2.9. A quarter-view of the CMS hadron calorimeter. The shading indicates the grouping of scintillating layers optically added together to form trigger tower signal readouts. [28]	25
2.10. A quadrant view of CMS where the IP is at the lower left corner. The dark grey areas denote the locations of the various muon stations and the steel disks. The 4 drift tube (DT, in light orange) stations are labeled MB (muon barrel) and the cathode strip chambers (CSC, in green) are labeled ME (muon endcap). The resistive plate chambers (RPC, in blue) located in the barrel and the endcaps of CMS, are labeled RB and RE, respectively.	30
2.11. A schematic of the two stage CMS trigger architecture and the corresponding rate reduction at each stage [30].	31
2.12. An overview of the CMS L1 trigger where the detector inputs are at the bottom and the subsequent steps in rate reduction proceed vertically upwards.	33
2.13. A flow chart of the multi-tier worldwide LHC computing grid, where the components circled in red are examples of the U.S. resources that are part of Open Science Grid (OSG) as defined in detail in Ref. [35]. The computing resources at Northwestern University fall under the Tier 3 computing category.	37
3.1. W^+ and W^- decay to leptons and corresponding lepton neutrinos for all lepton generations.	40
3.2. Discriminator values for the CSVv2 algorithm for an inclusive multi-jet topology, where the total number of entries in the simulation is normalized to the observed number of entries in the data.	52

4.1. The representative diagram of a top quark pair produced in association with a pair of DM particles ($\chi\bar{\chi}$) which decay via an explicit scalar or pseudoscalar mediator coupled to the tops.	56
4.2. Generator level p_T distributions for scalar (solid lines) and pseudoscalar (dashed lines) mediators, with $M_\chi = 1 \text{ GeV}$, where distributions with the same color have the same mediator mass.	57
4.3. (a) Generator level p_T distributions for off-shell production, with solid lines for scalar and dashed lines for pseudoscalar, and $M_\chi = 50 \text{ GeV}.$ (b) Near the on-shell/off-shell threshold (green solid line), the kinematics has contributions from on-shell and off-shell production.	57
4.4. The $M_{T2}^{\ell\ell}$ distribution in data and simulation for events passing selection requirements for the $e\mu$ channel. The distribution of two example signals (scalar and pseudoscalar mediator, $M_{\phi/a} = 100 \text{ GeV}$) with $M_\chi = 1 \text{ GeV}$ is scaled up by a factor of 200. The last bin includes overflow. Uncertainties are statistical only.	61
5.1. Summary of the cross section measurements of SM processes as of January 2018 with data collected by the CMS experiment at $\sqrt{s} = 7, 8,$ and $13 \text{ TeV}.$	64
5.2. Leading order $t\bar{t}$ production diagrams probed at the LHC via (a), (b) gluon fusion, and (c) quark-antiquark annihilation.	64
5.3. Examples of the (a) $t\bar{t} + V$ process, and (b) diboson production at LO.	67
5.4. Single top quark production via (a) s-channel, (b) t-channel, and (c) in association with a W boson.	67

5.5. The Drell-Yan lepton pair-production process mediated by a virtual photon (γ^*) or Z boson at (a) $\mathcal{O}(\alpha)$ and (b),(c),(d),(e) $\mathcal{O}(\alpha\alpha_s)$	68
5.6. Z peak in data and MC after subtraction of non-Drell-Yan contribution estimate from opposite-flavor data events in the ee channel for various p_T^{miss} bins.	74
5.7. Z peak in data and MC after subtraction of non-Drell-Yan contribution estimate from opposite-flavor data events in the $\mu\mu$ channel for various p_T^{miss} bins.	75
5.8. Data/MC scale factors binned in p_T^{miss} applied to MC events used for the estimate of the Drell-Yan normalization in the dilepton channel signal regions.	76
5.9. Examples of (a) W+jets, and (b) semileptonic $t\bar{t}$ that contribute to the fake lepton background.	77
5.10. Measured electron fake rates as a function of lepton (a) p_T and (b) $ \eta $. .	80
5.11. Measured muon fake rates as a function of lepton (a) p_T and (b) $ \eta $. .	80
5.12. The p_T^{miss} distributions in the fake rate method validation region. All expected backgrounds are estimated using simulation, except for the fake lepton contribution, denoted “FR Pred” which is estimated via the fake rate method.	82
6.1. (a) Pileup distributions in data and MC. Also shown are the pileup profiles in a few run ranges scaled to the relative contribution to the total integrated luminosity.(b) The pileup distributions from varying the total inelastic cross section by $\pm 4.6\%$	85

6.2. N_{PV} distributions in data and MC pre and post PU re-weighting in a region dominated by semileptonic $t\bar{t}$ events. The MC is normalized to the observed yield.	85
6.3. Effect of the top p_T reweighting on the expected $t\bar{t}$ background p_T^{miss} shape for (a) $M_{T2}^{\ell\ell} < 110 \text{ GeV}$ and (b) $M_{T2}^{\ell\ell} > 110 \text{ GeV}$ events.	87
6.4. The efficiency measured as a function of jet p_T and various η bins for (a) correctly tagging b jets, (b) misidentifying c jets, (c) and misidentifying light flavor or gluon jets.	88
6.5.	104
6.5. Kinematic distributions in the same flavor ($ee + \mu\mu$) channel. Signals with a pseudoscalar (magenta) and scalar (blue) mediator with $m_\phi = 100 \text{ GeV}$ and $m_\chi = 1 \text{ GeV}$ are overlayed and scaled by a factor of 200 to illustrate the potential shape differences between the signal and background in the various distributions. The uncertainties shown in these plots on the data and background are purely statistical.	105
6.6.	106
6.6. Kinematic distributions in the same flavor ($e\mu$) channel. Signals with a pseudoscalar (magenta) and scalar (blue) mediator with $m_\phi = 100 \text{ GeV}$ and $m_\chi = 1 \text{ GeV}$ are overlayed and scaled by a factor of 200 to illustrate the potential shape differences between the signal and background in the various distributions. The uncertainties shown in these plots on the data and background are purely statistical.	107

6.7. The $M_{T2}^{\ell\ell}$ distribution in the (a) same flavor and (b) opposite flavor channels. Events with $M_{T2}^{\ell\ell}$ below (above) 110 GeV form the low (high) signal purity categories. The uncertainties in the above plots are statistical only. The $M_{T2}^{\ell\ell}$ templates for signals with a pseudoscalar (magenta) and scalar (blue) mediator with $m_\phi = 100$ GeV and $m_\chi = 1$ GeV are overlayed and scaled by a factor of 200.	108
6.8. The p_T^{miss} distributions in the low purity signal region for (a) same flavor and (b) opposite flavor events. The uncertainties in the above plots are statistical only. The p_T^{miss} templates in the low purity signal region for signals with a pseudoscalar (magenta) and scalar (blue) mediator with $m_\phi = 100$ GeV and $m_\chi = 1$ GeV are overlayed and scaled by a factor of 200.	108
6.9. The p_T^{miss} distributions in the high purity signal region for (a) same flavor and (b) opposite flavor events. The uncertainties in the above plots are statistical only. The p_T^{miss} templates in the high purity signal region for signals with a pseudoscalar (magenta) and scalar (blue) mediator with $m_\phi = 100$ GeV and $m_\chi = 1$ GeV are overlayed and scaled by a factor of 200.	109
6.10. The fake p_T^{miss} uncertainty at one standard deviation from the nominal recoil distribution as derived in simulation using Z bosons decaying to dielectrons and dimuons with $M_{T2}^{\ell\ell} > 110$ GeV. In order to smoothen out the binned uncertainty, it is fit with a second-order polynomial. . .	109
6.11. A visualization of the relation (a) between the observed value of the test statistic $q(\mu)_{\text{obs}}$, the probability density function $f(q(\mu) H)$ and the p -value, and (b) between the p -value and the significance Z.	110

6.12. The background-only post-fit p_T^{miss} distributions in the low signal purity SRs. The expected (pre-fit) p_T^{miss} distributions for two example signals (scalar and pseudoscalar mediator, $m_{\phi/a} = 100 \text{ GeV}$) with $m_\chi = 1 \text{ GeV}$ are scaled up by a factor of 200. The dashed blue line represents the total expected (pre-fit) MC background p_T^{miss} shape, and the subsequent ratio between the pre-fit and post-fit shape in the lower ratio panel. The last bin of the distributions includes overflow. Statistical and systematic uncertainties are shown.	110
6.13. The background-only post-fit p_T^{miss} distributions in the high signal purity SRs. The pre-fit p_T^{miss} distributions for two example signals (scalar and pseudoscalar mediator, $m_{\phi/a} = 100 \text{ GeV}$) with $m_\chi = 1 \text{ GeV}$ are scaled up by a factor of 200. The dashed blue line represents the total expected (pre-fit) MC background p_T^{miss} shape, and the subsequent ratio between the pre-fit and post-fit shape in the lower ratio panel. The last bin of the distributions includes overflow. Statistical and systematic uncertainties are shown.	111
6.14. Background-only (red) and signal-plus-background (blue) post-fit nuisance pulls.	111
7.1. The representative diagram of a top quark pair produced in association with a pair of DM particles ($\chi\bar{\chi}$) using (a) the EFT formalism and (b) the simplified model formalism.	114

List of tables

3.1.	Variables and thresholds that define “FO”, “Loose”, and “Tight”. “-” indicates the variable is not considered for that working point.	43
3.2.	Effective areas for electron isolation PU subtraction.	46
3.3.	Variables and thresholds that define “FO”, “Veto”, and “Tight” electrons. An electron is in the barrel if it has supercluster $ \eta < 1.479$, otherwise it is in the endcap.	46
3.4.	Variables and thresholds that define the “Loose” PF jet ID.	49
5.1.	DY yields and $R_{\text{in/out}}$ values in the ee channel, for 0 b-tag selection . .	72
5.2.	DY yields and $R_{\text{in/out}}$ values in the $\mu\mu$ channel, for 0 b-tag selection . .	73
5.3.	DY yields and $R_{\text{in/out}}$ values in the ee channel, for ≥ 1 b-tag selection . .	73
5.4.	DY yields and $R_{\text{in/out}}$ values in the $\mu\mu$ channel, for ≥ 1 b-tag selection . .	73
5.5.	Signal region DY yields in MC and data (from $R_{\text{in/out}}$ prediction) in the ee channel	76
5.6.	Signal region DY yields in MC and data (from $R_{\text{in/out}}$ prediction) in the $\mu\mu$ channel	76

5.7. Electron fake rates	79
5.8. Muon fake rates	79
6.1. Background-only post-fit event yields passing selection in the $M_{T2}^{\ell\ell} > 110 \text{ GeV}$ (high signal purity) category. The expected (pre-fit) yield is also shown for a pseudoscalar $m_a = 100 \text{ GeV}$, $m_\chi = 1 \text{ GeV}$ signal. The uncertainties include contributions from both systematic and statistical sources.	100
6.2. Background-only post-fit event yields passing selection in the $M_{T2}^{\ell\ell} < 110 \text{ GeV}$ (low signal purity) category. The expected (pre-fit) yield is also shown for a pseudoscalar $m_a = 100 \text{ GeV}$, $m_\chi = 1 \text{ GeV}$ signal. The uncertainties include contributions from both systematic and statistical sources.	100
6.3. A summary of the naming convention for the nuisance parameters used in the fit, whether each is implemented as “lnN” (normalization uncertainty) or “shape” (shape uncertainty), and which processes each affects. Unless indicated under the description heading, a nuisance is treated as correlated across both same and opposite flavor, high and low $M_{T2}^{\ell\ell}$ signal regions, and across the signal and all background processes.	103
7.1. Summary of the signal samples and the corresponding NLO cross sections used in this analysis for scalar and pseudoscalar mediator masses with $m_\chi = 1 \text{ GeV}$	116
7.2. Observed and expected upper limits at 95% CL _s on μ as a function of scalar (S) and pseudoscalar (PS) mediator masses for $m_\chi = 1 \text{ GeV}$ with $\pm 1\sigma$ and $\pm 2\sigma$ uncertainties on the expected limits.	117